Optimization of WEC arrays

A new approach for the combined optimization of positions and damping coefficients

Jacopo Gallizioli

A thesis presented for the Master's degree of
Aeronautical Engineering

Dipartimento di Matematica
Politecnico di Milano
Italia
November 28, 2022

Acknowledgement

First and foremost I am extremely grateful to my supervisor, Prof. Gabriele Ciaramella, for his invaluable advice, that extends outside the purely academic domain, his continuous support, and his patience. I also could not have undertaken this journey without the help of current Ph.D. student Marco Gambarini, who assisted me during the whole process, providing critical contributions to my thesis development, and to whom I truly wish the very best. I am also thankful to Prof. Edie Miglio, who granted me the opportunity of working on this fantastic project. Lastly, I would be remiss in not mentioning my friends and part of my family. My heartfelt thanks go directly to Linh and Letizia, who supported me more than anyone else in these challenging times.

Abstract

The ways of harvesting power from the sea is a topic that has been studied since the end of the past century. Given the importance that is nowadays associated with the use of renewable energies, the number of studies on this subject is quickly increasing. In this thesis, we consider wave energy converters as cylindrical bodies whose dynamic behavior is modeled through a linear spring-damper system.

Positioning these bodies into different configurations, the total power extracted by the array they compose varies according to the positions they take. Interestingly, for some arrangements, it is possible to notice an increase in performances with respect to the scenario where the bodies are isolated. This phenomenon is called park effect. The extent to which the park effect contributes to the produced power is evaluated through the interaction factor, which is computed as the ratio between the power obtained by an array, and sum of the powers that each device composing the array would produce if it were isolated from all the other devices.

What we want to achieve with this thesis is the development of a design strategy for a park of wave energy converters, that acts on both its geometrical and physical characteristics. Concerning the geometry of the array, we aim at computing the positions of its bodies, for which the interaction factor is maximized. Similarly, the physics of the array is improved by computing the damping coefficients that optimize the total extracted power. The biggest novelty introduced in this thesis is the combined optimization of the positions and of damping coefficients.

The first step towards our goal is the study of the mathematical model developed by Child [6], which describes the interaction between waves and cylindrical bodies. A numerical implementation of this model is subsequently developed, using Python as the chosen programming language. Afterward, we validate our numerical implementation comparing the results that it produces, with the ones obtained in other previously published studies.

Subsequently, to optimize the array, we develop the necessary mathematical models. We start by detailing how to optimize the positions and the damping coefficients individually. And we conclude by developing a model for the combined optimization of the positions and of the damping coefficients. Concerning the positions optimizations, we use the projected gradient method, where the cost function, to be minimized, is the total power with opposite sign, and its gradient is computed through a Lagrangian approach. We choose to use the projected gradient method, because we want to study which are the optimal positions of the bodies, under the constraint of them being fixed inside a given domain. Also for the damping coefficients optimization algorithm, a gradient method is used, with the requirement of the damping coefficients being positive

at each iteration. Regarding the combined optimization, this is performed using a two steps gradient method, in which, at each iteration, we first modify the positions of the bodies, and subsequently their damping coefficients.

These optimization strategies are therefore implemented, once again in Python to determine optimal configurations. We test them on arrays with different initial conditions, subject to different kinds of constraints. The obtained results show that, after the optimization is performed, the performances are indeed improved. This improvement amounts to different values according to the starting configuration and the selected constraint. Further optimizations could be performed using similar methods applied to other quantities, such as the bodies stiffness coefficients or the body's geometrical dimensions.

Contents

List of Figures

List of Tables

List of Algorithms

Chapter 1

Introduction

This thesis is concerned with the optimization of arrays of wave energy converters.

The optimization aims at exploiting the so-called park effect, an important property that is present not only in arrays of wave energy converters but also of wind turbines and similar devices. Given an array of energy converters, the park effect is the phenomenon that leads to different levels of power production, based on how the bodies are positioned in the array with respect to each other. The amount to which the park effect contributes to greater power production is estimated through the interaction factor, which is a scalar quantity defined as the ratio between the power produced by the array and sum of the powers that each device composing the array would produce if it were isolated from all the other devices.

The park effect is a consequence of the hydrodynamic interaction between the various bodies composing an array that is subject to incident ambient waves. Therefore, to study how to compute the optimal positions of the bodies, that would correspond to a greater interaction factor, it is necessary to detail how this interaction happens.

The first step in modeling this interaction consists in stating which kind of flow model is selected. Most studies resort to a linear potential model, under the inviscid and incompressible hypothesis. This model is convenient because it allows for less computational effort, with respect to a nonlinear model, or to a model with a viscous, compressible flow. In our study, we also consider this kind of flow in the derivations of the interaction model. Only a few studies with nonlinear theories were attempted. Some of them performed simulations using the full set of Navier-Stokes equations, [8].

There are also multiple ways of modeling the actual interaction between the incident ambient waves with the energy converter. Also concerning this choice, there are multiple options. The path that has been pursued for longer, because of the lower computational effort it requires, is one where the energy converter is modeled as a point absorber [5] [10]. The drawback of this methodology is that it neglects the interaction due to scattered waves. Later models were

derived, which consider the interaction between bodies through planar waves, neglecting the evanescent wave numbers [26]. Subsequently, methods, where the radiation and scattering properties of the bodies are used to iteratively add the reflected waves inside the array, were developed [24], [21], [20]. Lastly, we have the direct-matrix method, which allows computing the flow-field without the need of iterating the process [17]. This direct-matrix method is the one used in our modeling. Further progress has been made either by improving the direct-matrix method or developing more modern analytical methods, which, as a trade-off, require larger computational effort, and are outside the scope of this thesis.

Now, to compute the power produced by our array, it is necessary to compute the equation of motion of our bodies, which can be derived only by defining the dynamic properties of the bodies at study. There are multiple ways in which an energy converter can function when it comes to the methods for extracting energy from the waves, and, based on the way this happens, the dynamical properties of the body are different. However, being a wave energy converter a device that, placed in water, is moved by the ambient waves, and since the energy is always obtained by damping the motion of the energy converter taking energy from the wave, it is clear that the way the damping coefficient of the structures is modeled is of key importance. The damping coefficient has to consider both the physical properties of each body and how the mooring systems interact with the above-mentioned bodies. The most common approach is to use a linear damper [30], [18], [35], this is also how we model the damper in our thesis. Few examples, where an approach using a nonlinear model for the spring component is used, do exist. For instance, a coupled time-domain method has been implemented to solve the energy converter motion and mooring line tension simultaneously [13]. Another study modeled the mooring cables as catenary lines in a quasi-static analysis [31], or again, in another one, a finite element cable model is used to study arrays of different energy converters with a stochastic method, focusing on power variations [3].

Given that our purpose is not only to compute the power produced by an array but to maximize the extracted power, it is necessary to describe the optimization strategies used in other studies and the one we choose to implement.

In many studies, rather than performing an actual optimization of parameters, a comparison between different array configurations is performed [4], [9], [27], usually without specifying why a specific configuration is chosen.

The second step that many studies take, in the direction of an actual optimization, is sweeping over one parameter while keeping the others fixed [28], [23]. This allows one to find useful information and good values for certain parameters, but it is not guaranteed that these are optimal solutions. In many of these studies, not only the total power output is studied, but also the quality of the power supplied to the electric grid, which comes in the form of a low variance power output [29].

Now, we analyze the published articles that concern optimization problems. One example is a study with the aim to optimize the damping and stiffness constants of the device, making them time-varying parameters [32]. There are

also studies that optimize the power produced, without the limitation of a fixed geometry [22], [23], but all of them still use the point-absorber model, which, as we previously stated, neglects some key wave-bodies interactions.

One important branch of optimization methods is the one recurring to metaheuristic methods. These optimization methods are more modern and very useful when the optimization problem is very complex. The drawback of using these algorithms is that the optimal solution is not found analytically and, therefore, it is often suboptimal. An example of a metaheuristic algorithm is the genetic algorithm (GA) [7], which mimics the process of natural selection. Starting from a given configuration, mutations are added, and the best-performing new one is subsequently modified again, until convergence. Another algorithm that is part of this category is the particle swarm algorithm, which was found to outperform genetic algorithms [11].

The optimization strategy we adopt differs from the previously listed strategies because it is not based on the point-absorber model theory. As previously stated, we choose a direct-matrix method to compute the extracted power, therefore our optimization strategy will refer to this method of computing the power production. The process through which we build our optimization algorithm is described in chapter 4 of this thesis and is here briefly discussed. We choose, as the cost function to be minimized, the produced power with negative sign. We proceed by stating the Lagrangian formulation of the problem. This consists in augmenting the cost function with the state equation, which is given by the direct-matrix method, multiplied times a vector of Lagrangian multipliers. We proceed by computing the adjoint equations to compute the Lagrangian multipliers, and subsequently the gradient of the cost function. Here, the gradient is taken with respect to the parameter that we aim to optimize. In this thesis, we consider three optimization problems. One for the positions of the bodies, one for their damping coefficients, and one for the combined optimization of their positions and damping coefficients. Therefore, both the gradient of the cost function with respect to the positions of the bodies and the one with respect to the damping coefficients of the bodies, are computed. Focusing on the optimization of the positions, once we have computed the gradient of the cost function with respect to the positions, we use it to implement a projected gradient method, that projects the solution into a chosen admissible set. Also concerning the damping optimization, an iterative gradient method is applied. In this case, there is no need to project the solution, but we have to guarantee that the damping coefficient is positive at each iteration. Lastly, the combined optimization consists in adopting a 2-step method that, at each iteration, in the first step, using the previously described position gradient, optimizes the positions of the bodies, and in the second one, optimizes their damping coefficients. These optimization strategies are therefore numerically implemented and the obtained results are commented on in chapter 5.

Having described the content of this thesis, we now detail how it is organized in the various chapters. In chapter 2, taking as a reference Child's thesis [6], we go through the mathematical development of the model describing the interaction between floating cylinder and monochromatic waves. We start studying the

case of an isolated device, and we subsequently extend our analysis to the case of arrays composed of multiple devices. In this chapter, we also describe how to numerically implement the above-mentioned mathematical model. Next, in chapter 3, we perform the validation of our implementation. This is performed by comparing the results produced by our numerical implementation, with the ones obtained in other previously published studies. In addition, some tests are developed to verify that our implementation showcase some properties, of arrays of wave energy converter, which are widely agreed on by the scientific community. In chapter 4, we develop the optimization algorithms that allow us to compute optimal configurations. We start by developing the algorithms that optimize positions and damping coefficients independently. Subsequently, an algorithm performing compound optimization of positions and damping coefficients is developed. All the above-mentioned algorithms resort to gradient methods, whose exactness is verified by performing a convergence test with a finite differences approach. Subsequently, in chapter 5, we show and comment on the results obtained by running the optimization algorithms with different starting configurations, and forcing the bodies of the array into admissible sets of different sizes. Lastly, in chapter 6, we list the key findings of our studies presenting its weaknesses and limitations. One of the most important obtained result is the fact that the optimizations of the positions and of the damping coefficients seem to happen almost independently. In addition, concerning the positions of the bodies, we get that, under the constraints of our analysis, to obtain an optimal configuration it is necessary to increase the spacing between the devices as much as possible. At the same time, we obtain that it is necessary, for the damping coefficients of the bodies belonging to the columns interacting earlier with the ambient incident wave, to have higher values than the one of the devices in the column placed further down the direction of the wave. We also present some recommendations regarding possible future research on this topic.

Chapter 2

Mathematical and numerical modeling

The goal of this chapter is to provide a clear mathematical representation of the object at study, together with the necessary information for a correct numerical implementation.

In section 2.1, we start by describing all the hypotheses regarding the cylindrical bodies, which represent the energy converters, and the environment with which they interact. Next, in section 2.2, we analyze how the presence of a single body affects the flowfield around it when subject to an incident wavefield. In section 2.3, we develop the complete model describing the flowfield modification induced by an array of bodies.

Once this model is fully developed, we use it to compute many useful derived quantities in subsection 2.3.4, such as the forces acting on the cylinders and the power extractable from them. This is of particular interest since what we aim to maximize is the interaction factor. That is a coefficient computed as the ratio between the total power produced by an array of bodies, and the power produced by a single one multiplied by the number of bodies in the array. It is an important quantity because it represents to which degree the power production can be improved by exploiting the park effect.

Lastly, in section 2.4, we describe how to correctly perform the numerical implementation of the equations developed in the above-mentioned sections.

We specify that the content of this chapter follows the development of chapters 3 and 4 of Child's thesis. What we add to his work is a clear explanation of the underlying physics of the mathematical quantities developed in this chapter. Moreover, we create some graphs, as a support tool, to better visualize some of the discussed quantities.

2.1 Hypotheses

In this section, we discuss all the mathematical hypotheses used in our model, and highlight their practical implications. The degree to which these hypotheses worsen the truthfulness of our results is investigated, and the reason for their necessity is explained.

2.1.1 Flow Hypotheses

The ultimate objective of the model we are about to describe is to be able to give a reasonable estimation of the velocity field in the chosen domain. This is why it is of crucial importance to describe the hypotheses regarding the flowfield clearly. These are here conveniently listed:

- *Linear theory.* A linear model is useful for multiple reasons. First, it allows us to write our problem into the typical matrix-vector multiplication of linear algebra problems, which can be solved efficiently. Second, the use of a nonlinear model would introduce a substantial degree of complexity, that is outside the scope of this thesis. The drawback of using linear theory is the fact that nonlinear phenomena appear, especially in the neighborhood of the sharp edges of the cylinder, where turbulence is expected to be generated.

- *Irrotational flow.* Thanks to this assumption the velocity field is written as follows:

$$u = \nabla\phi, \tag{2.1}$$

  where ϕ is the scalar potential field associated to each point in our domain.

  This hypothesis, that, considering the Helmholtz decomposition of the velocity vector field, allows us to neglect the second component of the velocity, is appropriate when the flow is close to being inviscid, which is the case for our application, given the sufficiently high Reynolds number it is associated to.

- *Incompressible flow.* Considering the flow to be incompressible is suitable for water whose depth does not change drastically, and whose velocity gradients are not too large, as in our case. That is because under these assumptions we have that the Mach number is much smaller than one. In mathematical terms this hypothesis is written as follows:

$$\nabla \cdot u = 0. \tag{2.2}$$

- *Surface tension neglection.* This hypothesis concerns the interface between the fluid and the above domain, representing the atmospheric air. It allows us to simplify the model development without compromising accuracy.

This is because, for low wavenumbers, which are the ones from which most of the energy is extracted, the surface tension is really small being the curvature small.

- *Inviscid flow.* This hypothesis is strongly connected to the one defining the flow as irrotational. Moreover, this assumption neglects the contribution of skin friction forces, and prevents the description of flow separation phenomena. The latter might become relevant when dealing with bodies having sharp edges, originating nonlinear drag forces. Given that the bodies we are considering are cylinders, the only points where these phenomena might be relevant are at the bottom face circumference, especially during the ascending motion of the body. This hypothesis is nonetheless necessary, given that the numerical tools to simulate such nonlinear effects are too computationally demanding.

2.1.2 Geometry Hypotheses

To complete the description of the hypotheses used to describe our model we have to look into the ones used to describe the body of the energy converter and the environment in which it is located.

We consider all energy converters to be identical. This not only simplifies the mathematical development, but it is also a realistic assumption, since the purchase of many energy converters for the installation of an energy park is strongly governed by an economy of scale [14]. Hence, even if performances could be improved by the use of a differently sized converter, we ignore this aspect assuming that the potential benefit would still be marginal compared to the greater purchase expenses.

We assume the converters to be perfectly cylindrical, with a radius $r = a$. This hypothesis prevents us from considering the local effects that develop around the body, such as the one caused by the effect of surface roughness. However, it is still reasonable since the buoys used for these applications are generally radially symmetric.

The last hypothesis, which could be eventually relaxed by adding a layer of complexity, is that all the devices are located at the same depth, in a sea with a flat bottom.

2.2 Single Body

Let us consider the case of a single body. The development of the model proceeds as follows: first, we define the reference frame and all the relevant quantities; second, we consider the different contributions to the potential due to different effects; third, we define a set of basis functions whose span is able to represent all the needed potential functions. We use image 2.1 as the reference for many relevant parameters.

The now introduced parameters are the depth of the sea d, the position of the frame of reference, whose origin is on the seabed, and whose *z-axis* is coaxial

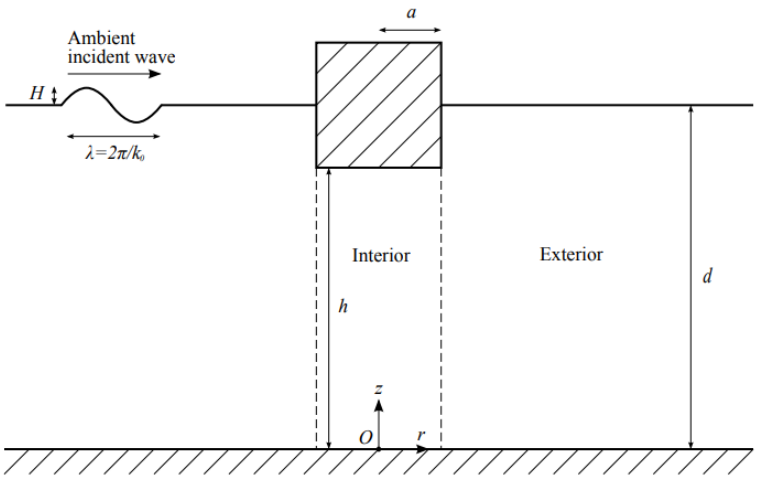

Figure 2.1: Side-view of a device with relevant parameters highlighted, figure from [6].

with the cylinder pointing upward, the distance from the seabed to the bottom face of the cylinder h, and the parameters related to the ambient incident wave, such as the wavenumber k_0, the amplitude H and the wavelength λ. From this picture, we also see how the domain is split into 2 regions: an interior and an exterior region. As we will detail later, we use different basis functions to represent the potential in the interior and exterior regions.

2.2.1 Governing equation

By applying both the incompressibility and the irrotational conditions, we see how the resulting governing equation becomes a Laplace equation in the variable ϕ:

$$\nabla^2 \phi = 0. \tag{2.3}$$

This equation has to be satisfied wherever ϕ is defined.

To have a complete description of the problem we impose the following boundary conditions:

- Imposing the vertical velocity component to be zero on the seabed:

$$\frac{\partial \phi}{\partial z} = 0 \quad on \quad z = 0. \tag{2.4}$$

- Imposing the radial velocity on the lateral surface of the cylinder to be zero:

$$\frac{\partial \phi}{\partial r} = 0 \quad on \quad r = a; \quad h \leq z \leq d. \tag{2.5}$$

- Imposing the vertical velocity at the bottom of the cylinder to be equal to the vertical velocity of the cylinder:

$$\frac{\partial \phi}{\partial z} = X' \quad on \quad z = h; \quad a \leq r \leq 0. \tag{2.6}$$

- Imposing the free surface condition relating the vertical velocity on the free surface to the frequency of the wave (using the fact that we neglect surface tension):

$$\frac{\partial \phi}{\partial z} = \frac{\omega^2}{g}\phi \quad on \quad z = d; \quad r \geq a. \tag{2.7}$$

  Since this condition imposes a matching of velocity at the interface, it is called *kinematic condition*.

On top of these boundary conditions, we have to add a condition that guarantees our flow to be radially bounded. This is because a radially unbounded solution would not have any physical meaning, since its energy would be increasing with r.

- This condition is called *radiation condition*, and it is mathematically represented as follows:

$$\lim_{r \to \infty} \sqrt{r} \left(\frac{\partial \phi}{\partial r} - ik_0 \phi \right) = 0. \tag{2.8}$$

Now that we analyzed all the conditions that the potential ϕ is subject to, we divide it into three different contributions: the scattered potential, the incident potential, and the radiated potential. This subdivision is meaningful only for the description of a single body, that is because, when multiple bodies are considered, the scattered potential of a body is to be seen as the potential incident to another.

The *scattered potential* from a body represents the wave generated from its interaction with an incident wave, under the constraint of the body being kept fixed in space. The *incident potential* to a body describes the ambient waves together with the incident waves that are generated by the other bodies in the array. Finally, the *radiated potential* portrays the contribution due to the vertical movement of the cylinder with no external wave. The above concept is formulated as follows:

$$\phi = \phi_S + \phi_I + \phi_R. \tag{2.9}$$

It will be useful to differentiate between the *ambient potential* ϕ_A, which represents the ocean wave from which we want to harvest energy, and the incident potential ϕ_I, which also includes the incident waves that are coming from the surrounding devices. Therefore, the incident potential ϕ_I describes a

broader range of waves then the ambient potential ϕ_A, being ϕ_A only one of the components that adds up to the complete incident potential ϕ_I.

Another useful definition is that of the *diffracted potential*, that is the sum of the incident and scattered potential: $\phi_D = \phi_I + \phi_S$.

Since each potential component is responsible for describing a different phenomenon, the governing equation that each of them has to satisfy is subject to different boundary conditions. This is the reason why each contribution needs a different set of basis functions to be described. In the next parts of this chapter, we describe in detail how to derive the wave basis of each of the different potential components.

2.2.2 Scattered wave basis

In this section, we construct a basis of functions for the scattered wave potential. Because of the cylindrical shape of the bodies, it is convenient to work in polar coordinates. This implies that also the Laplace equation has to be rewritten in polar coordinates,

$$\frac{\partial^2\phi}{\partial r^2} + \frac{1}{r}\frac{\partial\phi}{\partial r} + \frac{1}{r^2}\frac{\partial^2\phi}{\partial\theta^2} + \frac{\partial^2\phi}{\partial z^2} = 0. \tag{2.10}$$

Assuming the solution to be separable, we write the general form of the scattered potential as

$$\phi_S(r,\theta,z) = \sigma_r(r)\,\sigma_\theta(\theta)\,\sigma_z(z). \tag{2.11}$$

Now, we use the separation of variable approach, defining two separation constants, μ and ν. Substituting into (2.10) we have

$$\frac{\sigma_r''}{\sigma_r} + \frac{\sigma_r'}{r\sigma_r} + \frac{\sigma_\theta''}{r^2\sigma_\theta} = -\frac{\sigma_z''}{\sigma_z} = -\mu^2, \quad \mu\in\mathbb{C}, \tag{2.12}$$

$$-\mu^2 r^2 - \frac{\sigma_r'' r^2}{\sigma_r} - \frac{\sigma_r' r}{\sigma_r} = \frac{\sigma_\theta''}{\sigma_\theta} = -\nu^2, \quad \nu\in\mathbb{C}. \tag{2.13}$$

In the following subsections, we derive an expression for each of the three components of the scattered potential highlighted in (2.11). We do it distinguishing between the interior and exterior region of the domain, being the potential is subject to different boundary condition depending on the considered region.

Exterior region

Zeta separation To compute the z-dependence of the basis functions of the scatter potential, we refer to the right-side equation of (2.12). This, imposing the boundary condition on the seabed (2.4), allows us to obtain

$$\sigma_z(z) = c_1\cosh\mu z, \quad c_1\in\mathbb{C}. \tag{2.14}$$

The values of the μ-coefficients are computed by imposing the kinematic boundary condition at the free surface (2.7), which leads to

$$\frac{\omega^2}{g} = \mu \tanh \mu d. \tag{2.15}$$

This equation has a different solution based on μ being real or complex. For μ real, we get the solution to be $\mu = k_0$, with $k_0 \geq 0$, which represents the progressive wave number, or in other words the "spatial frequency" of a traveling wave. Meanwhile, for μ complex, we get the solution to be $\mu = ik_q$, with $k_q \geq 0$, and $q \in \mathbb{N}$, which represents the evanescent wave-number, or in other words the "spatial frequency" of a standing wave.

Now that the possible values of μ have been computed, we write the general solution of the scattered potential in the exterior region,

$$\sigma_z^q = \begin{cases} N_0^{-\frac{1}{2}} \cosh k_0 z & \text{if } q = 0, \\ N_q^{-\frac{1}{2}} \cosh k_q z & \text{if } q \geq 1, \end{cases} \tag{2.16}$$

where the subscript q is used to represent that the solution exists for different values of the wavenumber. From now on, a solution of the z-separation regarding a specific wavenumber q will be called the *q-th zeta-mode*. The N_0 and N_q coefficients are normalizing factors defined as

$$N_0 = \frac{1}{2}\left(1 + \frac{\sinh 2k_0 d}{2k_0 d}\right), \tag{2.17}$$

$$N_q = \frac{1}{2}\left(1 + \frac{\sinh 2k_q d}{2k_q d}\right). \tag{2.18}$$

This choice of normalizing factors gives us an orthonormal set of functions with respect to the L_2 product, this will be useful later on in the computation of further coefficients.

θ-separation We proceed in a similar way to the z-separation but considering (2.13).

By solving the right-side equation, we get the following expression for σ_θ:

$$\sigma_\theta(\theta) = c_1 e^{i\theta\nu} + c_2 e^{-i\theta\nu}. \tag{2.19}$$

Since this function represents the θ-dependence of the potential, it has to be periodic over a period of 2π, to guarantee continuity. This is obtained by imposing ν to be an integer.

Moreover, given the case of $\nu = 0$, we have the solution $c_1\theta + c_2$, which must have $c_1 = 0$ to satisfy continuity. This is because if c_1 were different from zero, we would have a function linearly growing with θ, and therefore not periodic over a period of 2π. Since the solution for the $\nu = 0$ case is a constant, it can therefore be included in (2.19).

The final solution for the θ-dependence of the scattered potential is finally expressed as follows:

$$\sigma_n^\theta = e^{in\theta}, \quad n \in \mathbb{Z}. \tag{2.20}$$

In analogy to the z-separation, the n subscript represents the *n-th θ mode*.

r-separation Since r is the third and last variable we do not need to define any additional separation constant, instead, we simply use the previously defined ones in (2.13) to obtain

$$-\mu^2 r^2 - \frac{\sigma_r'' r^2}{\sigma_r} - \frac{\sigma_r' r}{\sigma_r} = -\nu^2. \tag{2.21}$$

For the progressive case, we notice that the change of variable $\hat{r} = k_0 r$, $\hat{\sigma}_r(\hat{r}) = \sigma_r(r)$ leads to

$$\hat{\sigma}_r'' \hat{r}^2 + \hat{\sigma}_r' \hat{r} + \left(\hat{r}^2 - n^2\right) \hat{\sigma}_r = 0. \tag{2.22}$$

This is a Bessel differential equation, whose solutions can be written as Hankel functions of the first kind

$$H_n = J_n + iY_n. \tag{2.23}$$

Since we are interested in a set of basis functions, we define the solution as the sum of Bessel functions of the first kind and Hankel functions of the first kind,

$$\hat{\sigma}_r^n = c_1 J_n(k_0 r) + c_2 H_n(k_0 r). \tag{2.24}$$

We proceed in a similar manner for the progressive case, applying the change of variable $\hat{r} = k_q r$, $\hat{\sigma}_r(\hat{r}) = \sigma_r(r)$.

The resulting equation is the modified Bessel equation

$$\hat{\sigma}_r'' \hat{r}^2 + \hat{\sigma}_r' \hat{r} + \left(-\hat{r}^2 - n^2\right) \hat{\sigma}_r = 0. \tag{2.25}$$

The solution of this equation is a combination of Bessel functions of the first kind and one of the second kind,

$$\hat{\sigma}_r^q = c_1 I_n(k_q r) + c_2 K_n(k_q r). \tag{2.26}$$

We now enforce the radiation condition, guaranteeing also that the functions have the correct phase. They must move toward infinity and not come from infinity.

To guarantee that the scattered waves are traveling toward infinity we must enforce the boundary condition

$$\lim_{r\to\infty} u(r,t) = Ae^{i(kr-\omega t)}. \tag{2.27}$$

Since the asymptotic expansion of the H and J functions at infinity are

$$H_n(r) \sim \sqrt{\frac{2}{\pi z}} e^{i\left(r-\left(n+\frac{1}{2}\right)\frac{\pi}{2}\right)}, \tag{2.28}$$

$$J_n(r) \sim \sqrt{\frac{2}{\pi z}} \cos\left(r - \left(n+\frac{1}{2}\right)\frac{\pi}{2}\right), \tag{2.29}$$

we see that H is the only contribution to the solution satisfying (2.27), hence we have to discard the J_n functions from our solution. In an analogous manner, one can prove the necessity of discarding the I_n functions.

Moreover, we normalize our solution to obtain the following final result, which consists in the set of basis functions describing the radial dependence of the scattered potential in the exterior region:

$$\sigma_r^{q,n} = \begin{cases} \frac{H_n(k_0 r)}{H_n'(k_0 a)} & \text{if } q = 0,\ n \in \mathbb{Z} \\ , \frac{K_n(k_q r)}{K_n'(k_q a)} & \text{if } q \geq 1,\ n \in \mathbb{Z}. \end{cases} \tag{2.30}$$

General solution Combining the previously obtained result, we write the set of functions describing the scattered potential in the exterior region,

$$\phi_S|_n^q = \begin{cases} \frac{gH}{\omega} N_0^{-\frac{1}{2}} \cosh(k_0 z) \frac{H_n(k_0 r)}{H_n'(k_0 a)} e^{in\theta} & \text{if } q = 0,\ n \in \mathbb{Z} \\ \frac{gH}{\omega} N_q^{-\frac{1}{2}} \cosh(k_q z) \frac{K_n(k_q r)}{K_n'(k_q a)} e^{in\theta} & \text{if } q \geq 1,\ n \in \mathbb{Z}. \end{cases} \tag{2.31}$$

Interior region

We now proceed to compute the basis functions of the scattered potential in the interior region. Following the same approach as for the exterior region, we use the separation of variables approach to solve the Laplace equation in polar coordinates, (2.11) - (2.13). The difference from the exterior region case, is in the boundary conditions to apply.

z-separation Solving the right side equation of (2.12), we get the same general solution (2.14). Applying the boundary condition at the bottom of the buoy, we get the equation to compute the value of μ to be

$$\sinh(\mu h) = 0, \tag{2.32}$$

whose solution is the set of imaginary numbers

$$\mu = i\frac{s\pi}{h}, \quad s \in \mathbb{Z}. \tag{2.33}$$

Hence, substituting these values into the general solution, and fixing the constant coefficient to the desired value, we get the solution for the z-separation to be

$$\sigma_z^s(z) = \begin{cases} \frac{1}{2} & \text{if } s = 0, \\ \cos\left(\frac{s\pi z}{h}\right) & \text{if } s \neq 0. \end{cases} \tag{2.34}$$

θ-separation For the interior region, we have the same governing equations and boundary conditions in the θ variable as in the exterior region case. Therefore, we get

$$\sigma_n^\theta = e^{in\theta}, \quad n \in \mathbb{Z}. \tag{2.35}$$

r-separation Substituting the new values of μ ($s \neq 0$) into (2.21), being μ complex, we get a modified Bessel equation, whose solution is written as

$$\sigma_r(r) = c_1 I_n\left(\frac{shr}{\pi}\right) + c_2 K_n\left(\frac{shr}{\pi}\right). \tag{2.36}$$

For the case of $s = 0$, we apply the usual change of variable $\hat{r} = \frac{r}{a}$, $\hat{\sigma}_r(\hat{r}) = \sigma_r(r)$. The equation becomes, for $n \neq 0$, an Euler equation in $\hat{\sigma}_r$, $\hat{r}$,

$$\hat{\sigma_r}''\hat{r}^2 + \hat{\sigma_r}'\hat{r} \pm n^2\hat{\sigma}_r = 0, \tag{2.37}$$

whose solution is

$$\sigma_r(r) = c_1\left(\frac{r}{a}\right)^n + c_1\left(\frac{r}{a}\right)^{-n}. \tag{2.38}$$

For $s = 0$, $n = 0$, we get a simpler differential equation,

$$\hat{\sigma_r}''\hat{r}^2 + \hat{\sigma_r}'\hat{r} = 0, \tag{2.39}$$

whose solution is

$$\sigma_r(r) = c_1 \log\left(\frac{r}{a}\right) + c_2. \tag{2.40}$$

Since we are now in the interior region, we have to discard all the terms that diverge for $r \to 0$, because they are not physically meaningful. By doing so in the $s \neq 0$ case, we discard the K_n functions. For the $s = 0$ and $n = 0$ case, we discard the log term. Hence, the solution reduces to a constant and can be included in the general solution of the Euler equation.

The final expression for a set of basis functions for the scattered potential in the interior region is

$$\sigma_r^{s,n}(r) = \begin{cases} \frac{I_n\left(\frac{s\pi r}{h}\right)}{I_n\left(\frac{s\pi a}{h}\right)} & \text{if } s \neq 0, \quad n \in \mathbb{Z}, \\ \left(\frac{r}{a}\right)^{|n|} & \text{if } s = 0, \quad n \in \mathbb{Z}. \end{cases} \tag{2.41}$$

General solution Now that we have described the basis functions for the three variables in the inner region for the scattered potential, we combine them to obtain the general solution, that is

$$\left(\tilde{\phi}_S\right)_s^n = \begin{cases} \frac{gH}{\omega}\cos\frac{s\pi z}{h}\frac{I_n\left(\frac{s\pi r}{h}\right)}{I_n\left(\frac{s\pi a}{h}\right)}e^{in\theta} & \text{if } s \neq 0 \quad n \in \mathbb{Z} \\ \frac{gH}{\omega}\frac{1}{2}\left(\frac{r}{a}\right)^{|n|}e^{in\theta} & \text{if } s = 0 \quad n \in \mathbb{Z} \end{cases} \tag{2.42}$$

2.2.3 Incident wave basis

In this section, we describe the waves that are incident to the body neglecting completely the presence of the body. This incident wavefield is described by incident wavefield potential. To compute this potential we solve the Laplace equation, first in the exterior region, and afterward in the interior region, following the same logical order as in subsection 2.2.2. Now, the boundary conditions are different from the one in subsection 2.2.2, which is the reason why we will get a different solution.

We start by detailing the ambient wave, which are the incident waves to a body coming from the ambient in the form of monochromatic planar waves. We are allowed to consider monochromatic waves because of the linear nature of our problem. Afterward, we also consider the contribution to the incident wave due to the scattered and radiated waves from other bodies. Similarly to before, we use the separation of variable approach to define the incident potential,

$$\phi_I = \sigma_r(r)\,\sigma_\theta(\theta)\,\sigma_z(z)\,. \tag{2.43}$$

Ambient

For ambient waves, we choose not to switch to polar coordinates, since a planar wave is more naturally described in x, y, z coordinates. After applying the separation of variables in x, z (note that a planar wave traveling in the x-direction has no y-dependence), applying boundary conditions, and considering only the progressive case we get the solution to be

$$\phi_A = C_A e^{ik_0 x} N_0^{-\frac{1}{2}} \cosh(k_0 z), \quad C_A \in \mathbb{C}. \tag{2.44}$$

Note that we are considering only the progressive case, because the evanescent case is related to the non-ambient component of the incident wave.

Applying the free surface dynamic boundary condition

$$\frac{\partial \phi}{\partial t} = -gH \cos\Big(kx - \omega t + \frac{\pi}{2}\Big), \tag{2.45}$$

we compute the value of the C_A coefficient. Plugging C_A into the previous equation gives

$$\phi_A = \frac{gH}{\omega} \frac{\cosh(k_0 z)}{\cosh(k_0 d)} e^{ik_0 x}. \tag{2.46}$$

This expression, thanks to the identity [33] $e^{\frac{1}{2}z\left(t-\frac{1}{t}\right)} = \sum_{k=-\infty}^{\infty} t^k J_k(z)$, is rewritten in polar coordinates centered on the device, and the x-traveling wave is set to travel in any arbitrary direction tilted by β with respect to the x direction modifying the θ-exponent term,

$$\phi_A = \frac{gH}{\omega} \frac{\cosh(k_0 z)}{\cosh(k_0 d)} \sum_{n=-\infty}^{\infty} J_n(k_0 r)\, e^{i\left(\frac{\pi}{2}+\theta-\beta\right)}. \tag{2.47}$$

The complete ambient wave is in (2.47) expressed as a sum of infinite terms. The accuracy of this expansion is greater the larger the number of considered terms. For computational reasons, it is impossible to use an infinite amount of terms, which would guarantee a complete representation. Hence, we wrote a code to investigate how many terms are necessary to have a good approximation of the incident wave. Analyzing the free-surface displacement as the real part of a rotating vector, we plot its absolute value in figure 2.2, and its real part in figure 2.3, varying the number of θ-modes used. We can see that a clear improvement in precision is obtained by increasing the number of θ-modes. It has to be noted that, when we have to consider to which number of θ-modes we want to limit our analysis, we must focus only on enforcing that in the region around the position of the body we have a good representation of the incident flowfield. Therefore, despite being interesting to notice how using $n = 30$ θ-modes we get almost no error in most of the domain, the actual number of θ-modes necessary is definitely smaller. Later on, to actually choose the number of modes to use in our simulations, we will perform a convergence analysis. This will give more useful and less qualitative information.

Complete incident wave basis

The incident waves to each device do not only come from the ambient, but also from the interaction of the ambient waves with other bodies. This will be later exhaustively detailed in subsection 2.3.1, and in subsection 2.3.1. Taking into account this additional contribution, we get the complete formulation of a set of basis functions,

$$(\phi_I)_n^m = \begin{cases} \frac{gH}{\omega}\frac{\cosh(k_0 z)}{\cosh(k_0 d)} J_n(k_0 r)\, i^n e^{in\theta} & \text{if } m = 0, \quad n \in \mathbb{Z}, \\ \frac{gH}{\omega}\cos(k_m z) I_n(k_m r)\, e^{in\theta} & \text{if } m \geq 0, \quad n \in \mathbb{Z}. \end{cases} \tag{2.48}$$

2.2.4 Diffracted wave basis

In this section, we construct a basis of functions for the diffracted wave potential. We remind that diffracted waves are defined as the composition of the scattered wave from a device and the incident wave to it.

The same logical structure of subsections 2.2.2 and 2.2.3 is also applied here. First, we describe the behavior in the exterior region, and afterward, the behavior in the interior region. To complete our description of the diffracted wavefield, we have to compute some later defined coefficients. The method through which we do so is explained at the end of this section.

Exterior region

Considering an incident wave of θ-mode n, and z-mode m, we have that, since our body is radially symmetric, the resulting scattered wavefield maintains the same radial dependence as the incident wave that generates it. This means that

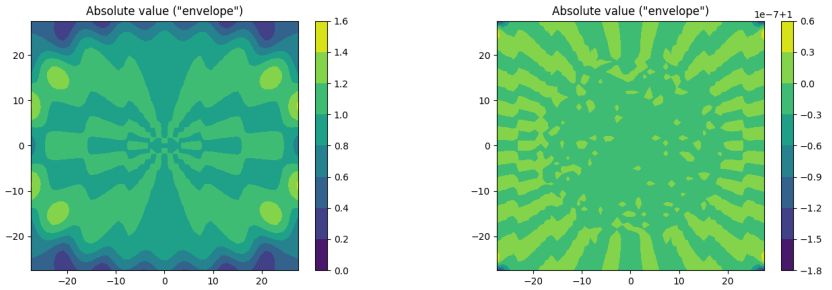

Figure 2.2: Absolute value of the free-surface displacement vector using $n = 10$ θ-modes for a wave of $\omega = 2\frac{rad}{s}$ in a sea of depth $d = 30$ m, compared to the case of $n = 30$ with the other parameters kept fixed.

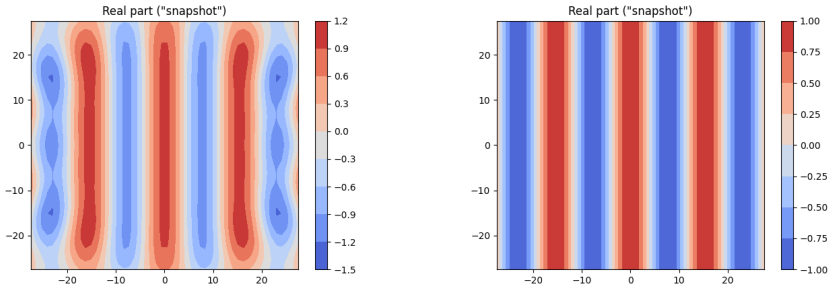

Figure 2.3: Real part of the free-surface displacement vector using $n = 10$ θ-modes for a wave of $\omega = 2$ $\frac{rad}{s}$ in a sea of depth $d = 30$ m, compared to the case of $n = 30$ with the other parameters kept fixed.

the diffracted wavefield, generated from the previously described incident wave, can be mathematically represented as follows:

$$(\phi_D)_n^m = \frac{gH}{\omega}\chi_n^m(r,z)\,e^{in\theta}, \tag{2.49}$$

where the radial and depth dependence is encapsulated in the χ function. To compute the χ function explicitly, we must notice that we already developed a set of basis functions for any scattered potential (2.31). Hence, to compute the scattered potential generated by the selected incident wave, we simply need to do a linear combination of the previously obtained basis functions. The resulting χ-function, for the progressive case in the exterior region, takes the form

$$\begin{aligned}\chi_n^0 = i^n \frac{\cosh(k_0 z)}{\cosh(k_0 d)}\left(J_n(k_0 r) - \frac{J_n'(k_0 a)}{H_n'(k_0 a)}H_n(k_0 r)\right) + \\ + D_{00}^n N_0^{-\frac{1}{2}}\cosh(k_0 z)\frac{H_n(k_0 r)}{H_n(k_0 a)} + \sum_{q=1}^{\infty} D_{q0}^n N_q^{-\frac{1}{2}}\cos(k_q z)\frac{K_n(k_q r)}{K_n'(k_q a)}.\end{aligned} \tag{2.50}$$

The first term in the equation represents the incident wave. We added a term in bracket to simplify the further computation of the D coefficients, when applying condition (2.61). This additional term does not affect the final result, since using the appropriate value of the D_{00}^n coefficient, we can account for its presence. Meanwhile, all the other terms that are multiplied times a D_{00}^n or a D_{q0}^n complex coefficient, represent the previously mentioned linear combination.

In a similar manner, we represent the evanescent part of the solution as

$$\begin{aligned}\chi_n^m = \cos(k_m z)\left(I_n(k_m r) - \frac{I_n'(k_m a)}{K_n'(k_m a)}K_n(k_m r)\right) + \\ + D_{0m}^n N_0^{-\frac{1}{2}}\cosh(k_0 z)\frac{H_n(k_0 r)}{H_n(k_0 a)} + \sum_{q=1}^{\infty} D_{qm}^n N_q^{-\frac{1}{2}}\cos(k_q z)\frac{K_n(k_q r)}{K_n'(k_q a)}.\end{aligned} \tag{2.51}$$

Interior region

For the interior region, the same consideration on the radial symmetry of the body holds. Hence, the diffracted potential in the interior region is

$$\left(\tilde{\phi}_D\right)_n^m = \frac{gH}{\omega}\tilde{\chi}_n^m(r,z)\,e^{in\theta}. \tag{2.52}$$

For the $\tilde{\chi}$-function, we use the same approach as before, noting that the incident wavefield gives no contribution in this region. The expression of $\tilde{\chi}$ takes the following form:

$$\tilde{\chi}_n^m = \frac{C_{0m}^n}{2}\left(\frac{r}{a}\right)^{|n|} + \sum_{s=1}^{\infty} C_{sm}^n \cos\left(\frac{s\pi z}{h}\right)\frac{I_n\left(\frac{s\pi r}{h}\right)}{I_n\left(\frac{s\pi a}{h}\right)}. \tag{2.53}$$

Again, all the C^n_{0m} and C^n_{sm} coefficients are needed for the linear combination of the previously computed basis functions of the scattered potential in the interior region (2.42), and are complex quantities.

Coefficients computation

Equations (2.50), (2.51), and (2.53) are linear combinations of the basis functions of the scattered potential. For now, we have not yet provided an expression for the D^n_{00}, D^n_{q0}, C^n_{0m} and C^n_{sm} coefficients used to make these linear combinations. Therefore, in this section, we focus on how to compute these coefficients by exploiting the orthogonality of the depth functions, and the continuity of the solution across the interior and exterior region.

Orthogonality of the depth functions holds

$$\frac{1}{d}\int \sigma^q_z(z)\,\sigma^m_z(z)\,dz = \begin{cases} 1 & \text{if } q = m, \\ 0 & \text{if } q \neq m. \end{cases} \tag{2.54}$$

$$\frac{2}{h}\int_0^h \sigma^s_z(z)\cos\Big(\frac{m\pi z}{h}\Big)dz = \begin{cases} 1 & \text{if } s = m, \\ 0 & \text{if } s \neq m. \end{cases} \tag{2.55}$$

Using this property, we write the following expressions for the coefficients:

$$C^n_{sm} = \frac{2}{h}\int_0^h \tilde{\chi}^n_m(a,z)\cos\Big(\frac{s\pi z}{h}\Big)\,dz, \tag{2.56}$$

$$D^n_{0m} = \frac{1}{k_0 d}\int_0^d \frac{\partial \chi^n_m}{\partial r}(a,z)\,N_0^{-\frac{1}{2}}\cosh(k_0 z)\,dz, \tag{2.57}$$

$$D^n_{qm} = \frac{1}{k_q d}\int_0^d \frac{\partial \chi^n_m}{\partial r}(a,z)\,N_q^{-\frac{1}{2}}\cos(k_q z)\,dz. \tag{2.58}$$

This is clearly not enough to explicitly compute the values of the coefficients, because they are still hidden inside the χ functions. Now, we impose continuity of the solution in our domain. To do so, we require the solution to match at the interface between the exterior and interior regions imposing

$$\chi^n_m = \tilde{\chi}^n_m \qquad r = a, \quad 0 \leq z \leq h, \tag{2.59}$$

$$\frac{\partial \chi^n_m}{\partial r} = \frac{\partial \tilde{\chi}^n_m}{\partial r} \qquad r = a, \quad 0 \leq z \leq h, \tag{2.60}$$

$$\frac{\partial \chi^n_m}{\partial r} = 0 \qquad r = a, \quad h \leq z \leq d. \tag{2.61}$$

Now, we plug the expressions of the χ expansions (2.50), (2.51) and (2.53), into the equations obtained thanks to the orthonormality condition (2.56), (2.57) and (2.58), properly using the matching conditions (2.59), (2.60) and (2.61), to prevent ending up with identities. An example of a wrong substitution that generates an identity is plugging (2.53) into (2.56).

This procedure leads us, after switching the order of integral and summation, to non null products of cosine and hyperbolic cosine, that are explicitly computed using the relations

$$\int_0^h \cos\Big(\frac{s\pi z}{h}\Big)\cosh\left(k_0 z\right)dz = \frac{k_0\left(-1\right)^s\sinh\left(k_0 h\right)}{k_0^2+\left(\frac{s\pi}{h}\right)^2}, \tag{2.62}$$

$$\int_0^h \cos\Big(\frac{s\pi z}{h}\Big)\cos\left(k_q z\right)dz = \frac{k_q\left(-1\right)^s\sin\left(k_q h\right)}{k_q^2-\left(\frac{s\pi}{h}\right)^2}. \tag{2.63}$$

A further level of simplification is obtained by using the Wronskian identities

$$K_n'(x)\,I_n(x) - I_n'(x)\,K_n(x) = -\frac{1}{x}, \tag{2.64}$$

$$H_n'(x)\,J_n(x) - J_n'(x)\,H_n(x) = -\frac{2i}{\pi x}, \tag{2.65}$$

which allow us the write the final linear systems of equations for the computation of the coefficients as

$$C_{sm}^n + \sum_{q=0}^{\infty} E_{sq}^n D_{qm}^n = U_{sm}^n, \tag{2.66}$$

$$D_{qm}^n = \sum_{s=0}^{\infty} G_{qs}^n C_{sm}^n. \tag{2.67}$$

Where all the E, G, U coefficients are computed using the previously mentioned relations, explicitly we have

$$E_{sq}^n = \begin{cases} -\frac{2}{h}\frac{H_n(k_0 a)}{H_n'(k_0 a)}\frac{h^2 k_0(-1)^s\sinh\left(k_0 h\right)}{N_0^{\frac{1}{2}}\left(s^2\pi^2+k_0^2h^2\right)} & s\geq 1,\quad q=0,\\ -\frac{2}{h}\frac{K_n(k_q a)}{K_n'(k_q a)}\frac{h^2 k_q(-1)^s\sin\left(k_q h\right)}{N_q^{\frac{1}{2}}\left(s^2\pi^2+k_q^2h^2\right)} & s\geq 1,\quad q\geq 1, \end{cases} \tag{2.68}$$

$$G_{sq}^n = \begin{cases} \frac{|n|\sinh\left(k_0 h\right)}{2ak_0^2 dN_0^{\frac{1}{2}}} & s=0,\quad q=0,\\ \frac{|n|\sin\left(k_q h\right)}{2ak_q^2 dN_q^{\frac{1}{2}}} & s=0,\quad q\geq 1,\\ \frac{I_n'\left(\frac{s\pi a}{h}\right)}{I_n\left(\frac{s\pi a}{h}\right)}\frac{s\pi h(-1)^s\sinh\left(k_0 h\right)}{N_0^{\frac{1}{2}}\,d\left(s^2\pi^2+k_0^2h^2\right)} & s\geq 1,\quad q=0,\\ \frac{I_n'\left(\frac{s\pi a}{h}\right)}{I_n\left(\frac{s\pi a}{h}\right)}\frac{s\pi h(-1)^s\sin\left(k_q h\right)}{N_q^{\frac{1}{2}}\,d\left(-s^2\pi^2+k_q^2h^2\right)} & s\geq 1,\quad q\geq 1, \end{cases} \tag{2.69}$$

$$U_{sm}^n = \begin{cases} \frac{4i^{n+1}(-1)^s h\sinh\left(k_0 h\right)}{\pi a\left(s^2\pi^2+k_0^2h^2\right)H_n'(k_0 a)\cosh\left(k_0 d\right)} & s\geq 0,\quad m=0,\\ \frac{2h(-1)^{s+1}h\sin\left(k_m h\right)}{a(-s^2\pi^2+k_m^2h^2)K_n'(k_m a)} & s\geq 0,\quad m\geq 1. \end{cases} \tag{2.70}$$

2.2.5 Radiated wave basis

In this section, we construct a basis of functions for the radiated potential. The radiated potential is the contribution to the total potential generated by the vertical movement of a body in absence of incident waves. To compute the radiated potential, we distinguish again between exterior and interior regions, and we give particular attention to the way we compute some necessary coefficients, as we did for the diffracted potential in subsection 2.2.4.

Exterior region

Given the linear nature of our governing equations, the radiated potential is proportional to the body vertical displacement X. We actually use a nondimensional displacement $\hat{X}$ to represent this proportionality relation. We represent the displacement and its derivatives as functions of the nondimensional displacement through the relations

$$X = H\hat{X}, \tag{2.71}$$

$$X' = -i\omega H\hat{X}, \tag{2.72}$$

$$X'' = \omega^2 H\hat{X}. \tag{2.73}$$

On top of the proportionality of the radiated potential to the displacement of the body, we affirm that, since our body is axial-symmetric, the radiated potential has no angular dependence. The general expression for the radiated potential hence becomes

$$\phi_R = \frac{gH}{\omega}\hat{X}R(r,z)\,. \tag{2.74}$$

Now considering the boundary conditions, satisfied by the governing equations in the exterior region, they are the same both for the radiated and the scattering case. Hence, we can write the solution for the radiated field in the exterior region as a linear combination of the previously defined basis functions of the scatter waves in the exterior region (2.31). Keeping in mind that there is no angular dependence, hence $n = 0$, we get our R-function in the radiated potential to be

$$R\,(r,z) \;=\; D_0^R N_0^{-\frac{1}{2}} \cosh\,(k_0 z)\frac{H_0(k_0 r)}{H_0'(k_0 a)} \;+\; \sum_{q=1}^{\infty} D_q^R N_q^{-\frac{1}{2}} \cos\,(k_q z)\frac{K_0(k_q r)}{K_0'(k_q a)}. \tag{2.75}$$

Interior region

For the interior region, in addition to what we have already done for the scattered wave basis development, we must also consider the condition imposed by the vertical movement of the body. We define as $\tilde{R}_h$ the homogeneous part of the solution, obtained when the body is kept still, and with $\tilde{R}_p$ the particular part of the solution, obtained by imposing the boundary condition (2.6). The general solution in the inner region is

$$\tilde{\phi}_R = \frac{gH}{\omega} \hat{X} \tilde{R}(r,z)\,, \tag{2.76}$$

$$\tilde{R} = \tilde{R}_h + \tilde{R}_p. \tag{2.77}$$

For the homogeneous part, the problem is the same as the scattered potential problem in the interior region, but considering only the radially symmetric cases, $n = 0$. Hence, we write a linear combination of the basis functions (2.42),

$$\tilde{R}_h = \frac{C_0^R}{2} + \sum_{s=1}^{\infty} C_s^R \cos\left(\frac{s\pi z}{h}\right) \frac{I_0\left(\frac{s\pi r}{h}\right)}{I_0\left(\frac{s\pi a}{h}\right)}. \tag{2.78}$$

For this particular part, we simply have to find a solution that is compatible with the boundary conditions, and such a solution can be verified to be

$$\tilde{R}_p = -\frac{i\omega^2}{2gh}\left(z^2 - \frac{r^2}{2}\right). \tag{2.79}$$

Coefficients computation

Same as for subsection 2.2.4, we have to explicitly compute the values of all the coefficients we used while doing the linear combination of the scattered potential's basis functions. To do so we once again exploit the orthogonality of the depth functions and the matching conditions at the interface between the interior and exterior regions. Orthogonality holds

$$C_s^R = \frac{2}{h}\int_0^h \tilde{R}(a,z)\cos\left(\frac{s\pi z}{h}\right) dz, \tag{2.80}$$

$$D_0^R = \frac{1}{k_0 d}\int_0^d \frac{\partial R}{\partial r}(a,z)\, N_0^{-\frac{1}{2}} \cosh\left(k_0 z\right) dz, \tag{2.81}$$

$$D_q^R = \frac{1}{k_q d}\int_0^d \frac{\partial R}{\partial r}(a,z)\, N_q^{-\frac{1}{2}} \cos\left(k_q z\right) dz. \tag{2.82}$$

The matching conditions hold

$$R = \tilde{R} \quad r = a, 0 \leq z \leq h, \tag{2.83}$$

$$\frac{\partial R}{\partial r} = \frac{\partial \tilde{R}}{\partial r} \quad r = a, 0 \leq z \leq h, \tag{2.84}$$

$$\frac{\partial R}{\partial r} = 0 \quad r = a, h \leq z \leq d. \tag{2.85}$$

We now proceed along the same line of section 2.2.4. We plug the expansions (2.75), (2.78) and the expression (2.79), into the definitions of the coefficients (2.80), (2.81) and (2.82). In doing so, we use the matching conditions (2.83), (2.84), (2.85), and the definition of the solution as the sum of homogeneous and particular contribution to avoid ending up with identities. The main difference is the presence of the particular solution, which results in the appearance of the following integral that is solved by a double integration by parts:

$$\int_0^h z^2 \cos\left(\frac{s\pi z}{h}\right) dz = \frac{2h^3 (-1)^s}{(s\pi)^2}. \tag{2.86}$$

All the other terms are straightforwardly integrated leading to the linear systems of equations

$$C_s^R + \sum_{q=0}^{\infty} E_{sq}^0 D_q^R = Q_s^R, \tag{2.87}$$

$$D_q^R = S_q^R + \sum_{s=0}^{\infty} G_{qs}^0 C_s^R. \tag{2.88}$$

Where E_{sq}^0 and G_{sq}^0 are defined in the same way as for the diffracted wave basis analysis in (2.68) and (2.69). The other coefficients take the following form:

$$Q_s^R = \begin{cases} \frac{i\omega^2}{gh}\left(\frac{h^2}{3} - \frac{a^2}{2}\right) & s = 0, \\ \frac{2i\omega^2 h(-1)^s}{gs^2\pi^2} & s \geq 1, \end{cases} \tag{2.89}$$

$$S_q^R = \begin{cases} \frac{ia\omega^2}{2k_0^2 dgh N_0^{\frac{1}{2}}} \sinh(k_0 h) & q = 0, \\ \frac{ia\omega^2}{2k_q^2 dgh N_q^{\frac{1}{2}}} \sin(k_q h) & q \geq 1. \end{cases} \tag{2.90}$$

2.3 Array

Now that we completed the description of the behavior of a single device, we have to analyze how the interaction between an array of devices and an incident wave develops.

We start by introducing a new notation, called *partial wave* notation, that allows us to write a linear combination of basis functions in a more compact form. This notation shows its usefulness once we numerically implement the

previously developed equations, since it allows us to reduce the complex problem we are describing to a simple matrix-vector multiplication. Afterward, we analyze how to reinterpret radiated and scattered waves from a body as incident waves to another body. This allows us to obtain the most general incident wave approaching a body. The following step is computing the potential all around the body, which is given by the complete incident wave, and its interaction with the body. We focus in greater detail on the computation of the distribution of pressure on the bottom surface of the cylinder, and we use it to compute its equation of motion. In the last part of this section, known the equation of motion of our body, we compute many useful derived quantities, such as the amount of power that each device is able to extract from the waves, and the interaction factor. The interaction factor is particularly interesting because, as it is later better detailed, it represents to which degree using devices placed in an array is more convenient than using them isolated from each other.

2.3.1 Partial wave notation

Having computed the basis functions for the various potentials adding up the complete potential ϕ, it is necessary, to solve the problem, to compute the coefficients of the linear combinations of the above-mentioned functions. To make this task easier, we introduce the partial wave notation, which allows us to write the linear combination in a more compact way. Using the partial wave notation consists in listing all the basis functions in a vector, so that to make a linear combination we simply have to perform a dot product between the partial wave vector, and a vector of coefficients. The order in which the functions are listed in the vector is not relevant, as long as it is kept consistent throughout the theory development, especially in the numerical implementation. An additional subscript is added to indicate to which body we are referring to.

For the scattered waves in the exterior region, the partial wave vector of θ-mode n and z-mode m is

$$\left(\Psi_i^S\right)_m^n = \begin{cases} \frac{\cosh(k_0 z)}{\cosh(k_0 d)} \frac{H_n(k_0 r_i)}{H_n(k_0 a)} e^{in\theta_i} & \text{if } m = 0, \quad n \in \mathbb{Z}, \\ \cos(k_m z) \frac{K_n(k_m r_i)}{K_n(k_m a)} e^{in\theta_i} & \text{if } m \geq 1, \quad n \in \mathbb{Z}. \end{cases} \tag{2.91}$$

For the incident waves in the exterior region, it is

$$\left(\Psi_i^I\right)_m^n = \begin{cases} \frac{\cosh(k_0 z)}{\cosh(k_0 d)} \frac{J_n(k_0 r_i)}{J_n(k_0 a)} e^{in\theta_i} & \text{if } m = 0, \quad n \in \mathbb{Z}, \\ \cos(k_m z) \frac{I_n(k_m r_i)}{I_n(k_m a)} e^{in\theta_i} & \text{if } m \geq 1, \quad n \in \mathbb{Z}. \end{cases} \tag{2.92}$$

For the diffracted wave in the interior region, it is

$$\left(\tilde{\Psi}_i^D\right)_m^n = \begin{cases} \left(\frac{r_i}{a}\right)^{|n|} e^{in\theta_i} & \text{if } m = 0, \quad n \in \mathbb{Z}, \\ \cos\frac{(m\pi z)}{h_i} \frac{I_n\left(\frac{m\pi r_i}{h}\right)}{I_n\left(\frac{m\pi a}{h}\right)} e^{in\theta_i} & \text{if } m \geq 1, \quad n \in \mathbb{Z}. \end{cases} \tag{2.93}$$

Ambient wave on j-th body

Having multiple bodies in an array, a periodic wave is perceived with a different phase by each of them. The phase shift is given by the relative position of each body.

Having as a reference figure 2.4, we have that the phase-shift in exponential form is equal to

$$I_j = e^{ik_0(x_j \cos(\beta) + y_j \sin(\beta))}. \tag{2.94}$$

Hence, the vector of coefficients that multiplies the incident wave partial wave vector is

$$(a_j)_m^n = \begin{cases} I_j J_n(k_0 a_j)\, e^{in\left(\frac{\pi}{2}-\beta\right)} & \text{if } m = 0, \quad n \in \mathbb{Z}, \\ 0 & \text{if } m \geq 0, \quad n \in \mathbb{Z}. \end{cases} \tag{2.95}$$

The ambient wave potential, written using the partial wave notation, is

$$\phi_j^A = \frac{gH}{\omega} a_j^T \Psi_j^I \tag{2.96}$$

Scattered waves from i-th body

Now, we apply the partial wave notation to the scattered potential. The scattered potential for the generic i-th body becomes

$$\phi_i^S = \frac{gH}{\omega} A_i^T \Psi_i^S. \tag{2.97}$$

Now, using Graff's addition formulae

$$H_n(k_0 r_i)\, e^{in\theta_i} = \sum_{l=-\infty}^{\infty} H_{n+l}(k_0 L_{ij})\, J_l(k_0 r_j)\, e^{i(\alpha_{ij}(l+n)+l(\pi-\theta_j))}, \tag{2.98}$$

$$K_n(k_m r_i)\, e^{in\theta_i} = \sum_{l=-\infty}^{\infty} K_{n+l}(k_m L_{ij})\, I_l(k_0 r_j)\, e^{i(\alpha_{ij}(l+n)+l(\pi-\theta_j))}, \tag{2.99}$$

we define a linear operator that re-scales the coefficients of the partial wave vector of the scattered wave by body i, into the coefficients of the partial wave vector of an incident wave perceived by body j.

This coordinate transformation matrix is defined for every pair of bodies, such that $i \neq j$. We also notice that this transformation does not affect the z-mode m. Hence, the transformation of the scattered wave of θ-mode n into the incident waves of θ-mode l takes the form

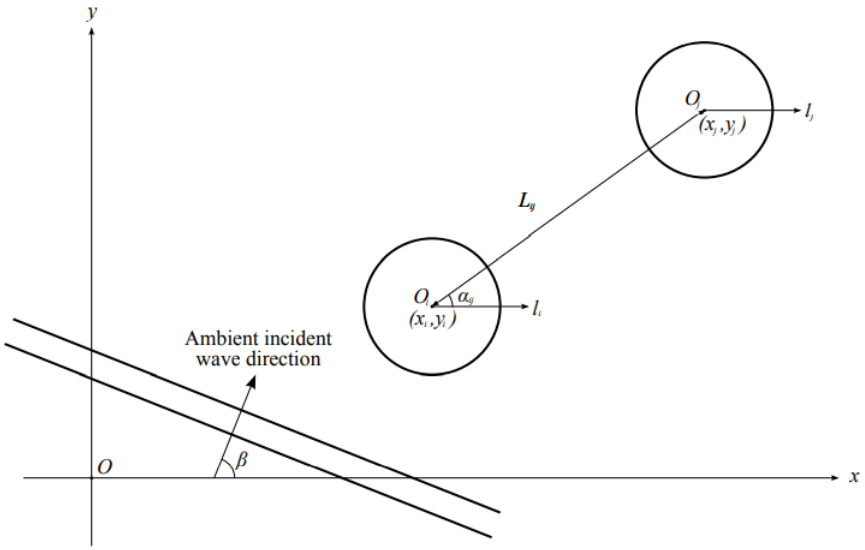

Figure 2.4: Vertical view of two devices with relevant parameters highlighted. Here, β is the angle formed by the ambient wave with the positive x-direction, (x_i, y_i) and (x_j, y_j) are the coordinates of body i and body j respectively, and L_{ij} is the distance between the two bodies. Figure from [6].

$$(T_{ij})^{nl}_{mm} = \begin{cases} \frac{J_l(k_0 a)}{H_n(k_0 a)} H_{n-l}(k_0 L_{ij})\, e^{i\alpha_{ij}(n-l)} & \text{if } m = 0, \quad n, l \in \mathbb{Z}, \\ \frac{I_l(k_m a)}{K_n(k_m a)} K_{n-l}(k_m L_{ij})\, e^{i\alpha_{ij}(n-l)}\, (-1)^l & \text{if } m \geq 1, \quad n, l \in \mathbb{Z}, \end{cases} \tag{2.100}$$

We wrote a code that investigates this transformation. In figure 2.5, we show how, for different numbers of θ-modes, the modulus of the rotating vector, representing the free-surface displacement, varies in the space, because of the scattered wave produced by a body placed in coordinates $(0, -10)$. In figure 2.6, we show how the same vector's modulus is reconstructed using the coefficient of the incident wavefield to a second body placed in coordinates $(0, 10)$. We notice that in some regions the result diverges, but this is of little relevance, since we care about reconstructing reliably the scattered potential as incident, only in the region close to the second body. We also see a clear increase in accuracy increasing the number of θ-modes n. This increase in accuracy is especially highlighted by looking at how, for the case with a high number of θ-modes, a much more distinct circular pattern is showcased. This circular pattern is a well-known property of the wavefield scattered from cylindrical bodies subject to planar waves [25], and it is here displayed once again.

By definition of the T_{ij} matrix we get

$$\Psi_i^S = T_{ij} \Psi_j^I. \tag{2.101}$$

Furthermore, the scattered potential generated by the i-th body (2.97), is written as perceived as incident by the j-th body using the following notation:

$$\phi_i^S \big|_j = \frac{gH}{\omega} A_i^T T_{ij} \Psi_j^I. \tag{2.102}$$

At this point, since the scattered and diffracted potential in the inner region are equivalent, we write, using partial wave notation, the diffracted potential in the inner region as

$$\tilde{\phi}_i^D = \frac{gH}{\omega} \tilde{A}_i^T \tilde{\Psi}_i^D. \tag{2.103}$$

Radiated waves from i-th body

We now proceed in a similar way to the previous section, first rewriting the radiated potential in partial wave notation, and second, reinterpreting the radiated waves emitted by one body as incident waves perceived by another one. Having each body an independent degree of freedom to allow the vertical displacement, we rewrite the radiated potential in the exterior region from the generic i-th body as

$$\phi_i^R = \frac{gH}{\omega} \hat{X}_i R_i^T \Psi_i^S. \tag{2.104}$$

Regarding the interior region, we have, same as for the single body case, that the solution is given by the sum of the homogeneous and particular solutions,

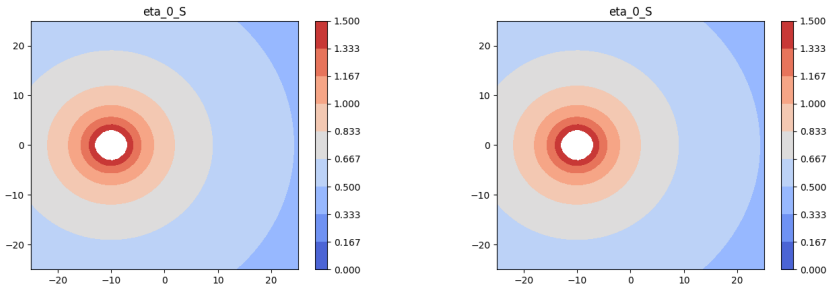

Figure 2.5: On the right, the absolute value of the free-surface displacement vector, generated by a scattered wave, represented using $n = 7$ θ-modes, born from the interaction of an incident wave of $\omega = 1\ \frac{rad}{s}$ and $\beta = 0\ rad$ with a body of radius $a = 4\ m$, draft $d - h = 0.5\ m$, positioned in a sea of depth $d = 10\ m$ at coordinates $(0, -10)\ m$. On the left, the case with $n = 30$ and the other parameters kept fixed.

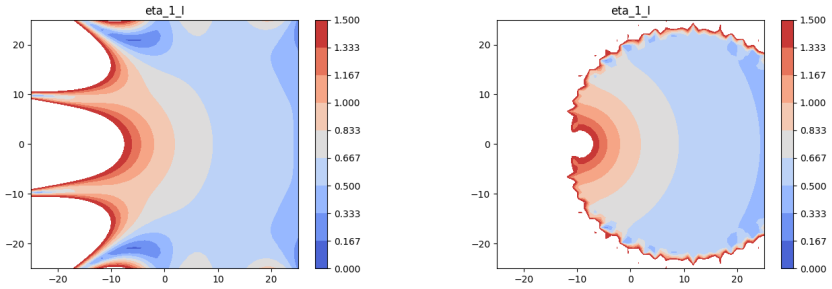

Figure 2.6: The absolute value of the same free-surface displacement vector as in figure 2.5, but reconstructed, through the matrix T_{ij}, using the coefficient of the incident wave basis of a second body with the same parameters as the first one, placed at coordinates $(0, 10)\ m$. Left and right are consistent with image 2.5.

$$\tilde{R}_i = \tilde{R}_i^h + \tilde{R}_i^p. \tag{2.105}$$

The homogeneous part is expressed as a linear combination of the scattered wave basis functions in the interior region, which are the same as the diffracted basis functions in the interior region. Using the partial wave notation we have

$$\tilde{R}_i^h = \tilde{R}_i^T \tilde{\Psi}_i^D. \tag{2.106}$$

Hence, the radiated potential in the inner region becomes

$$\tilde{\phi}_i^R = \frac{gH}{\omega} \hat{X}_i \left(\tilde{R}_i^p + \tilde{R}_i^T \tilde{\Psi}_i^D \right). \tag{2.107}$$

Using again the coordinate transformation matrix 2.100, we interpret the radiated field in the exterior region from body i as the perceived incident field to body j writing

$$\phi_i^R\big|_j = \frac{gH}{\omega} \hat{X}_i R_i^T T_{ij} \Psi_i^I. \tag{2.108}$$

2.3.2 Scattering equation

Having interpreted both the radiated and the scattered potential from one body as the incident potential to another, we now combine all the previously described incident potentials to obtain a complete incident potential description. By doing so, we obtain that the total incident potential is

$$\phi_j^I = \frac{gH}{\omega} \left(a_j^T + \sum_{i=1}^{N} \left(A_i + \hat{X}_i R_i \right)^T T_{ij} \right) \Psi_j^I. \tag{2.109}$$

Having a wave described by this incident potential approaching a body, we are now interested in computing the scattered potential from this body after its interaction with this wave. To do so, we define a linear operator B, which encapsulates the ratios of the coefficient of Ψ_j^S and those of Ψ_j^I. This operator is called *exterior diffraction transfer matrix*, and allows us to compute the coefficients A_j of Ψ_j^S as follows:

$$A_j = B_j \left(a_j + \sum_{i=1}^{N} T_{ij}^T \left(A_i + \hat{X}_i R_i \right) \right). \tag{2.110}$$

The B matrix is characteristic for each device, and since our body is radially symmetric, it has zero entries for the coefficient relating different θ-modes of the incident and scattered potential. The entries for the B matrix are

$$(B)_{qm}^{nn} = \begin{cases} \frac{H_n(k_0a)}{J_n(k_0a)}\left(-\frac{J_n'(k_0a)}{H_n'(k_0a)} + i^{-n}\frac{D_{00}^n \cosh(k_0d)}{N_0^{\frac{1}{2}} H_n'(k_0a)}\right) & \text{if } m=0, \quad q=0, \quad n\in\mathbb{Z}, \\ \frac{K_n(k_qa)}{J_n(k_0a)}\left(i^{-n}\frac{D_{q0}^n}{N_q^{\frac{1}{2}} K_n'(k_qa)}\right) & \text{if } m=0, \quad q\geq 0, \quad n\in\mathbb{Z}, \\ \frac{H_n(k_0a)}{I_n(k_ma)}\left(\frac{D_{0m}^n \cosh(k_0d)}{N_0^{\frac{1}{2}} H_n'(k_0a)}\right) & \text{if } m\geq 1, \quad q=0, \quad n\in\mathbb{Z}, \\ \frac{K_n(k_qa)}{I_n(k_ma)}\left(\frac{D_{qm}^n}{N_q^{\frac{1}{2}} K_n'(k_qa)}\right) & \text{if } m\geq 1, \quad q\neq(0,m), \quad n\in\mathbb{Z}, \\ \frac{K_n(k_ma)}{I_n(k_ma)}\left(-\frac{I_n'(k_ma)}{K_n'(k_ma)} + \frac{D_{mm}^n}{N_m^{\frac{1}{2}} K_n'(k_ma)}\right) & \text{if } m\geq 1, \quad q=m, \quad n\in\mathbb{Z}. \end{cases} \tag{2.111}$$

Similarly, we define an *interior diffraction transfer matrix*, that represents the ratio between the coefficients of the same complete incident wave-field to those of the basis functions of the diffracted potential in the inner region. Thanks to this matrix, we write the following expression for the $\tilde{A}_j$ coefficient of the diffracted partial waves in the inner region:

$$\tilde{A}_j = \tilde{B}_j\left(a_j + \sum_{i=1}^{N} T_{ij}^T\left(A_i + \hat{X}_i R_i\right)\right). \tag{2.112}$$

The entries of the inner diffraction transfer matrix are

$$\left(\tilde{B}\right)_{qm}^{nn} = \begin{cases} \frac{H_n(k_0a)}{J_n(k_0a)}\left(-\frac{J_n'(k_0a)}{H_n'(k_0a)} + i^{-n}\frac{D_{00}^n \cosh(k_0d)}{N_0^{\frac{1}{2}} H_n'(k_0a)}\right) & \text{if } m=0, \quad q=0, \quad n\in\mathbb{Z}. \\ \frac{K_n(k_qa)}{J_n(k_0a)}\left(i^{-n}\frac{D_{q0}^n}{N_q^{\frac{1}{2}} K_n'(k_qa)}\right) & \text{if } m=0, \quad q\geq 0, \quad n\in\mathbb{Z}, \\ \frac{H_n(k_0a)}{I_n(k_ma)}\left(\frac{D_{0m}^n \cosh(k_0d)}{N_0^{\frac{1}{2}} H_n'(k_0a)}\right) & \text{if } m\geq 1, \quad q=0, \quad n\in\mathbb{Z}, \\ \frac{K_n(k_qa)}{I_n(k_ma)}\left(\frac{D_{qm}^n}{N_q^{\frac{1}{2}} K_n'(k_qa)}\right) & \text{if } m\geq 1, \quad q\neq(0,m), \quad n\in\mathbb{Z}, \\ \frac{K_n(k_ma)}{I_n(k_ma)}\left(-\frac{I_n'(k_ma)}{K_n'(k_ma)} + \frac{D_{mm}^n}{N_m^{\frac{1}{2}} K_n'(k_ma)}\right) & \text{if } m\geq 1, \quad q=m, \quad n\in\mathbb{Z}. \end{cases} \tag{2.113}$$

2.3.3 Equation of motion

In this section, we look into the derivation of the equation of motion of a body. We model the power take-off of our device through a linear spring-damper system, upon which act the external forces.
We start by computing the contribution to the force due to pressure on the bottom face of the cylinder. This pressure is composed by two contribution, the static and dynamic pressure,

$$p_F = p_S + p_D. \tag{2.114}$$

The static contribution grows linearly with the negative z-direction, and at the bottom face of the cylinder adds up to

$$p_S = \rho g \left(d - (h + X)\right). \tag{2.115}$$

The dynamic pressure is instead related to the potential describing the velocity field through the following relation:

$$p_D = -\rho \left.\frac{\partial \phi}{\partial t}\right|_{z=h}. \tag{2.116}$$

The resulting force, due to these two pressure contributions, is given by integrating them on the bottom face of the cylinder,

$$F_j^F = -\iint p_F \cdot n_z \, dS, \tag{2.117}$$

$$F_j^S = \rho g \pi a^2 \left(d - (h + X)\right), \tag{2.118}$$

$$F_j^D = i\omega\rho \iint \phi(r_j, \theta_j, h_j) \, dS. \tag{2.119}$$

Since the body is in equilibrium while at rest, we have that its weight must be equivalent to the weight of water displaced. Hence,

$$F_j^W = -\rho g \pi h a^2 \left(d - h\right). \tag{2.120}$$

We add up F_j^W and F_j^S to obtain the buoyancy spring force,

$$F_j^B = F_j^S + F_j^B = -\rho g \pi a_j^2 X_j. \tag{2.121}$$

This is the force that allows the body to float. It is equal to the weight of the water displaced by the body and hence, since it grows linearly with the draft has the same behavior as a spring force. This is way it is called buoyancy spring force.

To explicitly compute the dynamic component of the force, we recall the previously obtained equation representing the potential in the inner region, which reads

$$\phi_j = \frac{gH}{\omega} \left(\left(a_j^T + \sum_{i=1}^{N} \left(A_i + \hat{X}_i R_i \right)^T T_{ij} \right) \tilde{B}_j^T \tilde{\Psi}_j^D + \hat{X}_j \left(\tilde{R}_j^p + \tilde{R}_j^T \tilde{\Psi}_j^D \right) \right). \tag{2.122}$$

To have a cleaner formulation we define the following quantities:

$$\tilde{Y}_j^D = \iint \tilde{\Psi}_j^D(r_j, \theta_j, h) \, r_j \, d\theta_j \, dr_j, \tag{2.123}$$

$$\tilde{Y}_j^R = \iint \tilde{R}_j^P(r_j, h) \, r_j \, d\theta_j \, dr_j + \tilde{R}_j^T \tilde{Y}_j^D. \tag{2.124}$$

The only force contribution that we have not yet explicitly written is the one due to the power take-off, which as previously mentioned takes the form

$$F_j^G = -\delta_j X_j - \lambda_j X_j', \tag{2.125}$$

where δ_j is the stiffness coefficient of the $j-th$ body and λ_j is its corresponding damping coefficient.

Now, defining the last quantity needed for simplicity (W_j), we write the equilibrium of forces equation, from which we naturally get the equation of motion.

$$W_j = \tilde{Y}_j^R - \frac{i}{\rho g}\left(M_j\omega^2 - \pi a_j^2 \rho g + i\omega\lambda_j - \delta_j\right), \tag{2.126}$$

$$M_j X_j'' = F_j^D + F_j^B + F_j^G, \tag{2.127}$$

$$\sum_{i_1}^{N}\left(R_i^T T_{ij}\tilde{B}_j^T\tilde{Y}_j^D\right)\hat{X}_i + W_j\hat{X}_j + \sum_{i_1}^{N}\left(T_{ij}\tilde{B}_j^T\tilde{Y}_j^D\right)^T A_i = a_j^T\tilde{B}_j^T\tilde{Y}_j^D. \tag{2.128}$$

2.3.4 Derived quantities

In this section, using the previously obtained equation (2.128), we proceed to compute many relevant quantities. First, we compute the dynamic force acting on each body, detailing how to obtain the added mass and added damping to each body. Second, we obtain an expression for the power that each body is able to generate. This is of particular importance since it allows us to compute the final and most relevant parameter, the interaction factor, which is described in detail at the end of this section.

Hydrodynamic forces

Now, we describe how to compute the dynamic force acting on the bottom surface of the cylinder. We first notice that we have already developed an expression for this force in 2.119. Substituting in it the explicit expression of the potential given by 2.122, and using the previously defined expressions 2.123, 2.124 we get

$$F_j^D = i\rho g H\left(\left(a_j^T + \sum_{i=1}^{N}\left(A_i + \hat{X}_i R_i\right)^T T_{ij}\right)\tilde{B_j^T}\tilde{Y_j^D} + \hat{X}_j\tilde{Y_j}^R\right). \tag{2.129}$$

We distinguish the different contribution present inside this force:

- *Ambient force.* The first term in the bracket represents the ambient force, that is the force located at the body's position that is present either with

the body being there or not, it is due only to the ambient wave and its expression is

$$F_j^A = i\rho g H a_j^T \tilde{B_j^T} \tilde{Y_j^D}. \tag{2.130}$$

- *Incident force.* This is the contribution due to the scattered and radiated waves from the other bodies i, that are perceived as incident from our single body j. The expression of this contribution takes the form

$$F_j^I = i\rho g H \left(\sum_{i=1}^{N} \left(A_i + \hat{X}_i R_i \right)^T T_{ij} \right) \tilde{B_j^T} \tilde{Y_j^D}. \tag{2.131}$$

- *Radiated force.* This last term represents the force perceived by body j from his own radiated field. It is written as

$$F_{jj}^R = i\rho g H \hat{X}_j \tilde{Y_j}^R. \tag{2.132}$$

This component is of particular importance because it is the one we use to define the added mass and added damping to the system. The added mass m_{33} is the inertia added to the body because of the volume of water it accelerates while it is moving. Similarly, the added damping b_{33} is the amount of damping added to the body, which is commonly named radiation damping. This radiation damping is a result of the energy of the waves generated by the oscillatory motion of our body. This two terms are related to F_{jj}^R through

$$F_{jj}^R = -\left(m_{33} X_j'' + b_{33} X_j' \right). \tag{2.133}$$

Hence,

$$m_{33} = \frac{1}{\omega^2 H} Re\left\{ i\rho g H \tilde{Y_j}^R \right\}, \tag{2.134}$$

$$b_{33} = \frac{1}{\omega H} Im\left\{ i\rho g H \tilde{Y_j}^R \right\}. \tag{2.135}$$

Power

In this section, we define the power that a body is able to generate, and we develop a convenient formulation of it. The power is defined as the mean rate at which the hydrodynamic force does work over a period $T = \frac{2\pi}{\omega}$. Hence, it is written as

$$P_j = \frac{1}{T} \int_0^T Re\{F_j^D e^{-i\omega t}\} \, Re\{X_j' e^{-i\omega t}\} \, dt. \tag{2.136}$$

This expression is rewritten as follows:

$$P_j = \frac{1}{2} Re\Big\{ F_j^D \left(X_j'\right)^* \Big\}, \tag{2.137}$$

where $\left(X_j'\right)^*$ is the complex conjugate of X_j'. We now substitute the expression of F_j^D obtained from (2.127). Since the only term that brings a non-zero contribution is the damping term, we get

$$P_j = \frac{\lambda_j}{2} \left|X_j'\right|^2 = \frac{\lambda_j \omega^2 H^2 \left|X_j\right|^2}{2}. \tag{2.138}$$

Interaction factor

Now, having an expression of the power, we compute the interaction factor q, which we define as

$$q = \frac{\sum_{j=1}^{N} P_j}{NP}, \tag{2.139}$$

where N is the number of bodies in the array and P is the power extracted by a single isolated body. Being this quantity defined as the ratio between the power generated by an array composed of N bodies, and the power generated by N isolated bodies, it measures to which degree placing bodies in an array is beneficial. This quantity should always be kept into account while designing a park of buoys, since it indicates whether we are working in a good operating condition or not. For a good design, we aim to have $q \geq 1$, but in many applications, where space is the limiting factor, we just have to avoid configurations where the park effect acts too negatively, selecting the design that allows for the highest q, despite it being < 0.

For completeness, we mention the following result, obtained by Wolgamot et al. [34]:

$$\frac{1}{2\pi} \int_0^{2\pi} q(\beta)\, d\beta = 1. \tag{2.140}$$

This result shows how, in an environment where there is no preferential direction of the ambient waves, the park effect is always null. This conclusion was first achieved only under the point-absorber assumption [12], but Wolgamot extended its validity under more general hypothesis. He states that (2.140) is valid for axisymmetric devices regardless of body dimension, and that it is true not only for devices moving in heave, but also for ones moving in surge and sway, or indeed, for any combination of three or fewer modes for which the power absorbed by an isolated device is invariant with direction. This result is of key importance and we will use it in subsequent sections to validate our numerical implementation.

2.4 Numerical Modeling

In this section, we explain how to numerically implement the previously developed equation. First, we clarify some aspects concerning the number of modes to be used and the way to compute the evanescent wave numbers. Afterward, we explain how to obtain the system of equations that we use to compute the buoys' displacements, and the coefficients of the scattered wave basis, for a given sea state.

2.4.1 Number of modes

A first aspect that needs to be taken into account is that, in order not to modify a signal represented through the linear combination of an infinite amount of functions, e.g. the Fourier transform of a signal, one would have to compute an infinite amount of coefficients. This is clearly unfeasible when talking about running a simulation on a computer. Hence, in our case, the amount of θ-modes and z-modes used has to be finite. And therefore, all the quantities, whose size depends on the number of θ-modes and z-modes used, are approximations of the exact quantities due to this truncation.

The number of θ-modes and z-modes used depends on the required level of accuracy that we aim to achieve. Using $N = 5$ and $M = 40$, such that

$$0 \leq m \leq M, \tag{2.141}$$

$$-N \leq n \leq N, \tag{2.142}$$

where n and m are the numbers of the corresponding θ-mode and z-mode respectively, turns out to be enough for most applications [6].

On a side note, we specify that the following rule is used to map the quantities dependent on m or n, into their corresponding vectors:

$$\begin{aligned} m \to m+1, \qquad & m = 0, 1, ..., M, \\ n \to n+N+1, \qquad & n = -N, -N+1, ..., N-1, N. \end{aligned} \tag{2.143}$$

For vectors whose elements are associated with a pair of modes (m, n) we use the mapping rule

$$\begin{aligned} (m,n) \to (n+N)M + m + 1; \\ m = 0, 1, ..., M, \qquad n = -N, -N+1, ..., N-1, N. \end{aligned} \tag{2.144}$$

In both cases the presence of the $+1$ is needed only when working with coding languages that start counting from 1, for example, it is not needed for a Python implementation.

2.4.2 Evanescent wave-numbers

Another aspect that is worth investigating is the computation of the evanescent wave numbers. That is because, while for the progressive number the equation (2.15) can be solved analytically, for the evanescent case the equation is transcendental. Hence, to compute the values of the evanescent wave numbers we have to numerically compute the zeros of

$$f(k) = -\omega^2 - gk\tan(kd). \tag{2.145}$$

To do so, one can use any of the numerical methods for computing the zeros of a function, such as the Newton method. We must however pay attention to the choice of the initialization value used in these methods. Being the tangent a function of period π, we have to pick our initial values at distance π one from the other, as

$$k_{guess} = \left\{ \frac{\frac{\pi}{2} + \pi(q-1) + 0.1}{d} \right\}, \qquad for \quad q = 1, ..., M. \tag{2.146}$$

2.4.3 Linear system

Now, having shed a light on the main ideas to apply while implementing a code for our previously developed model, we look at how to form the linear system that will allow us to compute the buoys' displacements and the coefficients of the scattered basis.

The equations that we need to couple are (2.110) and (2.128).

Rearranging the terms in the first equation, making explicit what multiplies the unknowns A_i and X_i, we get

$$-A_j + \sum_{i=1}^{N} B_j T_{ij}^T A_i + \sum_{i=1}^{N} B_j T_{ij}^T R_i \hat{X}_i = -B_j a_j, \qquad for \quad j = 1, ..., N. \tag{2.147}$$

Doing the same for the second equation we get

$$\frac{1}{W_j}\sum_{i=1}^{N}\left(T_{ij}\tilde{B}_j^T\tilde{Y}_j^D\right)^T A_i + \frac{1}{W_j}\sum_{i=1}^{N}\left(R_i^T T_{ij}\tilde{B}_j^T\tilde{Y}_j^D\right)\hat{X}_i + \hat{X}_j = \frac{a_j^T\tilde{B}_j^T\tilde{Y}_j^D}{W_j}. \tag{2.148}$$

Our objective is now to rewrite the above equations into a single linear system in compact form, that written with a matrix-vector multiplication takes the form

$$Mz = h, \tag{2.149}$$

where z is

$$z = \left[\frac{A_i}{\hat{X}_i}\right] \tag{2.150}$$

To rewrite the system as above described, we interpret the summations in (2.147) and (2.148) as multiplications of each row of the matrix M, with the column vector z and the presence of j body is considered by having $2j$ block rows in the matrix. The 2 factor is present because we have two sets of equations where $j = 1, ..., N$.

Hence, the expressions for M is

$$M = \left[\begin{array}{c|c} M_1 & M_2 \\ \hline M_3 & M_4 \end{array}\right], \tag{2.151}$$

where,

$$M_1 = \begin{bmatrix} -I & B_1T_{21}^T & \cdots & B_1T_{N1}^T \\ B_2T_{12}^T & \ddots & & \vdots \\ \vdots & & \ddots & B_{N-1}T_{N(N-1)}^T \\ B_NT_{1N}^T & \cdots & B_NT_{(N-1)N}^T & -I \end{bmatrix}, \tag{2.152}$$

$$M_2 = \begin{bmatrix} 0 & B_1T_{21}^TR_2 & \cdots & B_1T_{N1}^TR_N \\ B_2T_{12}^TR_1 & \ddots & & \vdots \\ \vdots & & \ddots & B_{N-1}T_{N(N-1)}^TR_N \\ B_NT_{1N}^TR_N & \cdots & B_NT_{(N-1)N}^TR_{N-1} & 0 \end{bmatrix}, \tag{2.153}$$

$$M_3 = \begin{bmatrix} 0 & M_3^{21} & \cdots & M_3^{N1} \\ M_3^{12} & \ddots & & \vdots \\ \vdots & & \ddots & M_3^{N(N-1)} \\ M_3^{1N} & \dots & M_3^{(N-1),N} & 0 \end{bmatrix}, \tag{2.154}$$

$$M_4 = \begin{bmatrix} 1 & M_4^{21} & \cdots & M_4^{N1} \\ M_4^{12} & \ddots & & \vdots \\ \vdots & & \ddots & M_4^{N(N-1)} \\ M_4^{1N} & \dots & M_4^{(N-1)N} & 1 \end{bmatrix}. \tag{2.155}$$

Here, we have that:

- In M_1, the $B_i T_{ji}^T$ elements are matrices, whose size is $(2N+1)(M+1) \times (2N+1)(M+1)$, the same one of the identity matrices I.
- In M_2, the $B_i T_{ji}^T R_j$ elements are column vectors, whose size is $(2N+1)(M+1) \times 1$, the same one of the vector 0, composed of zeros.
- In M_3, the $M_3^{ij} = \frac{1}{W_j}\left[T_{ij}\tilde{B}_j^T \tilde{Y}_j^D\right]^T$ elements are row vectors, whose size is $1 \times (2N+1)(M+1)$, the same one of the vector 0, composed of zeros.
- In M_4, the $M_4^{ij} = \frac{1}{W_j} R_i^T T_{ij} \tilde{B}_j^T \tilde{Y}_j^D$ elements are scalars.

To complete the description of the numerical model we report the expression of h, that is

$$h = \begin{bmatrix} h_1 \\ \hline h_2 \end{bmatrix} = \left[\begin{array}{c} -B_1 a_1 \\ -B_2 a_2 \\ \vdots \\ -B_N a_N \\ \hline -\frac{1}{W_1} a_1^T \tilde{B}_1^T \tilde{Y}_1^D \\ -\frac{1}{W_2} a_2 T \tilde{B}_2^T \tilde{Y}_2^D \\ \vdots \\ -\frac{1}{W_N} a_N^T \tilde{B}_N^T \tilde{Y}_N^D \end{array}\right], \tag{2.156}$$

where, as previously highlighted the terms composing this vector can be divided into two groups. The first one is made of the terms $-B_j a_j$, which are the known terms of equation (2.110). The second is made of the terms $\frac{1}{W_j} a_j^T \tilde{B}_j^T \tilde{Y}_j^D$, which are the known terms of equation (2.128).

Chapter 3

Validation of the numerical model

In this chapter, we check the quality of the results given by our numerical implementation. To perform this check, we compare the results obtained by other published articles and studies, with the ones obtained by our simulations.

First, in section 3.1, we specify the hardware and software used to perform our simulations. We also give information on how to access the code.

Afterward, in section 3.2, we use as reference the results obtained in chapter 4 of Child's thesis. We perform simulations, to obtain the same quantities described in that chapter, using the same boundary conditions and parameters, as the one adopted by Child. The quantities that we investigate in this section are the frequency response of the dimensionless heave displacement, the dimensionless added mass and added damping, and finally the magnitude and phase of the ambient incident wave.

Next, in section 3.3, we use, for comparison, an article published by Göteman, titled "Methods of reducing power fluctuations in wave energy parks" [16]. Here, out of the many published results, we study the power generated by 3×3 square array configurations, ranging the spacing between the devices, using different incident wave field characteristics. Once again, we use the same parameters as Göteman, where stated, highlighting that a mismatch between the results could be found, due to the lack of statement for some parameters.

It is to be noticed that in both section 3.2, and section 3.3, we perform a convergence analysis, showing how, changing the number of θ-modes and of z-modes used, the accuracy of our solution improves. This is needed to select the appropriate amount of modes to use for running the subsequent simulations.

Lastly, in section 3.4, we use the developed and implemented model, to verify, sweeping different parameters of a selected configuration of bodies, if we obtain results coherent with what is predicted by other published studies. This is also the section where we start selecting some parameters, that are later used to set the conditions in which we perform the optimization of the array, which will be

the subject of the following chapters.

3.1 Numerical implementation's information

Here, the hardware and software, adopted for performing the code validations and, more generally, for running all the numerical implementations that provide the results shown in this thesis, are shown.

Concerning the hardware, the employed processor is an Intel Core i7-6500U CPU running at 2.5 GHz, using 12 gigabytes of RAM.

Regarding the software, the OS used is Linux, Ubuntu distribution, version 20.04. The selected programming language is Python, version 3.8.10. The choice of using Python was also made considering that Python provides a library, named SciPy, which contains all the Bessel and Hankel functions that were necessary in our numerical model.

Lastly, all the scripts, used both for the validation of the numerical model and for all the other sections of this thesis, can be found on GitHub in the following repository: `https://github.com/JacopoGallizioli/floatcyl`. For fairness, we have to mention that our numerical implementation is the continuation of Marco Gambarini's work, which can be found here: `https://github.com/marcogambarini/floatcyl`.

3.2 Child's thesis review

In this section, we first perform a convergence analysis to compute which is the sufficient number of θ-modes and z-modes to be used in our numerical implementation. Afterward, we validate our numerical implementation by studying some of the test cases present in chapter 5.4 of Child's thesis [6].

3.2.1 Convergence analysis

Here, we study the convergence of our numerical implementation, changing the number of θ-modes and z-modes used. The quantity for which we check convergence is the absolute value of the peak of the frequency response graph of the heave-scaled displacement. The convergence should be checked by measuring the absolute value of the difference between this quantity measured for different values of N and M, and its exact value. Since we are not able to analytically determine the exact value of this quantity, we choose to approximate it with the value obtained using $N = 8$ and $M = 50$. These values are chosen keeping into account both the available computational power, and the fact that the convergence values obtained by Child [6] are significantly lower.

The obtained results are shown in figure 3.1, and the parameters used are displayed in table 3.2. We can see that convergence is reached with relatively low values of N and M. Hence, given that in most of our computations we use $N = 5$ and $M = 45$, we can safely assume that the number of θ-modes and z-modes used is sufficient.

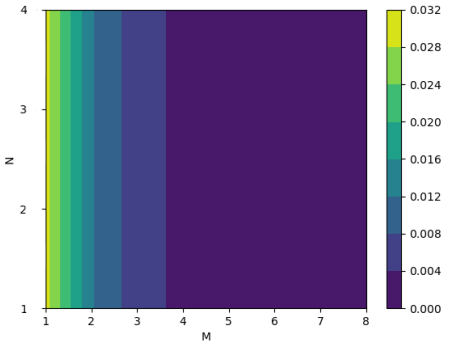

Figure 3.1: The magnitude of the error, obtained computing the non-dimensional heave displacement, is shown in relationship to the amount of θ-modes and z-modes used.

3.2.2 Results comparison

As stated before, we now proceed in the comparison between the results obtained by Child and ours. The quantities that we investigate in this section are: the heave displacement frequency response, the added mass and damping for different ambient waves, and the ambient force-frequency response.

Heave response

The first quantity that we look into is the buoy-scaled displacement. This scaled displacement is a vector rotating with the same frequency as the one of the progressive wave approaching the body. Therefore, we perform a spectral analysis of this complex quantity $\hat{X}$, by studying how its absolute value and phase change, as the progressive wavenumber associated with the incident ambient wave changes.

The comparison between our results and the ones obtained by Child is displayed in figure 3.2, and the parameters used for running these simulations are reported in table 3.1.

Looking at the graphs of figure 3.2, we see that an almost perfect agreement is found between our results and the one obtained by Child. The small mismatch, appearing both in the graph describing the amplitude behavior and the one showing the phase of $\hat{X}$, is most likely a result of the graph digitizing process.

Added mass and damping

A second quantity computed by Child, that we use to verify the validity of our code, is the added mass (2.134) together with the added damping (2.135). We compute the dimensionless counterparts of these quantities, defined as

$$\hat{m}_{33} = \frac{m_{33}}{\pi \rho a^2 d}, \tag{3.1}$$

$$\hat{b}_{33} = \frac{b_{33}}{\pi \rho a^2 d \omega}. \tag{3.2}$$

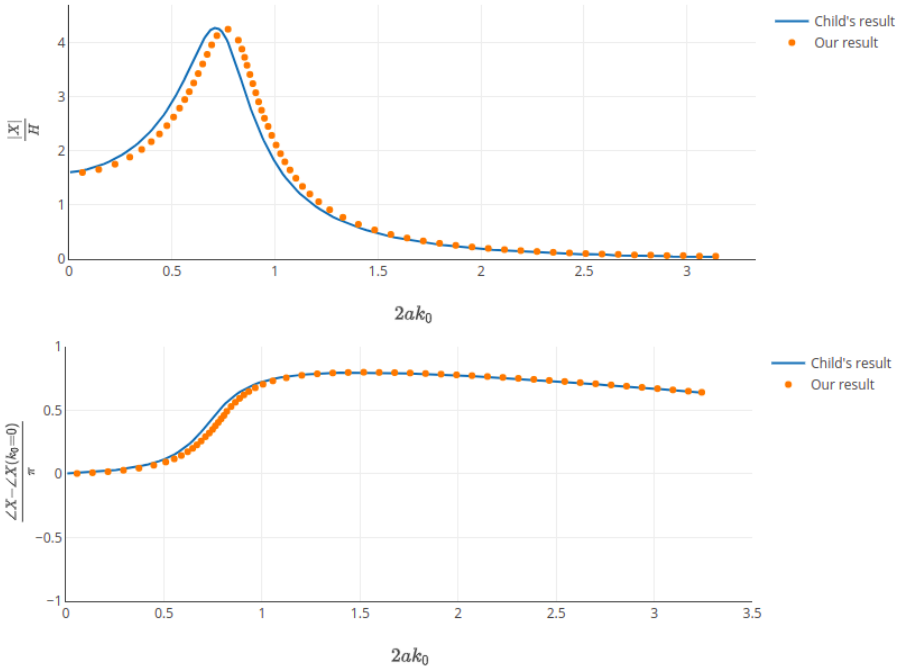

Figure 3.2: We show the non-dimensional amplitude and phase of the heave displacement of an isolated device, as a function of the non-dimensional progressive wave numbers of the incoming wave. In blue we have the results obtained by Child and in orange the ones obtained by us.

The parameters used for the computation of these two quantities are the same as before, listed in table 3.1. As shown by the graphs 3.3, there is an almost complete correspondence between the value obtained by Child and our one.

Ambient Force

An additional comparison is made with the results concerning the ambient force (2.130). We study again both the magnitude and the phase of the rotating vector representing the ambient force in the location of our device. Note that, the ambient force values are independent from the parameters chosen to describe the body, since this force is present even when our body is not. Also in this case the quantity we investigate are non-dimensional, that is to convey more general information. These quantities are defined as

$$|\hat{F}_A| = \frac{|F_A|}{\rho g \pi a^2 H}, \tag{3.3}$$

$$\angle F_{A\,scaled} = \frac{\angle F_A - \angle F_A(\omega = 0)}{\pi}. \tag{3.4}$$

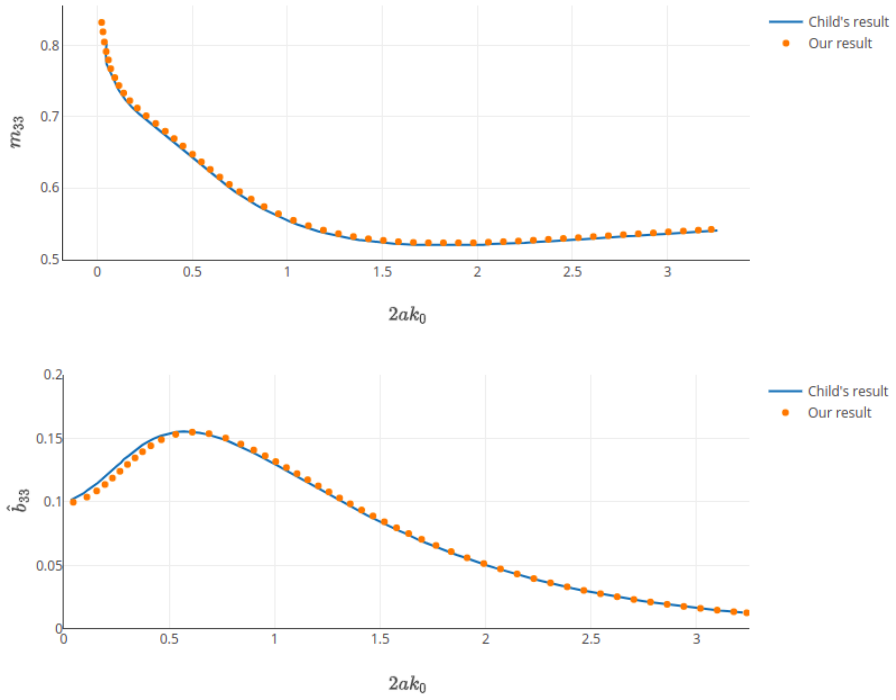

Figure 3.3: We show the non-dimensional added mass and added damping as a function of the frequency of the ambient wave approaching the body. In blue, we have the result obtained by Child and in orange the one obtained by us.

Also in this case, as shown in figure 3.4, there is a good matching between the results obtained by us and Child. Overall, the comparison between our results and the one obtained by Child points toward the fact that our implementation is correct.

3.3 Göteman's article review

In this section, we simulate, using our numerical implementation, the results published in an article by Göteman [16]. Our objective is, once again, to obtain results that can validate our implementation.

We use the same approach previously adopted when using Child's thesis as a reference, that is first performing a convergence analysis, and afterward computing the actual quantities present in the article.

3.3.1 Convergence analysis

Here, we study the convergence of our numerical implementation ranging the number of θ-modes and z-modes used. The quantity, for which we check conver-

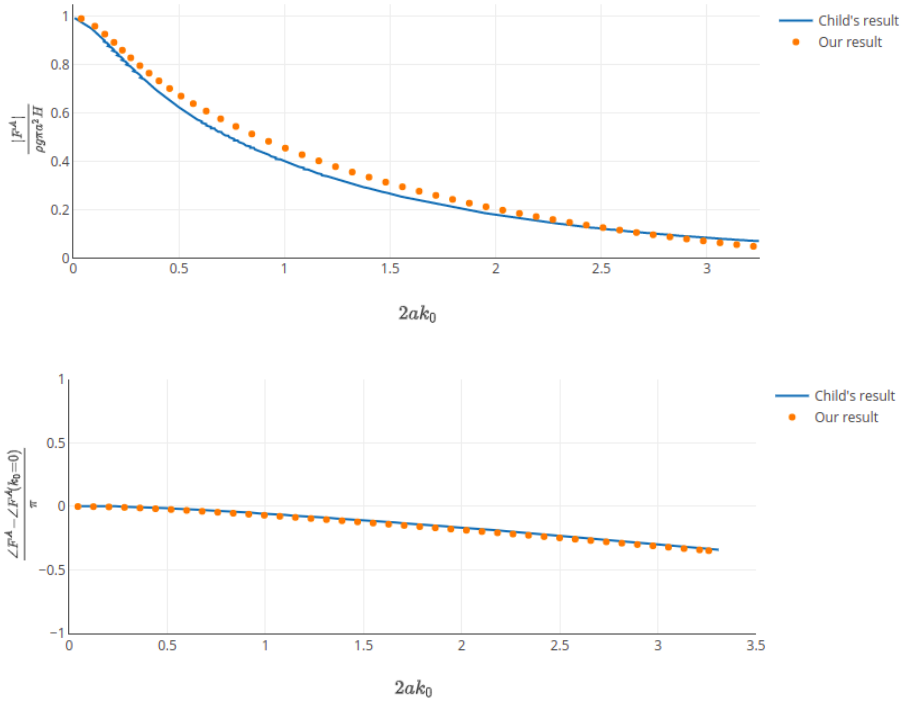

Figure 3.4: We show the non-dimensional amplitude and phase of the ambient force as a function of its frequency. In blue we have the result obtained by Child and in orange the one obtained by us.

gence, is the average power produced by a 3×3 square configuration of bodies, whose parameters are detailed in table 3.3.

The obtained results are displayed in figure 3.5. We can see that convergence is reached relatively early. Hence, the choice of $N = 5$ and $M = 45$, which we adopt throughout the simulations of this section, is good in terms of convergence.

3.3.2 Power of 3×3 configuration

Here, we choose to check the values obtained by Göteman in section IV.B. In that section, they compute the total power generated by a 3×3 square configuration of energy converter, for different sea states and for different values of spacing between the devices.

The comparison between our results and the one obtained by Göteman is displayed in figure 3.6. The parameters used to run our simulations and the one used by Göteman are displayed in table 3.4.

By looking at the obtained results, we notice that the graph showcase an expected behavior, which is the fact that our estimations of the values of the powers are around double the ones obtained by Göteman. This is due to the

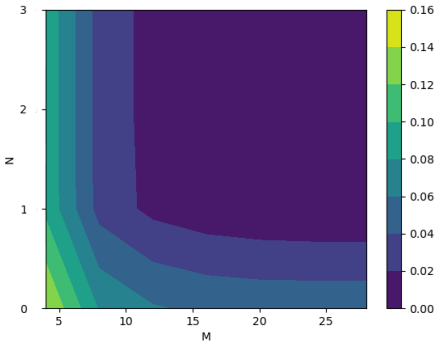

Figure 3.5: The magnitude of the error, obtained computing the average power produced by a 3×3 square configuration, is shown in relationship to the amount of θ-modes and z-modes used. The parameters used are shown in table 3.3

fact that Göteman uses a wave climate, which is the superposition of waves with different periods. The H_s parameter he refers to in the article, simply reported as H in table 3.4, is the significant wave height, which is computed as the average height of the highest one-third of all waves measured [19]. On the other hand, we use a monochromatic wave with the same energy period and wave height.

When referring to the relation

$$H_s \sim 4\eta_{rms}, \tag{3.5}$$

Yoshimi states that this proportionality between the significant wave height and the RMS surface elevation is confirmed by many wave observation data taken throughout the world [15]. Hence, given that, for a monochromatic wave of height H_m, η_{rms} can be computed as

$$\eta(t) = \frac{H_m}{2}\cos(\omega t), \tag{3.6}$$

$$\eta^2(t) = \frac{H_m^2}{4}\cos^2(\omega t), \tag{3.7}$$

$$\overline{\eta^2(t)} = \frac{H_m}{8}, \tag{3.8}$$

$$\eta_{rms} = \frac{H_m}{2\sqrt{2}}. \tag{3.9}$$

We get that the relation between H_s and H_m is

$$H_m \sim \frac{H_s}{\sqrt{2}}. \tag{3.10}$$

Therefore, since the power scales with the square of the wave height, we get that the power, obtained using a monochromatic wave with same wave height

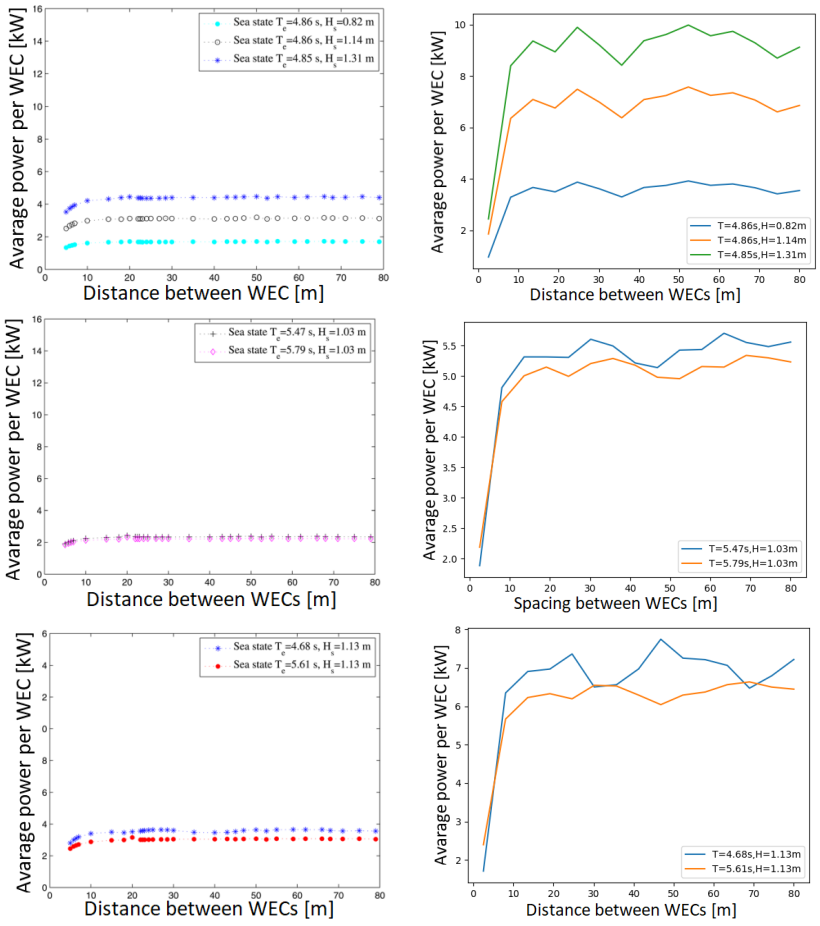

Figure 3.6: The value of the average power per energy converter [kW] is shown in relationship to the variation of spacing between devices. The graphs on the left are the ones obtained by Göteman calculations, while the ones on the right are the ones obtained with our calculations. In each pair of graphs, different sea states with similar wave heights H but different periods are compared.

as the significant wave height of a wave climate, is doubled with respect to the one of the original wave climate.

Analyzing the general behavior of the graphs we obtained, we notice that, in accordance with Göteman's results, for a very low buoy separation distance, the park effect acts destructively, reducing the average extracted power by a significant amount. At the same time, it is interesting to notice that, after a certain spacing threshold value of around 10 m, a further increase of spacing does not improve consistently the value of extracted power. Also, it is worth highlighting that the average powers per energy converter oscillate around the same value both for ours and Göteman's simulations, but the shapes of these oscillations are different. This is most likely due to the use of different parameters, such as the value of the sea depth, in case they were not defined by Göteman, or to the different modeling methodology applied. This also implies that it is very difficult to exploit the positive aspects of the park effect, if one acts only by modifying the spacing between the devices. Therefore, the spacing constraint should be considered mainly to avoid operating in the condition of spacing ≤ 10 m, for which we see that the park effect brings a large negative effect.

Concluding, we see that, despite having a slightly different shape, both our and Göteman's results showcase the same trend. This suggests a correct numerical implementation.

3.3.3 Power variance of 3 $\times$ 3 configuration

Here, we replicate another result obtained by Göteman in section IV.B. This time we want to verify if our numerical model is able to accurately predict how the power variance changes, as a function of the spacing between the devices, for the same 3 $\times$ 3 square configuration, described again by the parameters of table 3.4. Here we don't simulate the results for all the sea states previously analyzed, but only for the one corresponding to wave height $H = 0.82$ m and energy period $T = 4.86$ s. This choice is arbitrary and it is made only because this is the first sea state appearing in Göteman's article.

The results obtained are displayed in figure 3.7. We can immediately notice that, once again, using a monochromatic wave instead of a wave climate leads to different results. We can nonetheless make some considerations, regarding the obtained results, that can make us understand whether our numerical implementation is correct or not.

One is to be made concerning the seemingly periodic nature of our result. This characteristic is also naturally linked to the nature of the monochromatic wave. That is because, having our incident wave a wavelength $\lambda = 36.8$ m, and being the number of arrays odd along each dimension, we have that, for spacings that are multiples of $\frac{\lambda}{2}$, two devices oscillate with the same phase. This clearly leads to a peak in the variance. On the other hand, if the spacing is a multiple of $\frac{\lambda}{3}$, but not of $\frac{\lambda}{2}$, we have that the interaction between the bodies and the wave is such that the ascendant and descendant movements compensate each other, leading to an almost null variance. This fact can be better understood

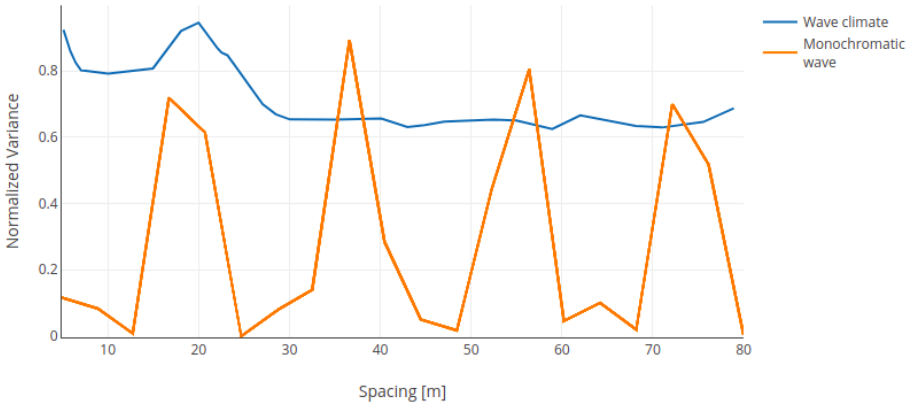

Figure 3.7: The value of the total power variance, normalized with the square of the average total power, is shown in relationship to the variation of spacing between devices. The blue line shows the results obtained by Göteman, who used a wave climate of significant wave height $H_s = 0.82\ m$. The orange line represents the results obtained by us, using a monochromatic wave of wave height $H = 0.82\ m$.

by visualizing $\frac{2}{3}$ of a period of a sine function. Splitting the support of this function in three equal intervals, and evaluating the function on the nodes of this partition, we obtain the z positions of a line of bodies when the ambient wave has a wavelength equal to 3 times the spacing between the bodies. In this configuration we get that the z-position of the first body is equal to zero, meanwhile, the z-position of the second and the third bodies are equal but opposite in sign. These positions highlight the above-mentioned property of the ascending and descending movements compensating each other.

Concluding, we can say that, despite our results not matching with the ones of Göteman, this difference is due to the different way used to model the incident wavefield. Moreover, our results are consistent with the hypothesis of monochromatic incident wave, suggesting a correct numerical implementation.

3.4 Configurations testing

Having checked the validity of our implementation, we now study the properties of different arrangements of bodies, using the interaction factor, 2.139, as the main parameter for measuring the performances of a given configuration. This analysis is executed to perform an additional control on the consistency of our results. The results have to be coherent with the theoretical knowledge we developed studying the subject, and with results published in other related works.

The first configuration we study is one with the devices displayed along

a simple line. This case-study is useful to observe many general results that we are going to exploit afterward. The second one consists in positioning the devices along a semi-ellipses that share the line along which one of the two axes is positioned.

The last configuration is one with 9 bodies displayed in a 3×3 square configuration. Unlike before, this configuration is not explored to find greater evidence of the exactness of our numerical implementation. We choose to carry out the analysis of this configuration for the purpose of determining which is the domain we should select for the optimization that will be carried on in section 5. This domain determines the area inside which our bodies are constrained, and therefore highly affects the results of our optimization.

For all the results that are displayed, we specify the value of the parameters used to obtain them for reproducibility.

3.4.1 Line

The first configuration that we want to try, is one where all the devices are positioned along a straight line. Figure 3.8 helps us to visualize how the devices are positioned in space.

β vs spacing

Now, we compute how the interaction factor changes, ranging simultaneously the value of the incident angle β, and of the *spacing* between the devices. We display the results in figure 3.9. These results are obtained using the values of the parameters reported in table 3.5.

The first thing that we can notice analyzing our results, is that the interaction factor is never greater than 1.02. This means that, with this configuration, we cannot achieve an improvement of performance larger than 2%, with respect to the case where all the devices are isolated. We can anticipate that, for most configurations in this section, it will be impossible to obtain an interaction factor capable of improving performances substantially. The second consideration that we make, is that, for certain combinations of β and *spacing*, the interaction factor is smaller than 1, getting close to the value of 0.9. Hence, during the design phase of a park of buoys, one should consider these results, to avoid working in operating conditions associated with an interaction factor smaller than 1.

Another consideration that can be made, is that the value of β for which we can obtain the best interaction factor values, at relatively low spacing, is $\beta = 0$, this result had been already found [23], and here it is confirmed.

Average q

Now, we want to analyze how the park operates in an environment where there is no preferential direction of the incoming wave. To do so, one simply has to compute the average interaction factor over the different values of β, obtained

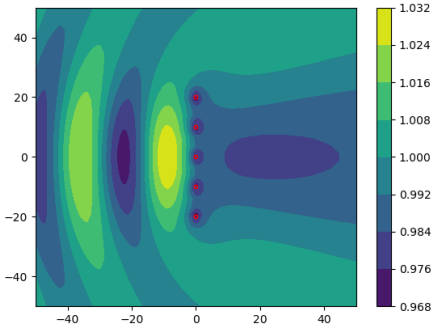

Figure 3.8: Magnitude of the free-surface displacement generated by an ambient wave of amplitude $H = 1\ m$, frequency $\omega = 1\ \frac{rad}{s}$, traveling in the x-direction, interacting with an array of 5 buoys, of radius $a = 1\ m$, draft $d - h = 0.5\ m$, spaced with a distance of $5m$ along the y-axis, in a sea of depth $d = 10\ m$ and water density $\rho = 1000\ \frac{kg}{m^3}$.

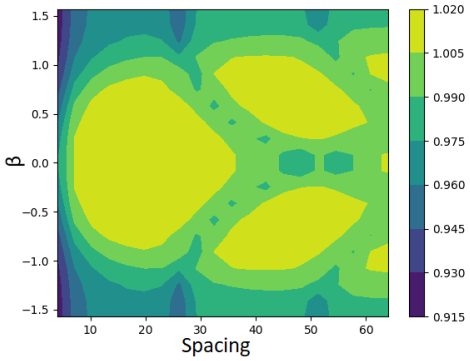

Figure 3.9: Interaction factor as a function of β and the spacing between the devices. The parameters used are the one of table 3.5.

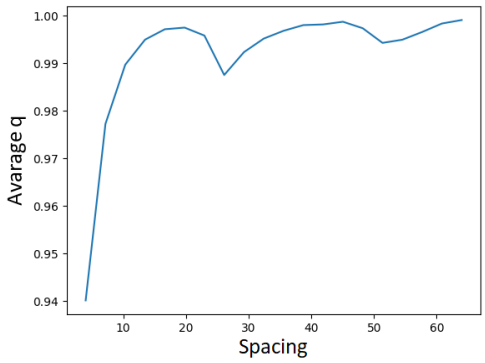

Figure 3.10: Interaction factor averaged over the different value of β, as a function of the spacing between the devices. The parameters used are the one of table 3.5.

for each value of spacing. The results of this computation are shown in figure 3.10.

Looking at this graph, one can see that the interaction factor is always smaller than $q = 1$, and converges to 1 increasing the value of the spacing parameter. This is perfectly consistent, given that, for high value of spacing, we achieve a configuration where the devices can almost be considered isolated, being very far from each other. In addition, we can see that the value of the interaction factor, despite being always smaller than $q = 1$, is also very close to 1, for all configurations with a high enough spacing. This is consistent with (2.140), showcasing a good numerical implementation.

A second consideration concerns the value of the optimal spacing. That is, the smallest possible value of spacing, which allows for a good average interaction factor. We can see from image 3.10 that this value is around $16m$.

3.4.2 Semi-ellipses

Here, we compute the interaction factor and the variance for an array of bodies positioned on two semi-elliptical lines. The variance is considered normalized with the square of the average buoy power. Figure 3.11, is useful to understand how the bodies are positioned in space.

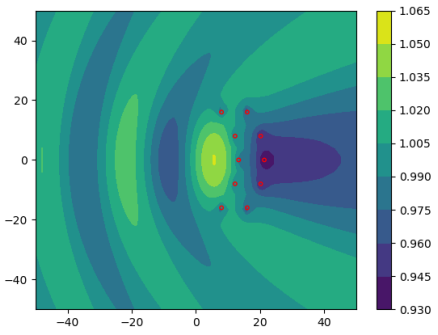

Figure 3.11: Magnitude of the free-surface displacement generated by an ambient wave with $H = 1\ m$, $\omega = 1\ \frac{rad}{s}$, travelling in the x-direction, interacting with an array of 10 buoy, with $a = 1\ m$, $d - h = 0.5\ m$, placed along 2 semi-ellipses, spaced with a distance of $8m$ along the y-axis, in a sea with $d = 10\ m$ and water density $\rho = 1000\ \frac{kg}{m^3}$.

Before proceeding, we need to define the aspect ratio of an ellipse. Considering a semi-ellipse, symmetric with respect to the x-axis, whose semi-axes a and b are aligned with the x and y-axis respectively, we define the aspect ratio magnitude as

$$|AR| = \frac{a}{b}, \tag{3.11}$$

The sign of AR is taken positive if the semi-ellipse is in the first and second quadrant, negative otherwise. This definition is necessary because we compute how the power variance and the interaction factor changes in function of the selected aspect ratio.

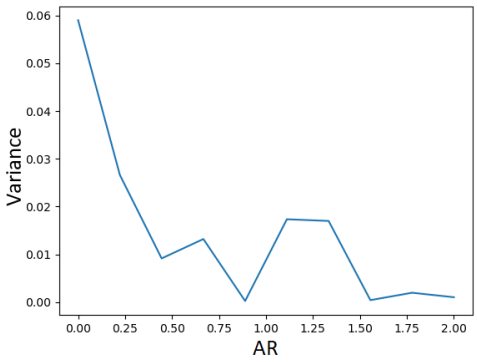

Figure 3.12: Power variance as a function of AR for a configuration of bodies displaced along two semi-elliptical lines. The parameter used are the one of table 3.6.

Variance

Here, we study how the power variance changes as a function of $|AR|$.

We report the values of the parameters used for this simulation in table 3.6. Since we are keeping β constant, we have to choose to which value we want to set it. We choose to set it to the value for which we had optimal performance for the straight line configuration, that is $\beta = 0$. The same rule is applied when choosing to which value set the *spacing* parameter, that is $spacing = 16\ m$. We also specify that for *spacing* we mean the distance between the projection along the y-axis of the centers of two consecutive bodies.

The results obtained from this simulation are displayed in Figure 3.12. Analyzing this image, we see that the variance decreases changing from a straight line configuration to a semi-elliptical one. That is to be expected, given that we are forcing our system with a monochromatic wave, that, when the bodies are placed along a straight line, is perpendicular to the said line, making all the bodies oscillate with the same phase. Meanwhile, increasing $|AR|$, the bodies oscillate with different phases, which corresponds to lower variance. Once again, our numerical implementation shows to be consistent.

Average interaction factor

Here, we first compute how the interaction factor varies for different values of AR and β, to later compute how it is averaged over different values of β.

The values of the parameters used while running this simulation are shown in table 3.7. Same as before, for the value of the *spacing* we chose the one that granted us the best interaction factor in the straight line configuration, that is $spacing = 16\ m$.

The results we obtain are displayed in figure 3.13. We can see that, once again, the best set of values for the interaction factor is found for $\beta = 0$.

We now study which aspect ratio corresponds to the best interaction factor averaged on the different values of β. This is useful because it allows us to consider the operating environment in which there is no preferential direction of the ambient waves.

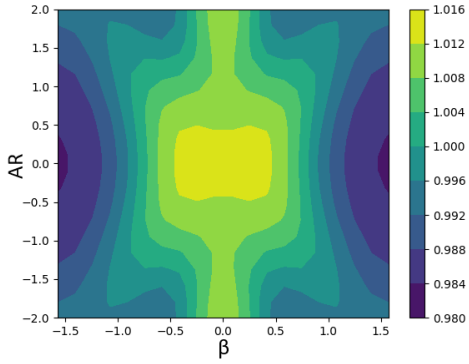

Figure 3.13: Interaction factor as a function of AR and β, for a semi-elliptical configuration. The parameters used are the one of table 3.7.

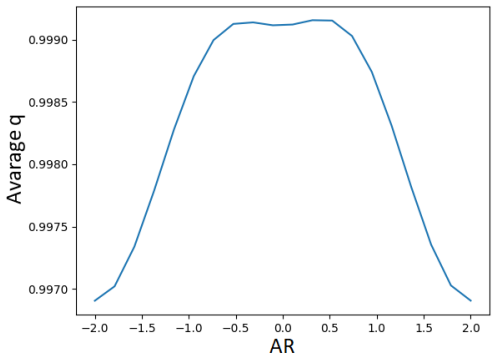

Figure 3.14: Interaction factor averaged over different values of β as a function of AR. The parameters used are the one of table 3.7.

The results of this analysis are displayed in image 3.14. Looking at figure 3.14, we see that there is no AR value for which the average interaction factor is greater than unity, if there is no preferential direction of the ambient wave. Moreover, the average interaction factor is extremely close to unity for every value of AR. This is a known result [34], confirmed by our numerical implementation. This also shows consistency with (2.140), since (2.140) is obtained in optimal conditions, and here we are in sub-optimal operating conditions.

Considering then, which configuration has the greatest average interaction factor, we get that the configurations with $|AR|$ around 0.7, is the one that gives the best average q. Previous studies already showed that, changing the curvature of the line along which the energy converters are positioned, has the benefit of creating a configuration less dependent on the ambient waves directions [9]. Here, we can see that our model confirms these results to be true.

3.4.3 3×3 square

Here, we aim at defining the size of the domain, inside which we wish to constrain the bodies composing the array that we wish to optimize. In the optimization that we perform, whose model is detailed in section 4, nine bodies are located in a fixed area, and we compute the configuration for which the produced power is maximized. This kind of optimization, where the bodies are constrained into a prescribed domain, tends to face the real-life problem of having a limited amount of space for the installation of a park of energy converter. Given that, we now run a simulation that computes how the interaction factor changes, for a 3×3 square configuration, ranging the spacing between the bodies and the staggering between the first and second line.

We define the staggering between two consecutive lines as the relative y-displacement of one line with respect to the other. Actually, we consider the non-dimensional staggering, scaling it with the spacing parameter. Here, only the second line is considered to be staggered, meanwhile, the first and third ones maintain the original position. Figure 3.15, is useful to understand how the bodies are positioned in space.

Now, we run the simulation using the parameters of table 3.8, whose results are displayed in image 3.16. From our results, we notice that changing the staggering parameter has a minimal influence on the interaction factor. Meanwhile, there is a strong dependence on the interaction factor from the value of the spacing between bodies. We remind that we are looking for a domain, whose purpose is to contain an array of wave energy converters, that allows for a good interaction factor, minimizing at the same time the required space. Therefore, we select a square domain, whose area is equal to $400m^2$, that is because, as we have just shown, it allows for configurations with an interaction factor close to unity.

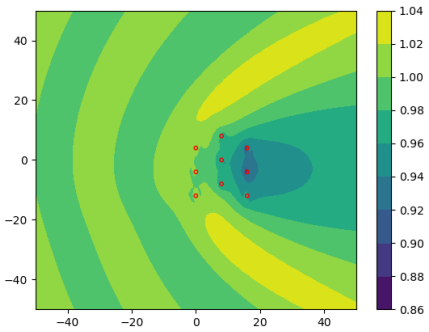

Figure 3.15: Magnitude of the free-surface displacement generated by an ambient wave with $H = 1\ m$, $\omega = 1\ \frac{rad}{s}$, traveling in the x-direction, interacting with an array of 9 buoys, with $a = 1\ m$, $d - h = 0.5\ m$, placed in a 3×3 square with staggering of 0.5 , with a distance of 8 m along the y-axis, in a sea with $d = 10m$ and water density $\rho = 1000\ \frac{kg}{m^3}$.

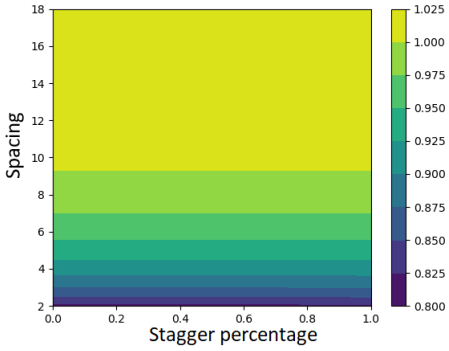

Figure 3.16: Interaction factor as a function of *spacing* and *staggering*, for a 3×3 square configuration. The parameter used for this simulation are displayed in table 3.8.

Parameters comparison		
Parameter	Child's values	Our values
a	a_T m	1 m
draft	$b_T = a_T$ m	1 m
lambda	λ_{ds} $\frac{Ns}{m}$	λ_{ds} $\frac{Ns}{m}$
delta	δ_{ds} $\frac{N}{m}$	δ_{ds} $\frac{N}{m}$
depth	$d_T = 8a_T$ m	8 m
k_0	$\frac{1}{a}[0\ 4]$ $\frac{1}{m}$	$[0\ 4]$ $\frac{1}{m}$
Nn	0	0
Nq	33	33
rho	1000	1000 $\frac{kg}{m^3}$

Table 3.1: Child's parameters compared to the one used in our simulations, a "?" is present when the parameter used by Child was not specified. δ_{ds} and λ_ds are the damping and spring constants obtained with reactive (damping-spring) tuning respectively. They take the following form: $\delta_{ds} = \omega_0^2 \left(M + m_{33}(\omega_0)\right) - \rho g \pi a^2$, $\lambda_{ds} = b_{33}(\omega_0)$.

Parameter	Value	Parameter	Value	Parameter	Value
a	$1m$	$d-h$	$1m$	λ	$55000\frac{Ns}{m}$
d	$8m$	ω	$1.978rads$	δ	$4000\frac{N}{m}$
β	$0rad$	N_N	4	N_M	8
ρ	$1000\frac{kg}{m^3}$	N	$[1,4]$	M	$[1,8]$

Table 3.2: Parameters used for convergence analysis of the peak of the heave scaled displacement frequency response graph of an isolated body. N represents the number of θ-modes used, M the number of z-modes.

Parameter	Value	Parameter	Value	Parameter	Value
a	$2m$	$d-h$	$0.5m$	λ	$55000\frac{Ns}{m}$
δ	$4000\frac{N}{m}$	N_{bodies}	9	$spacing$	$16m$
d	$20m$	ω	$\frac{2\pi}{4.86}\frac{rad}{s}$	H	$0.86m$
β	$0rad$	N_N	4	N_M	7
ρ	$1000\frac{kg}{m^3}$	N	$[0,3]$	M	$[4,28]$

Table 3.3: Parameters used for convergence analysis of Göteman 3×3 square configuration. N represents the number of θ-modes used, M the number of z-modes.

Parameters comparison		
Parameter	Göteman's values	My values
a	2 m	2 m
draft	0.5 m	0.5 m
lambda	55000 $\frac{Ns}{m}$	55000 $\frac{Ns}{m}$
delta	4000 $\frac{N}{m}$	4000 $\frac{N}{m}$
Nbodies	9	9
configuration	square	square
spacing	[4 80] m	[3 80] m
depth	?	20 m
omega	[1.29, 1.29, 1.30, 1.15, 1.09, 1.34, 1.12, 1.01, 0.86] $\frac{rad}{s}$	[1.29, 1.29, 1.30, 1.15, 1.09, 1.34, 1.12, 1.01, 0.86] $\frac{rad}{s}$
H	[1.53, 0.82, 1.14, 1.31, 1.03, 1.03, 1.13, 1.13, 2.37, 2.36] m	[1.53, 0.82, 1.14, 1.31, 1.03, 1.03, 1.13, 1.13, 2.37, 2.36] m
beta	0 rad	0 rad
Nn	?	5
Nq	?	45
rho	?	1000 $\frac{kg}{m^3}$

Table 3.4: Göteman parameters compared to the one used in our simulations, a "?" is present when the parameter used by Göteman was not specified.

Parameter	Value	Parameter	Value	Parameter	Value
a	$1m$	$d-h$	$0.5m$	λ	$50000\frac{Ns}{m}$
δ	$4000\frac{N}{m}$	N_{bodies}	9	$spacing$	$[8,24]\,m$
d	$10m$	ω	$1\frac{rad}{s}$	H	$1m$
β	$\left[-\frac{\pi}{2},\frac{\pi}{2}\right]\,rad$	N_n	5	N_q	45
ρ	$1000\frac{kg}{m^3}$	N_β	20	$N_{spacing}$	20

Table 3.5: Parameters used for the computation of the interaction factor for the straight line configuration. N_n represents the number of θ-modes used, N_q the number of z-modes, N_{beta} the number of nodes on the β-axis, $N_{spacing}$ the number of nodes on the *spacing*-axis.

Parameter	Value	Parameter	Value
a	$1m$	$d-h$	$0.5m$
λ	$50000\frac{Ns}{m}$	$spacing$	$16m$
δ	$4000\frac{N}{m}$	N_{bodies}	20
d	$10m$	ω	$1\frac{rad}{s}$
H	$1m$	N_q	45
β	$0rad$	N_n	5
ρ	$1000\frac{kg}{m^3}$	N_{Lines}	2
N_{AR}	10	AR	$[0,2]$

Table 3.6: Parameters used for the computation of the power variance, for a configuration of 2 elliptical lines, varying AR.

Parameter	Value	Parameter	Value
a	$1m$	$d-h$	$0.5m$
λ	$50000\frac{Ns}{m}$	$spacing$	$16m$
δ	$4000\frac{N}{m}$	N_{bodies}	5
d	$10m$	ω	$1\frac{rad}{s}$
H	$1m$	N_q	45
β	$\left[-\frac{\pi}{2}, \frac{\pi}{2}\right] rad$	N_n	5
ρ	$1000\frac{kg}{m^3}$	N_β	20
N_{AR}	20	AR	$[-1, 1]$

Table 3.7: Parameters used for the computation of the interaction factor for the elliptical configuration, varying AR and β.

Parameter	Value	Parameter	Value
a	$1m$	$d-h$	$0.5m$
λ	$50000\frac{Ns}{m}$	$spacing$	$[2, 18]\, m$
δ	$4000\frac{N}{m}$	N_{bodies}	9
d	$10m$	ω	$1\frac{rad}{s}$
H	$1m$	N_q	45
β	$0rad$	N_n	5
ρ	$1000\frac{kg}{m^3}$	$N_{spacing}$	4
$N_{staggering}$	4	$staggering$	$[0, 1]$

Table 3.8: Parameters used for the computation of the interaction factor for the 3×3 square configuration, varying $spacing$ and $staggering$.

Chapter 4

WEC arrays optimization

In this chapter, we explain how to develop the model to optimize the power produced by our array. The results obtained through the numerical implementation of this model are later described in chapter 5.

We first describe, in section 4.1, how the power is optimized by modifying the positions of the bodies. Later, in section 4.2, we see how further improvement can be done by optimizing the damping coefficient of each device.

For both the optimization of the positions and of the damping coefficients, we first describe how to compute the gradient of the cost function, that is the total power with negative sign. Subsequently, we detail how to implement numerically the appropriate gradient method for the computation of the optimal solution. Finally, we check that the computed and numerically simulated gradients are correct, by performing a convergence analysis.

4.1 Position optimization

In this section, we describe how to obtain the model to retrieve the optimal configuration for an array of bodies, under the constraint of them being located in a fixed selected area. In the first part, we formulate our optimization problem. Later, we describe how to compute the gradient of our cost function. There, we also check that the computed gradient is correct by performing a convergence test with a finite difference approach. Finally, in the last part of this section, we focus on how to use the computed gradient to implement the projected gradient method.

4.1.1 Formulation of the optimization problem

Here, we describe how our optimization problem is formulated. The quantity that we aim to maximize is the total power produced by the selected array of devices. Therefore, since it is custom to formulate minimization problems, we define our cost function as the total power with inverted sign, that is

$$J = -\frac{1}{2}\omega^2 \sum_{i=1}^{N_b} \lambda_i |\hat{z}_i|^2, \tag{4.1}$$

where λ_i is the damping coefficient of the $i-th$ body, $\hat{z}_i$ its dimensionless heave displacement, obtained solving 2.149, and N_b is the number of bodies composing the array. This quantity can be defined in a more compact way as

$$J = -\frac{1}{2}\omega^2 z^H \Lambda z, \tag{4.2}$$

where z is a vector of size $N_b \times 1$, containing the heave displacements of all bodies, the H operator applied to it is the Hermitian transpose, and Λ is a matrix defined as

$$\Lambda = \begin{bmatrix} \lambda_1 & 0 & \cdots & \cdots & 0 \\ 0 & \lambda_2 & 0 & \cdots & 0 \\ \vdots & 0 & \ddots & & \vdots \\ \vdots & \vdots & & \ddots & 0 \\ 0 & 0 & \dots & 0 & \lambda_{N_b} \end{bmatrix}. \tag{4.3}$$

Notice that Λ is diagonal (Hermitian) and positive definite.

In addition, we have to specify that our optimization problem is constrained in the variable x. This means that before performing the optimization we have to define an admissible set inside which we want our variable x to be constrained. This is done to perform an analysis of the optimal configuration under the constraint of the bodies being located inside a given area. The method through which this constraint is applied is later defined when discussing the optimization algorithm.

4.1.2 Derivation of the gradient of the objective function

Having defined the cost function to be minimized, we now proceed to compute the gradient of this cost function, so that later a projected gradient method could be applied to find the optimal solution. In order to derive the gradient of the objective function, the first step consists in forming the Lagrangian function $\mathcal{L}$,

$$\mathcal{L}(A, z; \mu, \nu; x, y) = -\frac{1}{2}\omega^2 z^H \Lambda z + Re\left[\mu^H \left(M_1 A + M_2 z - h_1\right)\right] + \\ + Re\left[\nu^H \left(M_3 A + M_4 z - h_2\right)\right]. \tag{4.4}$$

Here, μ and ν are the Lagrange multipliers vectors, and A is the vector of coefficients of the scatter wave basis obtained solving the state equation (2.149).

Now, differentiating $\mathcal{L}$ with respect to μ and ν, we obtain once again the state equation (2.149). Meanwhile, differentiating it with respect to A and z, we obtain the additional equations necessary to compute the Lagrange multiplier. Starting differentiating with respect to A, we get

$$\frac{d\mathcal{L}}{dA}\delta A = 0, \qquad \forall \delta A, \tag{4.5}$$

$$\Leftrightarrow \quad Re\left[\mu^H M_1 \delta A + \nu^H M_3 \delta A\right] = 0, \qquad \forall \delta A, \tag{4.6}$$

$$\Leftrightarrow \quad Re\left[\delta A^H \left(M_1^H \mu + M_3^H \nu\right)\right] = 0, \qquad \forall \delta A, \tag{4.7}$$

$$\Leftrightarrow \quad M_1^H \mu + M_3^H \nu = 0. \tag{4.8}$$

Meanwhile differentiating with respect to z, we have

$$\frac{d\mathcal{L}}{dz}\delta z = 0, \qquad \forall \delta z, \tag{4.9}$$

$$\Leftrightarrow \quad -\frac{1}{2}\omega^2 \delta z^H \Lambda z - \frac{1}{2}\omega^2 z^h \Lambda \delta z + Re\left[\mu^H M_2 \delta z + \nu^H M_4 \delta z\right], \qquad \forall \delta z = 0, \tag{4.10}$$

$$\Leftrightarrow \quad -\omega^2 Re\left[\delta z^H \Lambda z\right] + Re\left[\delta z^H \left(M_2^H \mu + M_4^H \nu\right)\right], \qquad \forall \delta z = 0, \tag{4.11}$$

$$\Leftrightarrow \quad Re\left[\delta z^H \left(-\omega^2 \Lambda z + M_2^H \mu + M_4^H \nu\right)\right], \qquad \forall \delta z = 0, \tag{4.12}$$

$$\Leftrightarrow \quad -\omega^2 \Lambda z + M_2^H \mu + M_4^H \nu = 0. \tag{4.13}$$

Writing the linear system of the coupled equations (4.8) and (4.13) in compact form we get

$$\begin{bmatrix} M_1^H & M_3^H \\ M_2^H & M_4^H \end{bmatrix} \begin{bmatrix} \mu \\ \nu \end{bmatrix} = \begin{bmatrix} 0 \\ \omega^2 \Lambda z \end{bmatrix}. \tag{4.14}$$

This is the linear system that can be numerically solved to compute the values of the Lagrange multipliers.

Now, having shown how to compute the Lagrange multipliers in vectors μ and ν, we proceed to compute the gradient of J. To do so, one must compute the derivatives of the Lagrange function $\mathcal{L}$ with respect to x and y. And then assemble this derivatives vector into the vector ∇J. Computing the derivatives with respect to the $i-th$ body x-coordinate, x_i, we get

$$\frac{\partial \mathcal{L}}{\partial x_i} = Re\left[\mu^H \left(\frac{\partial M_1}{\partial x_i} + \frac{\partial M_2}{\partial x_i} z\right) + \nu^H \left(\frac{\partial M_3}{\partial x_i} A \frac{\partial M_4}{\partial x_i} z\right)\right], \tag{4.15}$$

where

$$\frac{\partial M_1}{\partial x_i} = \begin{bmatrix} 0 & \cdots & 0 & B_i \frac{\partial T_{1,i}}{\partial x_i} & 0 & \cdots & 0 \\ \vdots & & \vdots & \vdots & \vdots & & \vdots \\ 0 & \cdots & 0 & B_i \frac{\partial T_{i-1,i}}{\partial x_i} & 0 & \cdots & 0 \\ B_1 \frac{\partial T_{i,1}}{\partial x_i} \cdots & B_{i-1} \frac{\partial T_{i,i-1}}{\partial x_i} & 0 & B_{i+1} \frac{\partial T_{i,i+1}}{\partial x_i} \cdots & B_{N_b} \frac{\partial T_{i,N_b}}{\partial x_i} & & \\ 0 & \cdots & 0 & B_i \frac{\partial T_{i+1,i}}{\partial x_i} & 0 & \cdots & 0 \\ \vdots & & \vdots & \vdots & \vdots & & \vdots \\ 0 & \cdots & 0 & B_i \frac{\partial T_{N_B,i}}{\partial x_i} & 0 & \cdots & 0 \end{bmatrix}, \quad (4.16)$$

$$\frac{\partial M_2}{\partial x_i} = \begin{bmatrix} 0 & \cdots & 0 & \frac{\partial M_2^{1,i}}{\partial x_i} & 0 & \cdots & 0 \\ \vdots & & \vdots & \vdots & \vdots & & \vdots \\ 0 & \cdots & 0 & \frac{\partial M_2^{i-1,i}}{\partial x_i} & 0 & \cdots & 0 \\ \frac{\partial M_2^{i,1}}{\partial x_i} & \cdots & \frac{\partial M_2^{i,i-1}}{\partial x_i} & 0 & \frac{\partial M_2^{i,i+1}}{\partial x_i} & \cdots & \frac{\partial M_2^{i,N_b}}{\partial x_i} \\ 0 & \cdots & 0 & \frac{\partial M_2^{i,1}}{\partial x_i} & 0 & \cdots & 0 \\ \vdots & & \vdots & \vdots & \vdots & & \vdots \\ 0 & \cdots & 0 & \frac{\partial M_2^{N_b,i}}{\partial x_i} & 0 & \cdots & 0 \end{bmatrix}, \quad (4.17)$$

$$\frac{\partial M_3}{\partial x_i} = \begin{bmatrix} 0 & \cdots & 0 & \frac{\partial M_3^{1,i}}{\partial x_i} & 0 & \cdots & 0 \\ \vdots & & \vdots & \vdots & \vdots & & \vdots \\ 0 & \cdots & 0 & \frac{\partial M_3^{i-1,i}}{\partial x_i} & 0 & \cdots & 0 \\ \frac{\partial M_3^{i,1}}{\partial x_i} & \cdots & \frac{\partial M_3^{i,i-1}}{\partial x_i} & 0 & \frac{\partial M_3^{i,i+1}}{\partial x_i} & \cdots & \frac{\partial M_3^{i,N_b}}{\partial x_i} \\ 0 & \cdots & 0 & \frac{\partial M_3^{i,1}}{\partial x_i} & 0 & \cdots & 0 \\ \vdots & & \vdots & \vdots & \vdots & & \vdots \\ 0 & \cdots & 0 & \frac{\partial M_3^{N_b,i}}{\partial x_i} & 0 & \cdots & 0 \end{bmatrix}, \tag{4.18}$$

$$\frac{\partial M_4}{\partial x_i} = \begin{bmatrix} 0 & \cdots & 0 & \frac{\partial M_4^{1,i}}{\partial x_i} & 0 & \cdots & 0 \\ \vdots & & \vdots & \vdots & \vdots & & \vdots \\ 0 & \cdots & 0 & \frac{\partial M_4^{i-1,i}}{\partial x_i} & 0 & \cdots & 0 \\ \frac{\partial M_4^{i,1}}{\partial x_i} & \cdots & \frac{\partial M_4^{i,i-1}}{\partial x_i} & 0 & \frac{\partial M_4^{i,i+1}}{\partial x_i} & \cdots & \frac{\partial M_4^{i,N_b}}{\partial x_i} \\ 0 & \cdots & 0 & \frac{\partial M_4^{i,1}}{\partial x_i} & 0 & \cdots & 0 \\ \vdots & & \vdots & \vdots & \vdots & & \vdots \\ 0 & \cdots & 0 & \frac{\partial M_4^{N_b,i}}{\partial x_i} & 0 & \cdots & 0 \end{bmatrix}, \tag{4.19}$$

Here, we have that:

- In $\frac{\partial M_1}{\partial x_i}$, the $B_i \frac{\partial T_{ji}^T}{\partial x_i}$ elements are matrices, whose size is $(2N+1)(M+1) \times (2N+1)(M+1)$, the same one of the matrices 0, composed of zeros.
- In $\frac{\partial M_2}{\partial x_i}$, the $\frac{\partial M_2^{ij}}{\partial x_i} = B_i \frac{\partial T_{ji}^T}{\partial x_i} R_j$ elements are column vectors, whose size is $(2N+1)(M+1) \times 1$, the same one of the vector 0, composed of zeros.
- In $\frac{\partial M_3}{\partial x_i}$,r the $\frac{\partial M_3^{ij}}{\partial x_i} = \frac{1}{W_j}\left[\frac{\partial T_{ij}}{\partial x_i}\tilde{B}_j^T \tilde{Y}_j^D\right]^T$ elements are row vectors, whose size is $1 \times (2N+1)(M+1)$, the same one of the vector 0, composed of zeros.
- In $\frac{\partial M_4}{\partial x_i}$, the $\frac{\partial M_4^{ij}}{\partial x_i} = \frac{1}{W_j} R_i^T \frac{\partial T_{ij}}{\partial x_i} \tilde{B}_j^T \tilde{Y}_j^D$ elements are scalars.

Now, for completeness, we list the elements of the derivatives of the coordinate transformation matrix T_{ij}.

$$\left(\frac{\partial T_{ij}}{\partial x_i}\right)^{nl}_{mm} = \begin{cases} \frac{J_l(k_0 a)}{H_n(k_0 a)}\Big[H'_{n-l}(k_0 L_{ij})\, e^{i\alpha_{ij}(n-l)} k_0 \frac{\partial L_{ij}}{\partial x_i} + & \text{if } m = 0, \\ +H_{n-l}(k_0 L_{ij})\, e^{i\alpha_{ij}(n-l)} i\,(n-l)\,\frac{\partial \alpha_{ij}}{\partial x_i}\Big] & n, l \in \mathbb{Z}, \\ \\ \frac{I_l(k_m a)}{K_n(k_m a)}\Big[K'_{n-l}(k_m L_{ij})\, e^{i\alpha_{ij}(n-l)}\,(-1)^l\, k_m \frac{\partial L_{ij}}{\partial x_i} + & \text{if } m \geq 1, \\ +K_{n-l}(k_m L_{ij})\, e^{i\alpha_{ij}(n-l)}\,(-1)^l\, i\,(n-l)\,\frac{\partial \alpha_{ij}}{\partial x_i} & n, l \in \mathbb{Z}, \end{cases} \tag{4.20}$$

where the derivatives of the Hankel function H', and the one of the modified Bessel function of the second kind K', can be computed using the following recursive relationships [1]:

$$H'_{n-l}(k_0 L_{ij}) = \frac{(n-l)\, H_{n-l}(k_0 L_{ij})}{k_0 L_{ij}} - H_{n-l+1}(k_0 L_{ij})\,, \tag{4.21}$$

$$K'_{n-l}(k_0 L_{ij}) = -\frac{1}{2}\left[K_{n-l-1}\left(k_m L_{ij}\right) + K_{n-l+1}\left(k_m L_{ij}\right)\right]. \tag{4.22}$$

Hence, the last quantities that need to be computed to complete the description of the derivative of the coordinate transformation matrix are the derivative of L_{ij} and α_{ij}, which are now described. Firstly, we write the polar expression for the difference of x and y-coordinate of body i and body j, that is

$$\begin{cases} L_{ij}\cos\left(\alpha_{ij}\right) = x_j - x_i \\ L_{ij}\sin\left(\alpha_{ij}\right) = y_j - y_i \quad . \end{cases} \tag{4.23}$$

Now, deriving with respect to x_i, we obtain

$$\begin{cases} \frac{\partial L_{ij}}{\partial x_i}\cos\left(\alpha_{ij}\right) - L_{ij}\sin\left(\alpha_{ij}\right)\frac{\partial \alpha_{ij}}{\partial x_i} = -1 \\ \frac{\partial L_{ij}}{\partial x_i}\sin\left(\alpha_{ij}\right) + L_{ij}\cos\left(\alpha_{ij}\right)\frac{\partial \alpha_{ij}}{\partial x_i} = 0 \quad . \end{cases} \tag{4.24}$$

Now, we rewrite the system in matrix-vector multiplication form $Ax = b$, where

$$A = \begin{bmatrix} \cos\left(\alpha_{ij}\right) & -L_{ij}\sin\left(\alpha_{ij}\right) \\ \sin\left(\alpha_{ij}\right) & L_{ij}\cos\left(\alpha_{ij}\right) \end{bmatrix}, \tag{4.25}$$

$$x = \begin{bmatrix} \frac{\partial L_{ij}}{\partial x_i} \\ \frac{\partial \alpha_{ij}}{\partial x_i} \end{bmatrix}, \tag{4.26}$$

$$b = \begin{bmatrix} -1 \\ 0 \end{bmatrix}. \tag{4.27}$$

At this point, to compute x, one has to invert matrix A. To check if this operation is always allowed we compute the determinant of matrix A, that is

$$det(A) = L_{ij}\cos^2(\alpha_{ij}) + L_{ij}\sin^2(\alpha_{ij}) = L_{ij}. \tag{4.28}$$

Hence, A is positive definite and can always be inverted allowing us to compute the derivative of L_{ij}, and α_{ij}, with respect to x_i, for whatever couple of bodies.

Now, we have all the equations needed to compute $\frac{\partial T_{ij}}{\partial x_i}$, but to be able to compute $\frac{\partial \mathcal{L}}{\partial x_i}$ we are still missing the derivative of T_{ij} with respect to x_j. This quantity has the same structure as (4.20), with the only difference being that $\frac{\partial L_{ij}}{\partial x_i}$ and $\frac{\partial \alpha_{ij}}{\partial x_i}$ are replaced by $\frac{\partial L_{ij}}{\partial x_j}$ and $\frac{\partial \alpha_{ij}}{\partial x_j}$ respectively. To compute these new derivatives, one simply has to derive (4.23) with respect to x_j, obtaining once again a linear system to be solved.

Now we have all the equations that need to be numerically implemented to compute $\frac{\partial \mathcal{L}}{\partial x_i}$.

The last step in the computation of the gradient of J is to compute $\frac{\partial \mathcal{L}}{\partial y_i}$. To obtain this quantity one has to follow the exact same procedure previously detailed, starting from (4.15), replacing, in each step, the derivatives with respect to x, with the derivatives with respect to y.

Once this is done, we assemble the gradient of J as

$$\nabla J = \begin{bmatrix} \frac{\partial \mathcal{L}}{\partial x_1} \\ \frac{\partial \mathcal{L}}{\partial x_2} \\ \vdots \\ \frac{\partial \mathcal{L}}{\partial x_{N_b}} \\ \frac{\partial \mathcal{L}}{\partial y_1} \\ \frac{\partial \mathcal{L}}{\partial y_2} \\ \vdots \\ \frac{\partial \mathcal{L}}{\partial y_{N_b}} \end{bmatrix}. \tag{4.29}$$

Now, we perform a test to check that the computed gradient for the optimization of the positions is correct. To be more precise, what we want to verify is that the gradient defined through the Lagrangian approach is the same one as the one obtained through the limit of the difference quotients. Starting from the definition of the gradient of the function J as the limit for $h \to 0$ of the difference quotients of J, we have that

$$\nabla J^T(x)h \to J(x+h) - J(x) \qquad for ||h|| \to 0, \tag{4.30}$$

Therefore, we check that difference quotients converge to the gradient computed through the Lagrangian approach. We do this computing how the difference between $\nabla J^T(x)h$ and $J(x+h) - J(x)$, changes for different values of

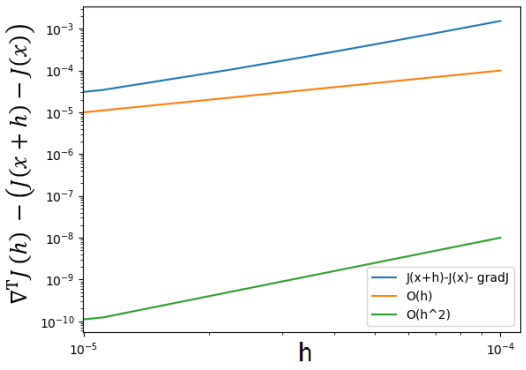

Figure 4.1: Difference between $\nabla J^T(x)h$ and $J(x+h) - J(x)$, for different values of h. Where h is a vector representing the displacement in the x-direction, of magnitude h, of the bodies in the middle line. The parameters used are shown in table 4.1. The graph has a logarithmic scale on both axes to highlight the order of convergence.

Parameter	Value	Parameter	Value	Parameter	Value
a	$1m$	$d-h$	$0.5m$	λ	$50000\frac{Ns}{m}$
δ	$4000\frac{N}{m}$	N_{bodies}	9	$spacing$	$10m$
d	$10m$	ω	$1\frac{rad}{s}$	H	$1m$
β	$0rad$	N_n	3	N_q	8
ρ	$1000\frac{kg}{m^3}$	N_h	10	h	$\left[0, \frac{1}{10000}\right] m$

Table 4.1: Parameters used for convergence analysis of the difference between $\nabla J^T(x)h$ and $J(x+h) - J(x)$.

h. The vector h is chosen to represent a displacement in the x-direction, of magnitude h, of the bodies in the middle line of a 3×3 square configuration of bodies. The results obtained from this simulation are reported in figure 4.1, and the data used are displayed in table 4.1. Looking at the graph we notice a clear convergence for $h \to 0$, as it should be. This hints toward a correct numerical implementation of the function computing the gradient.

In the graph, we also check for the order of convergence of our method. Given that the quantity we are computing is $\nabla J^T(x)h$ and $J(x+h) - J(x)$ as $h \to 0$, we can analytically compute the expected rate of convergence since $J(x+h)$ can be expanded as

$$J(x+h) \to J(x) + \nabla J^T(x)h + \frac{1}{2}h^T H_J(x)h + \mathrm{O}\big(h^3\big), \qquad for \quad h \to 0, \quad (4.31)$$

where H is the Hessian matrix of function J in computed in point x. Substituting this expression into $J(x+h) - J(x) - \nabla J^T(x)h$, we get that the only remaining terms are of second order and above, hence we expect a second order convergence rate. Therefore, the graph in figure 4.1, confirms the predicted results, showing a clear second order convergence rate, this is another strong indicator of a correct numerical implementation.

4.1.3 Projected gradient method

Here, we give an overview on how the method of the projected gradient is used to find the positions of the bodies, for which maximum power is produced.

The method requires a starting configuration. It is defined by specifying the coordinates of all bodies as the entries of a single vector v_0,

$$v_0 = \begin{bmatrix} x_1 \\ x_2 \\ \vdots \\ x_{N_b} \\ y_1 \\ y_2 \\ \vdots \\ y_{N_b} \end{bmatrix}. \quad (4.32)$$

Here, the letter v is used to avoid confusion in the algorithm, where otherwise it would seem that only the x-coordinate is modified.

Now, we have all the tools to develop our numerical implementation, whose details are reported in algorithm 1.

We notice how, in our numerical implementation, we assemble all the matrices needed to solve (2.149), apart from the coordinate transformation matrix

Algorithm 1 Positions optimization algorithm

compute all the matrices to solve (2.149), apart from T
$K = 0$
define v_0, t_0, γ, m, $maxit$, tol

while $K \leq maxit$ and $||v_K - v_{K-1}|| > tol$ **do**
  assemble T and all derivatives of T, according to (2.100) and (4.20)
  assemble M
  solve (2.149)
  compute $J(v_K)$
  solve (4.14) to compute μ and ν
  compute $\nabla J(v_K)$
  $t = t_0$
  $v^*(t) = P_{U_{2d}}(v_K - t\nabla J)$
  compute $J(v^*(t))$

  while $J(v^*(t)) - J(v_K) \leq -\frac{\gamma}{t}||v^*(t) - v_K||^2$ **do**
    $t = mt$
    compute $v^*(t)$
    assemble T and its derivatives using coordinates $v^*(t)$
    assemble M
    solve (2.149)
    compute $J(v^*(t))$
  end while

  update $v_{K+1} = v^*(t)$
  $K = K + 1$
end while

T, before entering any cycle. That is possible because T is the only quantity that will change based on the position of the bodies, and therefore needs to be updated at each iteration.

To compute v^*, we first move in the direction opposite to the one defined by the gradient, and we subsequently apply the projector operator $P_{U_{2d}}$ on this obtained configuration. This is an operator acting on the configuration, projecting it on the selected domain of feasible solutions. In case we choose to limit the domain of feasible solutions to a square with sides of length $s = spc(N_b - 1)$, where spc is the spacing between two consecutive bodies in either the x or y direction, the projector operator takes the form

$$P_{U_{2d}}(v) = \begin{bmatrix} min(max(x_1, 0), s) \\ min(max(x_2, 0), s) \\ \vdots \\ min(max(x_{N_b}, 0), s) \\ min(max(y_1, 0), s) \\ min(max(y_2, 0), s) \\ \vdots \\ min(max(y_{N_b}, 0), s) \end{bmatrix}. \tag{4.33}$$

Also, some explanations regarding the second while-loop are needed. This loop is done to perform a line search along the direction opposite to the gradient, which means looking for an appropriate step to take in the selected direction. The condition on this loop, called the Armijo rule, guarantees that a sufficient decrease in the cost function is achieved at each iteration.

4.2 Damping optimization

In this section, we show how to find the optimal damping for each individual device composing an array of wave energy converters.

The logical process is very similar to the one adopted for the optimization of the positions of the bodies. Firstly, we detail the formulation of the problem. Next, we describe how to compute the gradient of the objective function. Lastly, we detail how the above-computed gradient is used to define the optimization algorithm.

4.2.1 Formulation of the optimization problem

Here, we formulate our optimization problem. The aim of this optimization is to compute the values of the damping coefficients λ_i, associated with each of the bodies composing the array, for which the total extracted power is maximized. Once again, since it is custom to formulate a minimization problem, we define our objective function as the total extracted power with inverted sign, as in (4.2). This time, the only constraint acting on the optimization variables λ_i, is that they must be positive at each iteration. This is done to allow only for configurations where the power flow direction is correct.

4.2.2 Derivation of the gradient of the objective function

Now, to implement our optimization algorithm, we need to compute the gradient of the cost function. This, similarly to before, is done through a Lagrangian approach. Therefore, we start by formulation of the Lagrangian, which, similarly to equation (4.4), takes the form

$$\mathcal{L}(A, z; \mu, \nu; \lambda) = -\frac{1}{2}\omega^2 z^H \Lambda z + Re\big[\mu^H \left(M_1 A + M_2 z - h_1\right)\big] + \\ + Re\big[\nu^H \left(M_3 A + M_4 z - h_2\right)\big] \quad (4.34)$$

.

Now, differentiating (4.34) with respect to μ and ν, we and end up with the state equation (2.149). Meanwhile, differentiating it with respect to A and z, we obtain the adjoint equation (4.14), which we can use to compute the Lagrangian multipliers vectors μ and ν. Now, to compute the gradients of J with respect to λ, what we have left to do is compute the derivatives of the Lagrangian (4.34), with respect to each of the damping coefficients λ_i as follows.

$$\frac{\partial \mathcal{L}}{\partial \lambda_i} = -\frac{1}{2}\omega^2 z_i^H z_i + Re\left[\nu^H \left(\frac{\partial M_3}{\partial \lambda_i} A + \frac{\partial M_4}{\partial \lambda_i} z - \frac{\partial h_2}{\partial c_i}\right)\right], \quad (4.35)$$

where,

$$\frac{\partial M_3}{\partial \lambda_i} = \begin{bmatrix} 0 & \cdots & 0 & \frac{\partial M_3^{1,i}}{\partial \lambda_i} & 0 & \cdots & 0 \\ \vdots & & \vdots & \vdots & \vdots & & \vdots \\ 0 & \cdots & 0 & \frac{\partial M_3^{i-1,i}}{\partial \lambda_i} & 0 & \cdots & 0 \\ 0 & \cdots & 0 & 0 & 0 & \cdots & 0 \\ 0 & \cdots & 0 & \frac{\partial M_3^{i+1,i}}{\partial \lambda_i} & 0 & \cdots & 0 \\ \vdots & & \vdots & \vdots & \vdots & & \vdots \\ 0 & \cdots & 0 & \frac{\partial M_3^{N_b,i}}{\partial \lambda_i} & 0 & \cdots & 0 \end{bmatrix}, \tag{4.36}$$

$$\frac{\partial M_4}{\partial \lambda_i} = \begin{bmatrix} 0 & \cdots & 0 & \frac{\partial M_4^{1,i}}{\partial \lambda_i} & 0 & \cdots & 0 \\ \vdots & & \vdots & \vdots & \vdots & & \vdots \\ 0 & \cdots & 0 & \frac{\partial M_4^{i-1,i}}{\partial \lambda_i} & 0 & \cdots & 0 \\ 0 & \cdots & 0 & 0 & 0 & \cdots & 0 \\ 0 & \cdots & 0 & \frac{\partial M_3^{i+1,i}}{\partial \lambda_i} & 0 & \cdots & 0 \\ \vdots & & \vdots & \vdots & \vdots & & \vdots \\ 0 & \cdots & 0 & \frac{\partial M_4^{N_b,i}}{\partial \lambda_i} & 0 & \cdots & 0 \end{bmatrix}, \tag{4.37}$$

$$\frac{\partial h_2}{\partial \lambda_i} = \begin{bmatrix} 0 \\ \vdots \\ 0 \\ \frac{1}{W_i^2}\left[a_i^T \tilde{B}_i^T \tilde{Y}_i^D\right]\frac{\omega}{\rho g} \\ 0 \\ \vdots \\ 0 \end{bmatrix}. \tag{4.38}$$

Here, we have that:

- In $\frac{\partial M_3}{\partial \lambda_i}$, the $\frac{\partial M_3^{ij}}{\partial \lambda_i} = -\frac{1}{W_i^2}\left[T_{ji}\tilde{B}_i^T\tilde{Y}_i^D\right]^T \frac{\omega}{\rho g}$ elements are row vectors, whose size is $1 \times (2N+1)(M+1)$, same as the vectors 0, composed of zeros, present in this matrix.
- In $\frac{\partial M_4}{\partial \lambda_i}$, the $\frac{\partial M_4^{ij}}{\partial \lambda_i} = -\frac{1}{W_i^2}\left[R_j^T T_{ji}\tilde{B}_i^T\tilde{Y}_i^D\right] \frac{\omega}{\rho g}$ elements are scalars, same as the 0 elements of this matrix.
- In $\frac{\partial h_2}{\partial \lambda_i}$, the $\frac{1}{W_i^2}\left[a_i^T\tilde{B}_i^T\tilde{Y}_i^D\right] \frac{\omega}{\rho g}$ elements are scalars, same as the 0 elements of this vector.

Now, we have all the necessary items to build the gradient of J with respect to λ as

$$\nabla_\lambda J = \begin{bmatrix} \frac{\partial \mathcal{L}}{\partial \lambda_1} \\ \frac{\partial \mathcal{L}}{\partial \lambda_2} \\ \vdots \\ \frac{\partial \mathcal{L}}{\partial \lambda_{N_b-1}} \\ \frac{\partial \mathcal{L}}{\partial \lambda_{N_b}} \end{bmatrix}. \tag{4.39}$$

Here, many of the considerations made for the position optimization problem could also be applied. In particular, we focus on the fact that, following the same consideration associated with (4.31), also in this case the convergence rate of this method should be of the second order. Therefore, we check this to be true, performing a test that computes the convergence rate of the difference between $\nabla J^T(\lambda)h$ and $J(\lambda+h) - J(\lambda)$ for h approaching to zero. This is done considering as h the increase in the damping coefficients of bodies composing a 3×3 array of wave energy converter. The parameters used to run this simulation are listed in table 4.2, and the obtained results are shown in image 4.2. Looking at the graph, we see a clear second-order convergence rate, in accordance with the theoretical results. Therefore, this validates our numerical implementation of the damping coefficients optimization algorithm.

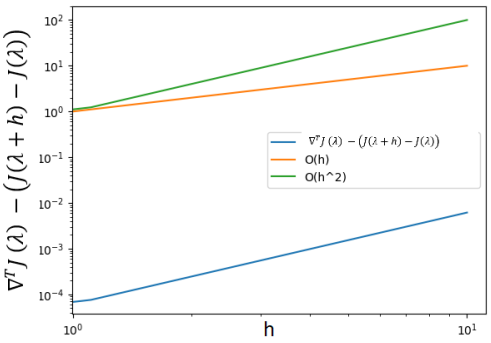

Figure 4.2: Difference between $\nabla J^T(\lambda)h$ and $J(\lambda+h) - J(\lambda)$, for different values of h. Where h is a vector representing the increase in the damping coefficient of each body of the array. The parameters used are shown in table 4.1. We use a logarithmic scale to measure the convergence rate.

Parameter	Value	Parameter	Value	Parameter	Value
a	$1m$	$d-h$	$0.5m$	λ_0	$20000\frac{Ns}{m}$
δ	$4000\frac{N}{m}$	N_{bodies}	9	$spacing$	$10m$
d	$10m$	ω	$1\frac{rad}{s}$	H	$1m$
β	$0rad$	N_n	3	N_q	8
ρ	$1000\frac{kg}{m^3}$	h	$[0,10]\,m$	N_h	10

Table 4.2: Parameters used for convergence analysis of the difference between $\nabla J^T(\lambda)h$ and $J(\lambda+h) - J(\lambda)$.

4.2.3 Gradient method

Having computed the gradient of J with respect to the vector of damping coefficients, we now use it to implement an optimization algorithm based on the gradient method. In order for this algorithm to function, it is necessary to find an initial configuration to optimize. Then we list all the damping coefficients, belonging to the above-mentioned configuration, into a single vector λ_0, an in

$$\lambda_0 = \begin{bmatrix} \lambda_1 \\ \lambda_2 \\ \vdots \\ \lambda_{N_b-1} \\ \lambda_{N_b} \end{bmatrix}. \tag{4.40}$$

The optimization algorithm is therefore implemented following a similar structure to the positions optimization algorithm, as it is shown in algorithm 2.

Notice that, differently from the case of the position optimization algorithm, here, we do not use the projected gradient method but the simpler gradient method, that is because, engineering-wise, it is simple to modify the damping coefficient of a body, meanwhile getting access to more space to install wave energy converter is more troublesome.

Another difference is the fact that, in this implementation, the only matrix that has to be computed at each iteration is W, being the only one depending on λ.

We also notice that here an additional condition is present at the beginning of the code, that is constraining λ to the set of positive values. This condition is necessary to grant that the power flow is always achievable.

4.3 Combined optimization

In this section, we analyze how to build an optimization algorithm capable of finding the optimal position and the optimal damping coefficient of each device composing the array of bodies we want to consider. Finding the optimal positions and damping coefficients at the same time has several advantages. One of the most important, is that optimizing both parameters at the same time, the problem of the positions gradient being affected by the value of the damping coefficients, and at the same time of the damping coefficients gradient being a function of the positions, is solved. This coupling problem is solved because, as we will soon see in detail, while performing this combined optimization we update both the positions of the bodies and their damping coefficients at each iteration.

The procedure through which we obtain the optimization algorithm is detailed in algorithm 3. Analyzing how this algorithm works, we start by stating that also this time a gradient method is applied. More in detail, we execute a

Algorithm 2 Damping coefficients optimization algorithm

Require: $\lambda \geq 0$
compute all the matrices to solve (2.149), except for W
$K = 0$
define λ_0, t_0, γ, m, $maxit$, tol

while $K \leq maxit$ and $||\lambda_K - \lambda_{K-1}|| > tol$ **do**
assemble W and M
solve (2.149)
compute J
solve (4.14) to compute μ and ν
compute ∇J
$t = t_0$
$\lambda^*(t) = \lambda_K - t\nabla J$
compute $J(\lambda^*(t))$

while $J(\lambda^*(t)) - J(\lambda_K) \leq -\frac{\gamma}{t}||\lambda^*(t) - \lambda_K||^2$ **do**
$t = mt$
compute $\lambda^*(t)$
assemble W and M
solve (2.149)
compute $J(\lambda^*(t))$
end while

update $\lambda_{K+1} = \lambda^*(t)$
$K = K + 1$
end while

2-steps algorithm. In the first step, the gradient of J with respect to the positions (4.29) is computed, and the positions are updated moving in the direction opposite to this gradient. In the second step, the gradient of J with respect to the damping coefficients (4.39) is computed, and again the damping coefficients are updated moving in the direction opposite to this gradient.

It has to be noted that in this algorithm we introduce the presence of two control variables, $check_1$, and $check_2$. These two are present because, in case the convergence of the positions is obtained before the convergence of the damping coefficients, the iterative process has to continue only for the damping coefficients. The same reasoning applies to the case where the damping coefficients are the ones to converge earlier than the positions. Therefore, these variables are used, as shown in algorithm 3, to allow the optimization of the parameter that has not yet reached convergence to continue. Note that it might happen that, since the value of the positions affect the value of $\nabla_\lambda J$, and since the values of the damping coefficients affect the one of $\nabla_v J$, one parameter, that at a certain iteration had converged, at another subsequent one might need to be updated, after the change of the other parameter. The use of the two control variables allows this to happen.

Another aspect to highlight is that we use two different values of tol, $t(0)$ and γ. This is the consequence of v and λ being quantities of two different orders of magnitude. For instance, being $\lambda > v$, the tol and $t(0)$ associated to λ, will be greater then the one associated to v.

This is also the reason why the two variables, v, and λ, are not jointed into a single vector with a corresponding longer gradient vector consisting in the merging of the gradient with respect to v and the one with respect to λ. If this was done, a single value for tol, $t(0)$ and γ, should have been chosen, which could not be appropriate for both v and λ. By scaling one of the two variables one could solve the problem for one of these parameters, but these would most likely still lead to the other two not being set to the correct value, given that there is not a linear law linking them.

Regardless, we don't disregard the possibility of making an implementation through a single vector of variables and a single gradient vector, given that further analysis and parameters tuning are necessary for it to be correct.

Considering the gradients used in this optimization algorithm, they are the same ones we previously developed, (4.29), (4.39). Therefore, there is no need to verify the convergence of these gradients, since we already did it in the previous sections. Also, the projecting strategy is the same as the one previously modeled, (4.33).

Now that we have developed all the tools to compute optimal positions and damping coefficients, we proceed, in the next chapter, to detail the results we obtained after numerically implementing these models.

Algorithm 3 Combined positions and damping coefficients optimization algorithm

Require: $\lambda \geq 0$
compute all the matrices to solve (2.149), apart from T and W
$K = 0$
define v_0, λ_0, $t_1(0)$, $t_2(0)$, γ_1, γ_2, m, $maxit$, tol_1, tol_2

while $K \leq maxit$ and ($||v_K - v_{K-1}|| > tol_1$ or $||\lambda_K - \lambda_{K-1}|| > tol_2$) **do**
$check_1 = 0$, $check_2 = 0$
assemble W,T, the derivatives of T, M and solve (2.149)
compute $J(v_K, \lambda_K)$
solve (4.14) to compute μ and ν
compute $\nabla_v J(v_K, \lambda_K)$
$t_1 = t_1(0)$, $v^*(t_1) = P_{U_{2d}}(v_K - t_1 \nabla_v J(v_K, \lambda_K))$
compute $J(v^*(t_1), \lambda_K)$

while $J(v^*(t_1), \lambda_K) - J(v_K, \lambda_K) \leq -\frac{\gamma_1}{t_1}||v^*(t_1) - v_K||^2$ **do**
$check_1 = 1$, $t_1 = mt_1$
compute $v^*(t_1)$
assemble T ,the derivatives of T, M and solve (2.149)
compute $J(v^*(t_1), \lambda_K)$
end while

if $check_1 = 1$ **then**
update $v_{K+1} = v^*(t_1)$
else
update $v_{K+1} = v_K$
end if
compute $\nabla_\lambda J(v^*(t_1), \lambda_K)$
$t_2 = t_2(0)$, $\lambda^*(t_2) = \lambda_K - t_2 \nabla_\lambda J(v^*(t_1), \lambda_K)$
compute $J(v^*(t_1), \lambda^*(t_2))$

while $J(v^*(t_1), \lambda^*(t_2)) - J(v^*(t_1), \lambda_K)(\lambda_K) \leq -\frac{\gamma_2}{t_2}||\lambda^*(t_2) - \lambda_K||^2$ **do**
$check_2 = 1$, $t_2 = mt_2$
compute $\lambda^*(t_2)$
assemble W, M and solve (2.149)
compute $J(v^*(t_1), \lambda^*(t_2))$
end while

if $check_2 = 1$ **then**
update $\lambda_{K+1} = \lambda^*(t_2)$
else
update $\lambda_{K+1} = \lambda_K$
if $check_1 = 0$ **then**
Break
end if
end if
$K = K + 1$
end while

Chapter 5

Optimization results

In this section, the results obtained applying the optimization strategies detailed in section 4 are shown and analyzed.

Following the same approach as in the previous sections, the data used to run the simulations of this chapter are listed in tables, so that these tests could be repeated. In addition, all the results are commented on, and the reason behind the choice of performing each of the tests is explained.

We group our results based on the optimization that is performed. A further classification is therefore applied, based on the chosen starting configurations. Firstly, in section 5.1, we list the results obtained by optimizing the positions of the bodies. Here, three different constraints will be considered concerning the positions of the bodies: a square, a rectangle, and a semi-decagon. This last configuration is chosen to mimic a natural bay area. Subsequently, in section 5.2, we perform the optimization of the damping coefficients of the bodies composing the array. We start considering the optimization of the damping coefficient of an isolated device, to later move to the optimization of the damping coefficients for a 3×3 square configuration subject to different ambient incident wave angles. Next, in section 5.3, we consider the combined optimization of the damping coefficients and of the positions of the bodies. A 3×3 square configuration is considered in this section and the tests are run for different values of the starting positions and damping coefficients. Lastly, in section 5.4, we take an overview of some of the obtained results comparing the different optimization strategies. In addition, some general considerations, concerning the optimal design of a park of wave energy converter, are drawn.

5.1 Position optimization

Here, we consider the results obtained by optimizing the positions of bodies composing arrays of wave energy converters.

We display results concerning arrays subject to different starting configurations and constraints. The most important results, that we show for each

simulation, are the final optimal positions of the bodies and the convergence of the interaction factor (2.139) to its optimal value.

In every simulation, the number of bodies will be limited to nine. This choice is made to balance the fact that a big enough number of bodies is needed to observe a significant park effect [2], with the fact that the computational costs grows quickly with the number of bodies considered, since this factor affects the size of the matrices to be assembled to solve the state equation (2.149).

We investigate configurations subject to three different kinds of constraints. The first one consists in having the bodies restricted into a square of a given area. Under this constraint, we also check how the optimal positions change with the angle of the ambient incident wave. The second configuration studied is one where the bodies are forced into a rectangle. Afterward, we study which optimal configuration is achieved by placing all the bodies inside a domain designed to mimic a natural bay. This simulation is particularly useful because it reproduces an area, the bay, that is a potential candidate for the installation of arrays of wave energy converters.

5.1.1 Square constraint

In this section, we study how the optimization of the positions of the bodies composing an array of wave energy converters, affects their distribution in space, under the constraint of them being limited inside a square of fixed area.

Remembering that the size of this specific constraint was chosen based on the considerations of section 3.4.3, we now have to choose the actual positions of the bodies inside the allowed domain. The following subsections describe one different simulation each. In the first three, the difference is in the choice of the initial configuration. Meanwhile, in the last one, we investigate what happens ranging the value of the ambient incident wave angle.

3x3 Large square

The first tested geometry consists in having the bodies displaced in the most intuitive way, that is on a 3x3 square grid that fills as much space as allowed. It is therefore clear that, at the beginning of the simulation, eight of the nine bodies are positioned on the boundary of the admissible set.

The parameter used for running this simulation are listed in table 5.1, and the obtained results are displayed in picture 5.1. Analyzing the graph showing the interaction factor as a function of the iteration number, we see that the optimization algorithm is working nicely, increasing the value of q monotonically. Sadly, we also notice that this increase in value, in absolute terms, is very marginal. This is most likely because the initial configuration was already close to a point of minimum. This conclusion, is strongly highlighted by the plot showing the difference between the initial positions and the final positions, where we see that the change in positions is almost unnoticeable. The fact that this is close to an optimal position is somewhat reasonable, given that, for the starting configuration the interaction factor was slightly less than one, therefore,

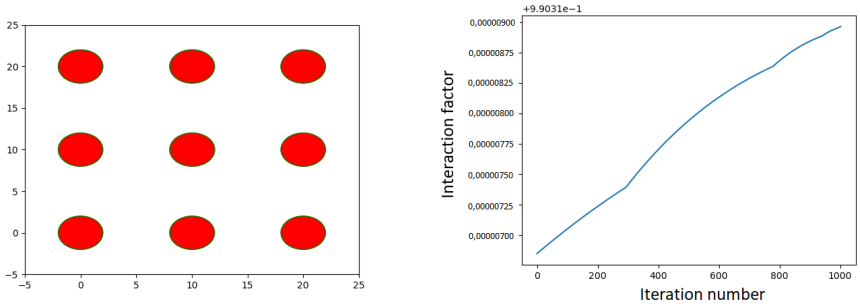

Figure 5.1: In the image on the left the initial positions are displayed (red full circle), compared to the final optimal positions (green empty circle). In the image on the right, the change in interaction factor q is shown as a function of the iteration number. The parameters used for running these simulations are listed in table 5.1.

the bodies should tend to get further from each other to get closer to the configuration where they are isolated, since it is associated to an interaction factor of one. Given that is not possible, since the selected configuration is already the one where the bodies are the furthest from each other, makes it reasonable that we started the simulation already close to an optimal configuration. We dig into this aspect in the next test, where we use, as the starting configuration, one where the bodies are very close to each other, to see if they actually tend to move apart from one another.

But before moving on, an additional consideration is made concerning the shape of the graph describing the interaction factor in figure 5.1. We notice that, in some points of the graph, there is a discontinuity in the first-order derivative of the function. This comes from the fact that, during the process of optimization, we perform a line search in the direction opposite to the one of the gradient, to determine the optimal step to take in this direction. Here, the points of discontinuity of the derivative, coincide with the iteration in which the conditions on the line search algorithm result in the selection of a bigger step.

3x3 Small square

We now test how the position optimization algorithm changes the coordinates of bodies, initially positioned into a 3×3 square array, when the distance between the bodies is such to have a starting configuration associated with a very low interaction factor. Here, the bodies are nevertheless subject to the same square constraint as in the previous configuration study, and they are initially positioned in the middle of the above-mentioned constraint. The purpose of this simulation is to first test if the expected behavior, consisting in the bodies getting further away from each other, is exhibited, and in second place, to investigate if, in the process of getting further away from each other, they tend

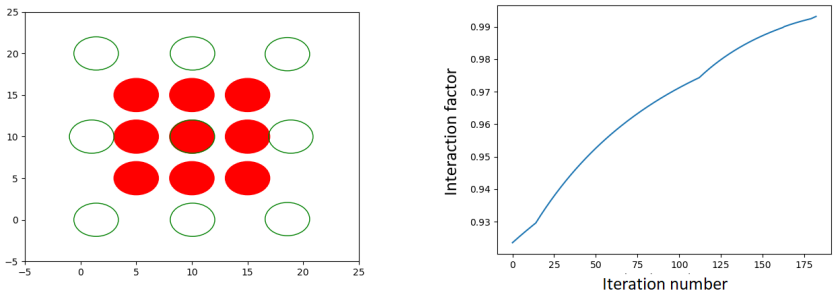

Figure 5.2: In the image on the left the initial positions are displayed (red full circle), compared to the final optimal positions (green empty circle). In the image on the right, the change in interaction factor q is shown as a function of the iteration number. The parameters used for these simulations are listed in table 5.2.

to abandon the square configuration or not.

The parameter used for running this simulation are listed in table 5.2, and the obtained results are displayed in figure 5.2. Analyzing the results displayed in the first plot of figure 5.1, we see that the bodies do indeed tend to drift away from each other as expected. We also notice that the overall structure of the configuration is maintained, however, the increase in the separation distance is non-homogeneous. In detail, we see that the increase in the y-direction is dominant, to the extent that the upper and lower constraints are active, while the constraints on the sides are not. This consideration hints towards the fact that, limiting our bodies in a rectangular constraint, we should achieve better performances for rectangles that have the longer sides along the direction perpendicular to the incoming wave. This will be later checked through an appropriate test.

Taking into account the second graph displayed in figure 5.2, we notice that there is once again a clear convergence of the interaction factor to values very close to one. The value at which the algorithm converges is very close to the starting one of the previous simulation, suggesting that, even assuming that we are only capable of finding a local minimum of the cost function, under the selected constraint, there is no significant configuration outperforming the ones we found so far.

Circle

Now, we test what happens when we run the optimization algorithm selecting, as initial condition, one where the bodies are positioned along a circle. This is done for two different reasons. The first one, is that in many studies the circular configuration is selected as a candidate for a globally optimal configuration. That is because its design implies having no dependence on the incident wave

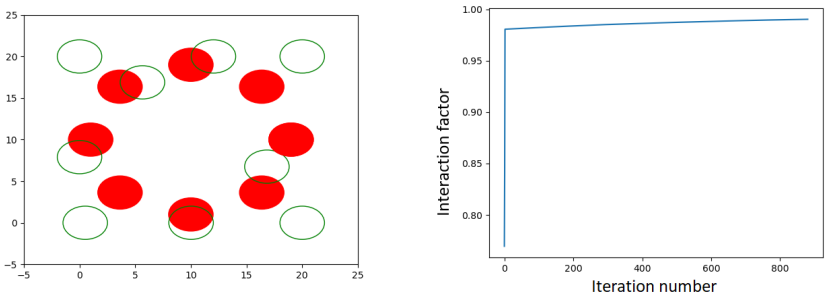

Figure 5.3: In the image on the left the initial positions are displayed (red full circle), compared to the final optimal positions (green empty circle). In the image on the right, the change in interaction factor q is shown as a function of the iteration number. The parameters used for these simulations are listed in table 5.3.

direction and a low variance power output. Given the qualities of this configuration we want to check if, once optimized, it can retain its original properties, increasing, on the other hand, the value of the produced power. The second reason is to test if, selecting this configuration the bodies tend to find a local optimum with an associated geometry resembling the original one, if the bodies will drift towards the previously found optimal geometries, or if a new optimal configuration will emerge.

The parameter used for running this simulation are listed in table 5.3, and the obtained results are displayed in picture 5.3. Looking at the first image, we see that the initial geometry is highly distorted, with most of the bodies changing their location by a significant amount. We notice that the geometry the circle configuration morphed into differs also from the rectangular one of the previous simulations. Therefore, we state that a new local minimum is found. Also, we comment on the fact that the body distribution tends to have a higher density on the left side of the domain. This is probably connected to the fact that the park effect, allows for a better interaction factor by making the bodies in the front produce more energy than if they were isolated, penalizing at the same time the bodies in the back.

Concerning the shape of the interaction factor graph, we see how the value it converges to is very close to 1. This is a shared feature with the previous simulations. An interesting aspect of this simulation is the fact that, despite the initial interaction factor being much lower than 1, the optimization algorithm makes it converge to a value very close to one of the previous simulations. This hints towards the fact that whatever configuration is chosen, under this constraint, the maximum achievable interaction factor is slightly below one.

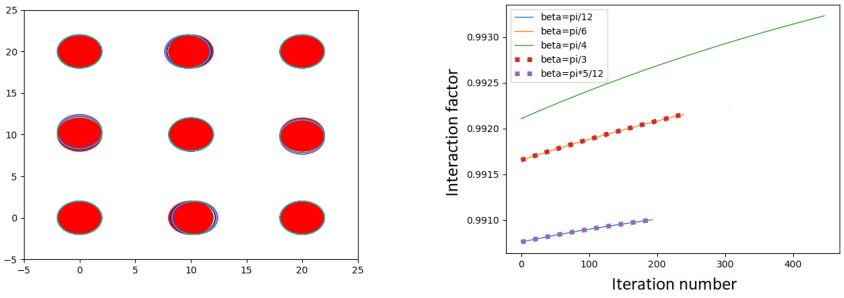

Figure 5.4: In the image on the left, the final positions of the bodies after the optimization are displayed, the circles of the same colors correspond to the same incident angle as follows: $blue(\beta = \{\frac{\pi}{12}, \frac{5}{12}\pi\})$, $cyan(\beta = \{\frac{\pi}{6}, \frac{\pi}{3}\})$, $magenta(\beta = \frac{\pi}{4})$. In the image on the right, the change in interaction factor q is shown as a function of the iteration number for each different β value. The parameters used in this simulation are listed in table 5.4.

Incident wave angle

Here, starting from the initial configuration, where the bodies are placed in a 3×3 square geometry taking up all the available space, we perform a position optimization ranging the value of the ambient wave incident angle. Performing this analysis, we want to investigate to which amount the optimal positions differ for different values of the incident angle. That is because, in most applications, the bodies are not subject to mono-directional waves, and therefore it would be pointless to point towards an optimal configuration for a given β, that provides low performances for all other values of β.

The results obtained running this simulation are displayed in figure 5.4, and the values employed for the different parameters are reported in table 5.4. From the image showing the final positions of the bodies, we see that there is no incident ambient wave angle for which the initial position is drastically modified. This is a good result, indicating that the initial arrangement is close to a local minimum for several values of the incident wave angle. We also notice that the closer the incident angle is to $\beta = \frac{\pi}{4}$, the greater the displacement of the bodies.

Looking at the image displaying the behavior of the interaction factor as a function of the iteration number, we see that some lines are overlapping. This is due to the symmetric nature of the problem. Given that the square configuration is two times symmetric, we get that an incident angle $\beta = x$ should produce the same results as with $\beta = \frac{\pi}{2} \pm x$. Our results are agreeing with the above-mentioned principle, given that the plot corresponding to $\beta = \frac{\pi}{6}$ is completely overlapping with the one associated with $\beta = \frac{5}{12}\pi$, and the one associated to $\beta = \frac{\pi}{12}$ with the one associated to $\beta = \frac{5}{12}\pi$. From this image we also notice how the interaction factor converges to higher values for the configurations associated

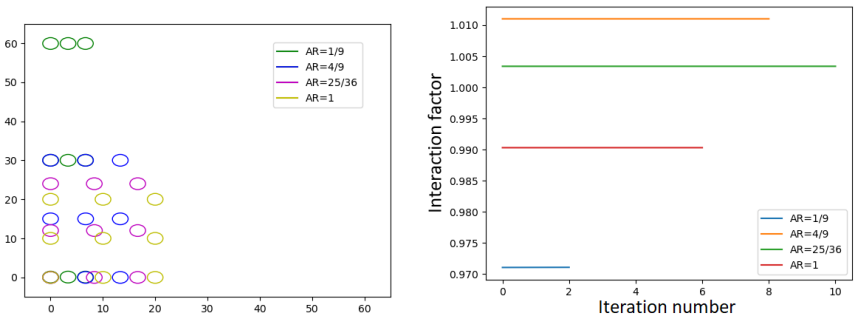

Figure 5.5: In the image on the left the final positions of the bodies after the optimization are displayed, and the circles of the same colors correspond to the same initial configuration. In the image on the right, the change in interaction factor q is shown as a function of the iteration number for each different AR value. The parameters used in this simulation are listed in table 5.5.

to lower β, this is in agreement with results obtained in the previous sections.

5.1.2 Rectangle constraint

Here, we study how, by modifying the structure of the constraining geometry to a rectangle, the optimal performances, and their associated geometries, obtained through the optimization process, are modified. The changes to the optimization algorithm, required to implement the new constraint, are quite simple and affect only (4.33). There, the value s has to be replaced by the length of the side of the rectangle in the x-direction when projecting the x-coordinates of our bodies, and by the one in the y-direction when projecting the y-coordinates of our bodies. Concerning the constraint, we choose to keep the area of the rectangle constant and equal to the one of square of the previous simulation, this is done to avoid favoring the cases where there would be more available space.

Similarly to the 3×3 square configuration, we perform our analysis both with initial configurations where the bodies are using all the available space, and with ones where the bodies are packed closer together, to see if in the rectangular case the same considerations, developed for the square case, apply.

Big rectangles vs AR

Here, we study how performances and arrangements of arrays of wave energy converters, subject to a rectangular geometrical constraint, are modified to optimize the positions of their bodies when the initial configuration of the bodies consists in a 3×3 rectangle that takes up as much space as possible. The parameter that is ranged in this simulation is the AR of the rectangle, which is defined as the ratio between the rectangle's side lying on the x-axis and the one lying on the y-axis.

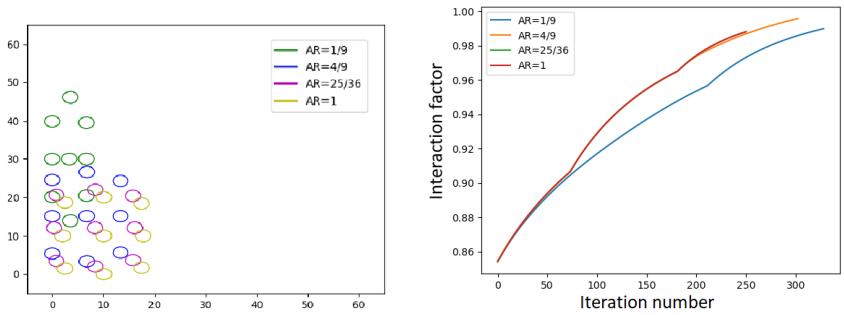

Figure 5.6: In the image on the left the final positions of the bodies after the optimization are displayed, the circles of the same colors correspond to the same initial configuration. In the image on the right, the change in interaction factor q is shown as a function of the iteration number for each different AR value. The parameters used in this simulation are listed in table 5.6.

The parameter used for running this simulation are listed in table 5.5, and the obtained results are shown in picture 5.5. Looking at the results, we can see how convergence is almost immediately reached for all the different configurations, showing that, similarly to the scenario in which the bodies are placed in a square of the maximum allowed size, the configurations in which the rectangles take up as much space as possible are locally optimal solutions. A consideration, that is not related to the optimization, but that is interesting regardless, can be made concerning the value of the interaction factor for different aspect ratios. This value can be seen to increase for values of AR that are smaller than 1. This is in agreement with the results obtained in the simulation with the small square in the square domain, which showing that the bodies to result on an active constraint, after optimization, are the top and bottom ones, suggested, as it is now confirmed, that configurations with aspect ratio lower than 1 tend to perform better.

Small rectangles vs AR

Here, similarly to the analysis with the square constraint, we impose the initial condition to be one where the bodies are packed very close to each other, in a 3×3 square configuration. Once again, we want to check whether the rectangular geometry is preserved or modified after the optimization, and if there are arrangements associated with performances greater than the one obtained before, when the staring configuration was a rectangle taking up as much space as allowed by constraints.

The results obtained from the simulations are displayed in image 5.6, and the data used to obtain the shown results are present in table 5.6. Looking at the image showing the final position of the bodies, we notice that, as expected, they tend to to drift away from each other, and that similarly to the square

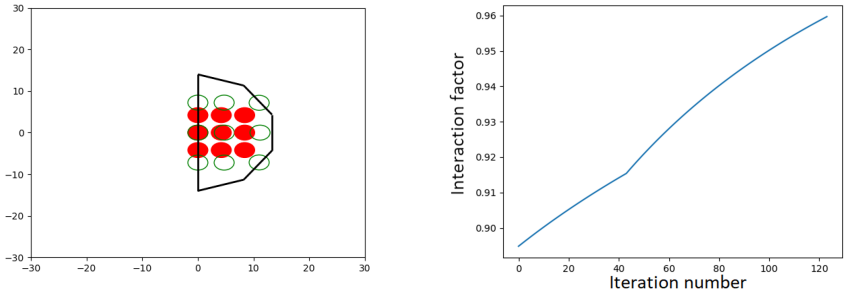

Figure 5.7: In the image on the left the final positions of the bodies after the optimization are displayed, the black line represents the boundaries of the domain, the red circle represents the initial positions, and the empty green ones, the final ones. In the image on the right, the change in interaction factor q is shown as a function of the iteration number. The parameters used in this simulation are listed in table 5.7.

scenario, they tend to preserve the initial rectangular geometry. What strikes the eye, is the fact that the bodies in the middle column are displaced by a larger amount than the ones in the first and last columns. We also notice that, for configurations with low aspect ratios, the top and bottom constraints are not active. Similarly, for configurations with a high aspect ratio, the constraints on the sides are not active.

Looking at the plot showing the convergence of the interaction factor, we highlight that clear convergence to values close to 1 is reached for all the configurations. Here, it is shown once again that some arrangements with AR lower than 1, outperform the square configuration. As a side note, we mention that the graph describing the behavior of the interaction factor for the configuration with associated AR of $\frac{25}{36}$, doesn't appear in the plot. That is because it is overwritten by the function describing the interaction factor of the configuration with $AR = 1$, which has the exact same shape.

5.1.3 Bay constraint

Here, we analyze how the positions of the bodies composing an array of wave energy converters, and its associated performances, are modified by the effect of the position optimization algorithm, having the bodies constrained into half a decagon. To implement this constraint, after having defined the vertices of the half decagon, we have to compute the equations of the line passing through each pair of consecutive vertices. Afterward, if moving in the direction opposite to the gradient (4.29) leads to a point outside the semi-decagon, the projection of the given point on the closest segment is computed, and its coordinates (x_p, y_p) become the new coordinates of the given body in the following iteration.

This test is run to simulate the condition in which the bodies are placed in

a natural bay. The importance of this simulation is therefore the fact that it mimics natural conditions better than the previous ones.

The starting positions for the bodies will be a 3×3 square, whose *spacing*, together with all the other parameters used in this simulation, is shown in table 5.7. The results obtained through the projected gradient optimization are displayed in figure 5.7.

From the first image, we see that the bodies composing the array show the usual behavior of getting further apart from each other. In addition, we see that the square structure is preserved, having bodies on active constraint only in the first and, partially, in the last column. A new feature, of this locally optimal solution, is the fact that bodies in the middle column tend to stay closer to the one of the first column rather than to the one belonging to the last one.

The interaction factor shows convergence to a value smaller than the one obtained in the previous simulations, this is because in this analysis we confine our bodies in a smaller domain.

5.2 Damping optimization

Here, we consider the results obtained by optimizing the damping coefficients of bodies composing arrays of wave energy converters.

We first analyze the results obtained considering the optimization of an isolated device. This is useful to determine the value of damping that is set as the initial condition in the following tests. Next, we look into the optimization of the damping coefficients for a 3×3 square array, where the area of the square is chosen equal to 400 m^2, similarly to the previous section. Here, tests are run for different values of the incident wave angle. This is done to test how the properties of the system change when breaking its symmetry.

5.2.1 Isolated body

Considering the optimization of the damping coefficient of an isolated body, we run two different tests. In the first one, the chosen value of the starting damping coefficient is equal to 50000 $\frac{Ns}{m}$. In the second one, it is equal to 25000 $\frac{Ns}{m}$. This is done to check if starting from different initial conditions, convergence is reached at the same value of damping, or if there are multiple optimal damping coefficients.

$\boldsymbol{\lambda_0}$=50000

We start with the isolated body configuration, characterized by the initial damping coefficient equal to 50000 $\frac{Ns}{m}$. This choice of the starting value is made because this is the value of the damping coefficients we used in all previous simulations. All the other parameters related to this simulation are displayed in table 5.8. The obtained results are shown in image 5.8.

Looking at the first graph we see that the optimal damping coefficient for an

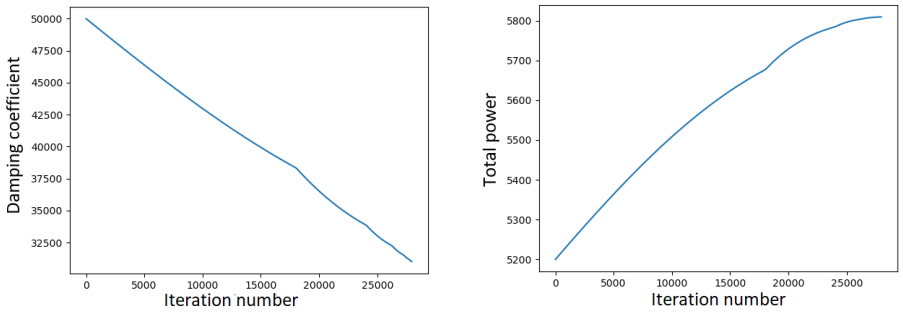

Figure 5.8: In the image on the left, the damping coefficient at each iteration of the optimization process is shown. In the image on the right, we display the power extracted by the wave energy converter at each iteration. The parameters used in this simulation are listed in table 5.8.

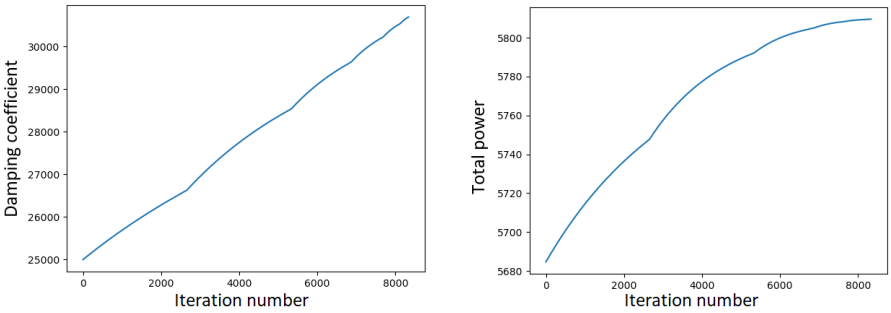

Figure 5.9: In the image on the left, the damping coefficient at each iteration of the optimization process is shown. In the image on the right, we display the power extracted by the wave energy converter at each iteration. The parameters used in this simulation are listed in table 5.8, exception made for λ_0, which is set to 25000 $\frac{Ns}{m}$.

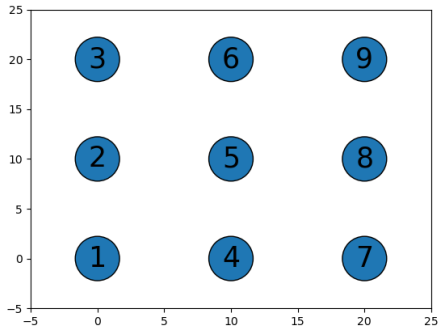

Figure 5.10: Reference for the index associated with each body.

isolated device is around the value of 31000 $\frac{Ns}{m}$. We also see that convergence is reached and, as it was the case for the positions optimization the discontinuity in the first-order derivative is a consequence of the line search process. In the second graph, the power at each iteration is shown. There, we notice clear convergence of the extracted power to a value close to $5800W$. In addition, we see that a substantial increase in performance is achieved, increasing the amount of extracted power by almost 12%. This shows the importance of the choice of a correct damping coefficient when designing a wave energy converter.

λ_0=25000

Now, we consider the optimization of the same isolated body, but using a different value for the starting damping coefficient, which is set to 25000 $\frac{Ns}{m}$. Here, the starting configuration is chosen to verify that the same value for the optimal damping is obtained, when starting the simulation with a different value of damping. More in detail we want to check that convergence is reached by approaching the solution from both sides.

The parameters used for this simulation are the same ones of table 5.8, with exception made for λ_0. The obtained results are shown in image 5.9. These results are consistent with the one of the previous simulation, showcasing convergence to the same value of extracted power, and damping coefficient.

5.2.2 3×3 square

Here, we analyze the results obtained by optimizing the damping coefficient of each individual body of a 3×3 square configuration of wave energy converters. Since the optimal damping coefficients can differ from one body to another, we use image 5.10 as a reference for the index associated with each body.

We start by simulating the case in which the ambient incident wave is perpendicular to the first line of bodies. Next, we break the symmetry of the problem, analyzing the situation in which the ambient incident wave angle has a value of $\frac{\pi}{6}$. This is done to see if some results, that are later detailed, which

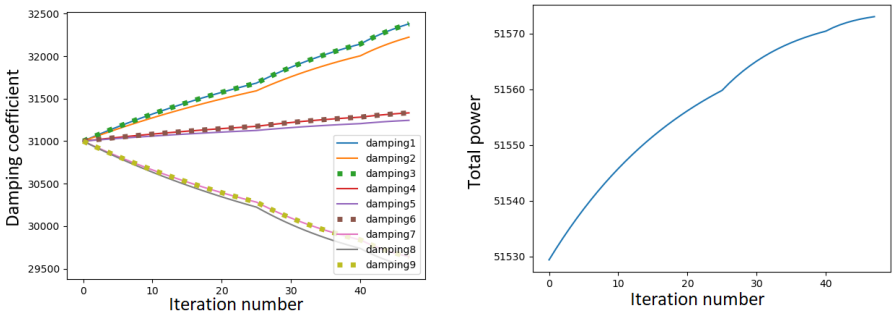

Figure 5.11: In the image on the left, the damping coefficients of each body, composing the 3×3 square array at study, are shown at each iteration of the optimization process. In the image on the right, we display the power extracted by the array at each iteration. The parameters used in this simulation are listed in table 5.9.

appear to be consequences of the symmetry of the problem, disappear when making the problem asymmetric.

We highlight that, in the simulations of this section, the starting value of the damping coefficients is set to be $\lambda_0 = 31000 \ \frac{Ns}{m}$. That is because we found this value to be the optimal damping for an isolated device, and therefore, it is our best candidate for the optimal damping also in the case of arrays composed of multiple bodies. Another consideration is made concerning the position in which the bodies are fixed. To obtain results that are comparable with the previously performed optimizations of the positions, we choose to set bodies of the 3×3 square configuration into a square of area equal to 400 m^2, which is the same one as the one we considered multiple times already in section 5.1.

β=0

Here, we show the results obtained by optimizing the damping coefficients of bodies placed in 3×3 square configuration, when they are under the influence of an ambient incident wave with a null angle. The data used for this simulation are listed in table 5.9, and the results obtained are displayed in figure 5.11.

From the second graph, we see that convergence is reached, and that the optimization of the damping coefficients leads to a significant increase in performance. This is very different from the optimization of the position, associated with the same initial configuration, that was previously carried out. This simulation hints towards the fact that the optimization of the damping coefficients, is a key element in finding the globally optimal solution to the problem of designing an array of wave energy converters.

Many considerations can also be made concerning the first graph. First of all, we can see how choosing $\lambda_0 = 31000 \ \frac{Ns}{m}$ was a good guess, given that some of the damping coefficients converged to a lower value than the starting one, and

some other to a higher one. Next, we can see how the damping coefficients of the couples of bodies $(1, 3)$,$(4, 6)$, and $(7, 9)$ are exactly identical at each iteration of the optimization process. To test if this property is a consequence of the symmetry of the system, we test, in the following simulation, if these damping coefficients keep being equal to each other when we change the value of the ambient incident wave angle. Another consideration can be made concerning the values to which the damping coefficients converge to. Looking at the values to which the damping coefficients converge, we see that the bodies located in the column that interact first with the ambient incident wave are the ones whose damping coefficient is increased the most. Meanwhile, the further away we go from the first line, the smaller the value at which the damping coefficients converge. We also notice another characteristic of this system, which is the fact that all the bodies belonging to the same column showcase a similar value of damping coefficients, with the body in the middle being always associated with the lowest value of the three. Most of these properties are probably the consequence of underlying mathematical properties of the problem at study, which we are currently unaware of, but that, if discovered, could lead to further development in the optimization of parks of energy converters.

$\boldsymbol{\beta = \frac{\pi}{6}}$

Now, we perform an optimization of the damping coefficients associated with the bodies composing a 3×3 square array of wave energy converter, when the ambient incident wave angle is equal to $\frac{\pi}{6}$. As we stated before, this test is performed to check which of the previously observed properties of the system are a consequence of its symmetry with respect to the direction of the ambient incident wave.

The parameters used for running this simulation are the same as the previous test, which are listed in table 5.9, exception made for the value of β, which is set to $\frac{\pi}{6}$. The obtained results are shown in figure 5.12.

From the second plot we can see that we have once again convergence of the extracted power, and that the value we converge to is very close to the one obtained setting $\beta = 0$.

Meanwhile, analyzing the first diagram, we see that the previously overlapping curves, now display different values of damping at each iteration, showing how the previously detailed behavior, consisting in the first and last body of each column having the same damping coefficient, was a consequence of the symmetry of the problem. Moreover, the previously clear grouping of the damping coefficients based on which was the column that they are associated with, now disappeared. At the same time, the tendency of bodies interacting earlier with the ambient incident wave to have larger damping coefficients, and similarly of bodies interacting later to have lower ones, is preserved.

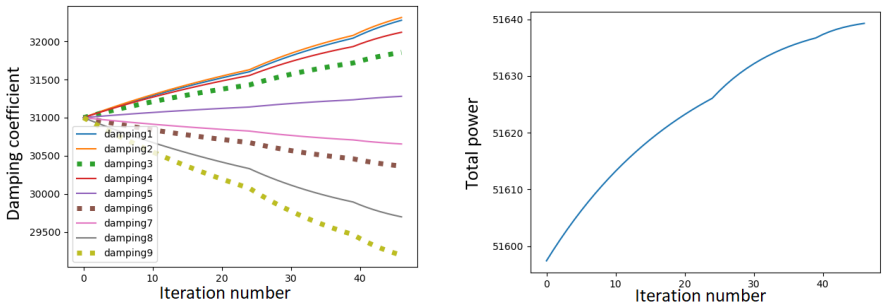

Figure 5.12: In the image on the left, the damping coefficients of each body, composing the 3×3 square array at study, are shown at each iteration of the optimization process. In the image on the right, we display the power extracted by the array at each iteration. The parameters used in this simulation are listed in table 5.9, apart from the value of β, which is set to $\frac{\pi}{6}$.

5.3 Combined optimization

In this section, we discuss the results obtained through the combined optimization of the damping coefficients and of the positions of the bodies composing an array of wave energy converters. The optimization algorithm, that we numerically implemented to obtain the results analyzed in this section, is the one described in section 4.3.

Here, three different numerical simulations are performed. All the simulations consider identical bodies placed in a 3×3 square configuration, limited inside a square domain of area equal to $400m^2$. This is done to obtain results comparable with the ones displayed in previous sections. In the first test, we define the starting positions as the ones that allows the bodies to fill up as much space as they are allowed to. This configuration resulted close to optimal, when performing an optimization affecting only the values of the positions. For the damping coefficients, we choose values close to the one for which we had optimal performances optimizing only the damping. These choices of initial conditions are made to check if the combined optimization modifies the close-to-optimal configurations found performing a single parameter optimization. In the two following tests, the initial conditions are changed, deviating from the close-to-optimal conditions of the previous simulation. This is done to allow the optimization algorithm to actually change the value of the selected parameters. In this way, we want the cross-influence, that the positions and the damping coefficients exert on each other, through the gradient of J, to allow for the formation of more interesting optimal solutions. Therefore, in the second test, the value of the initial damping coefficient is reduced to 22500 $\frac{Ns}{m}$, and the initial positions are selected to place the bodies in a more compact square centered inside the domain. Concerning the third and last simulation, the initial positions

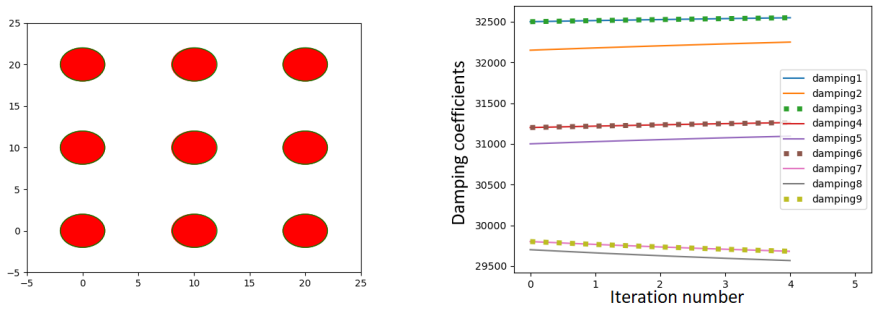

Figure 5.13: In the image on the left the initial and final positions of the bodies. In red we have the initial positions, and in green the final optimal ones. In the image on the right, the damping coefficients of each body, composing the 3×3 square array at study, are shown at each iteration of the optimization process. The parameters used in this simulation are listed in table 5.10.

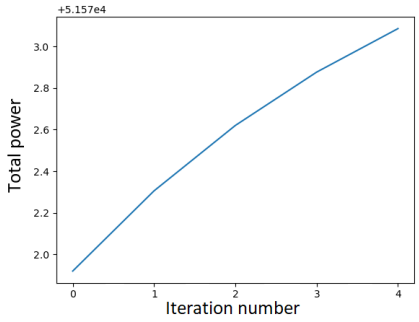

Figure 5.14: In this image we display the power extracted by the array at each iteration of the combined optimization of the positions and of the damping coefficients. The parameters used in this simulation are listed in table 5.10.

are selected to be identical to the ones in the second simulation, meanwhile, the bodies are over-damped, with damping coefficients being equal to 37500 $\frac{Ns}{m}$.

5.3.1 Big square, λ_0 optimal

Here, we show the results concerning the combined optimization of the positions and of the damping coefficients of a 3×3 square array of wave energy converters, whose positions, as previously mentioned, allow for the bodies to fill up as much space as they have available. The parameters used to run these tests are listed in table 5.10, and the results are shown in images 5.13 and 5.14.

Looking at figure 5.14, we see that the extracted power converges as it should. The increase in produced power is marginal and most likely mainly due to the optimization of the damping coefficients. Analyzing the results in figure 5.10, we see that both the positions and the damping coefficients of the bodies changed by a very small amount. This suggests that the previously obtained optimal positions solution is very weakly affected by a change in damping coefficients. In this test, we do not see how, optimizing two parameters at the time, the cross-

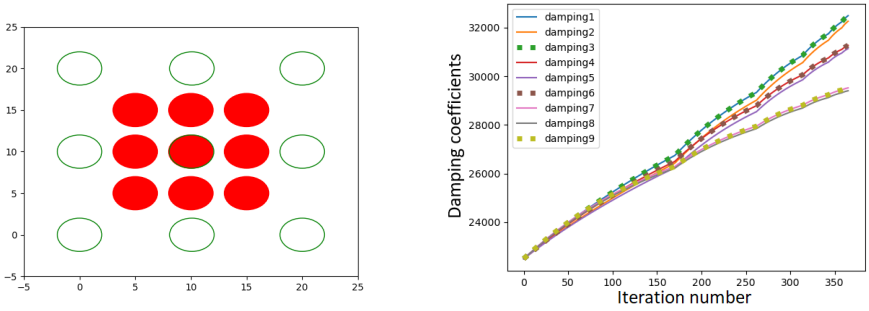

Figure 5.15: In the image on the left the initial and final positions of the bodies. In red we have the initial positions, and in green the final optimal ones. In the image on the right, the damping coefficients of each body, composing the 3×3 square array at study, are shown at each iteration of the optimization process. The parameters used in this simulation are listed in table 5.11.

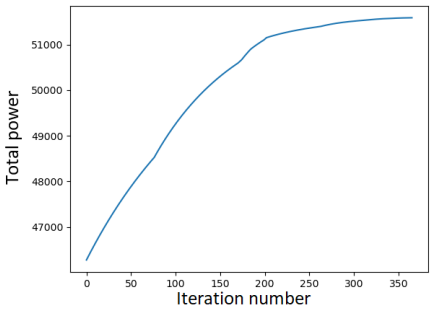

Figure 5.16: In this image we display the power extracted by the array at each iteration of the combined optimization of the positions and of the damping coefficients. The parameters used in this simulation are listed in table 5.11.

influence that they exert on each other affects the optimal solution. It almost looks like the optimization of the two parameters happens independently. To verify that this is not the case we perform the following test.

5.3.2 Small square, λ_0=22500

Here, we show the results obtained through the combined optimization of positions and damping coefficients of the bodies composing a 3×3 square array of wave energy converters. The initial positions and damping coefficients of the bodies are chosen in such a way to allow the cross-interaction between these two parameters to emerge. The detailed values of the parameters adopted in this simulation are listed in table 5.11, and the obtained results are shown in figures 5.15 and 5.16.

Looking at figure 5.16, we see the required convergence of the produced power. Starting from a sub-optimal configuration we have that the initial extracted power is significantly lower than the final optimal one. We also see that the value it converges to is very close to the one resulting from the previous

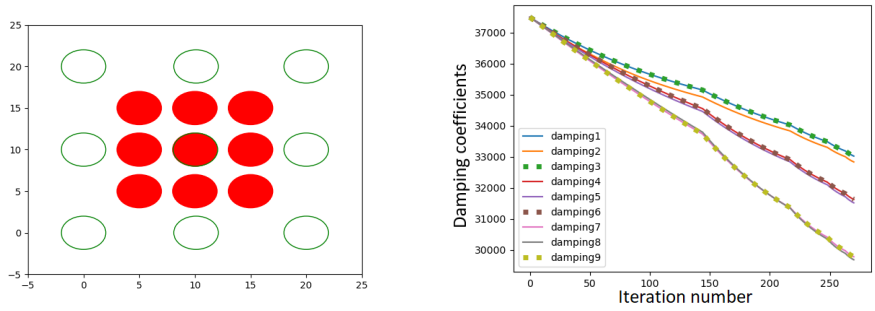

Figure 5.17: In the image on the left the initial and final positions of the bodies. In red we have the initial positions, and in green the final optimal ones. In the image on the right, the damping coefficients of each body, composing the 3×3 square array at study, are shown at each iteration of the optimization process. The parameters used in this simulation are listed in table 5.12.

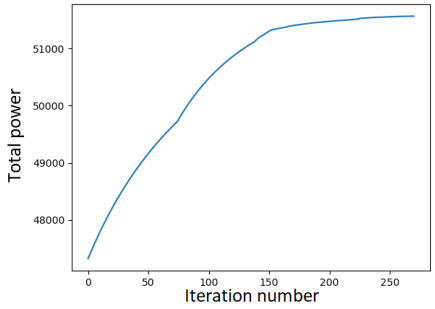

Figure 5.18: In this image we display the power extracted by the array at each iteration of the combined optimization of the positions and of the damping coefficients. The parameters used in this simulation are listed in table 5.12.

simulation, hinting at the fact that, under the given constraints, it is the maximum obtainable value of extracted power. From figure 5.15, we see the final value of the positions and of the damping coefficients of the bodies. Starting on purpose from a configuration associated with sub-optimal performances, we see that both parameters are substantially modified by the optimization algorithm. More in detail, we see that both the positions and the damping coefficients tend to value similar to the one obtained when they were optimized individually. Once again the cross-influence these two parameters exert on each other doesn't play a significant role in the optimization process. What might be related to their cross-influence, is the shape of the second graph in figure 5.15, and the number of iterations needed to reach convergence. Further testing would be necessary to prove these aspects.

5.3.3 Small square, λ_0=37500

Finally, the last configuration, consisting in a 3×3 square array with the bodies packed together at a distance of 5 m from one another, is studied. Here, the

initial damping coefficient is chosen to overdamp the system, to achieve a configuration similar to the previous test, where, having suboptimal parameters, we allowed the two optimization processes to affect each other. The parameters used in this simulation are listed in table 5.12, and the obtained results are displayed in figures 5.17 and 5.18.

Both the graphs describing the final positions and the extracted power show no significant difference from the one obtained in the previous test. Looking at the plot describing how the various damping coefficients change with the iteration number, we see that, also in this case, all the damping coefficients converge to values close to the one obtained by optimizing the damping coefficients when the positions were kept fixed. Therefore, given that all the tests performed on this configuration, no matter the initial conditions, provided the same final configuration, we conclude that in terms of damping coefficients and positions, this is the optimal solution.

5.4 Results overview

Here, a comparison between the results obtained with the different optimization algorithms is performed. The data in this section are shown both in terms of total extracted power and of the interaction factor of the configuration. Showing the total extracted power makes sense given that this is the quantity that the optimization algorithms maximize. The interaction factors are displayed to analyze by which amount the performances of the array differ from the one associated to the scenario where the bodies are isolated. An additional consideration is to be made regarding the interaction factor shown in this section. When the optimization of the damping coefficients is performed, we choose to compute the interaction factor (2.139) keeping its denominator constant in each iteration, and equal to the power extracted by a body with optimal damping multiplied by the number of bodies in the array. This is done to answer the question of whether it is possible or not to obtain more power than the sum of the powers extracted by individually optimized isolated bodies. Therefore, we do not update the value of the denominator at each iteration to avoid showing misleading information. That is because, by updating the denominator, the interaction factor would necessarily become greater than the one obtained by keeping it constant to the previously defined value. After the comparison of the results, some general considerations regarding the design of parks of wave energy converters are drawn. Since our optimizations deal only with the positions and the damping coefficients of the bodies, these final considerations will also only reflect on these two parameters.

5.4.1 Result comparison

Here, the results obtained using different optimization algorithms are compared. We only compare the results concerning the 3×3 square configuration, given that this is the one for which most tests were performed. We start by looking at

the configuration where the bodies are positioned taking up as much space as it is allowed by the selected admissible set. Subsequently, we analyze the case of the smaller square.

3x3 Big square

For this specific configuration, the optimization was run concerning the positions and the damping coefficients, both individually and in a combined optimization process. The results obtained by these optimization processes are shown in figures 5.19 and 5.20 in terms of total extracted power, and in figures 5.21 and 5.22, in terms of interaction factor. The data used for these optimizations are displayed in table 5.1, 5.9, and 5.10.

Looking at the graphs showing the total extracted power, we see how the different simulations, despite having the same starting geometry are associated with different values of initial total power. This is due to the fact that the three tests are executed using different initial damping coefficients. From a quantitative point of view, we can see how the combined optimization is the one leading to the largest final total power. This was to be expected, given that the combined optimization is the most complete optimization algorithm we developed. Analyzing the graphs displaying the interaction factors, we see that the one associated with the position optimization is actually higher than the one associated with the damping or combined optimization. This is only due to the previously mentioned choice of fixing the interaction factor denominator as the sum of the powers extracted by individually optimized isolated bodies, when evaluating optimization processes that affect damping coefficients. Comparing the interaction factor obtained through the damping optimization and the combined one, we see that, as we expected, the combined optimization is the one providing better performance. It is to be noted that, in no circumstance, the obtained interaction factor is greater than unity. This shows that, constraining the bodies in the selected domain, it is not possible to outperform isolated bodies. Nonetheless, the reduction in performances is small compared to the case of isolated bodies, and being these configuration space efficient, they are good candidates for the creation of parks of wave energy converters.

3x3 Small square

Here, we compare how the total power extracted by a 3×3 square array of wave energy converter changes at each iteration, according to the optimization process it is subject to. We perform the comparison between the results we obtained through the optimization of the position and the combined optimization. Here we do not provide a comparison with the sole optimization of the damping coefficient, since this is not a test we performed. The obtained results are displayed in figure 5.23 in terms of total power and in figure **??** in terms of interaction factor. The data used to obtain them are shown in tables 5.2 and 5.11

Once again, the total power at the first iteration is higher in the second test

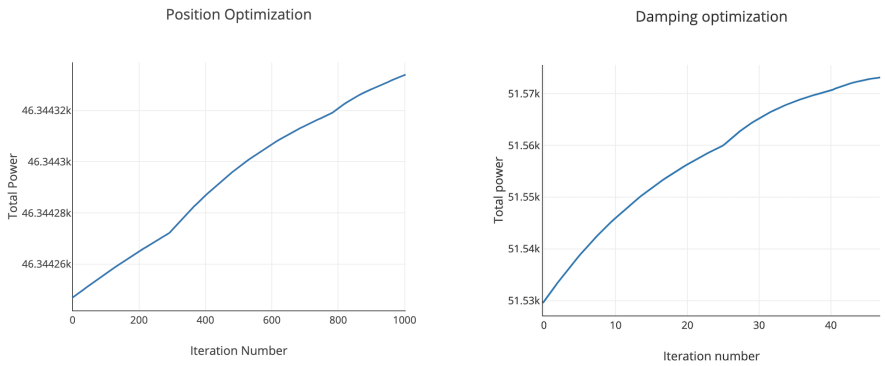

Figure 5.19: In this image we display the power extracted by the array at each iteration of an optimization process. On the left, we have the results concerning the optimization of the positions, whose data are in table 5.1. On the right, we have the results concerning the optimization of the damping coefficients, whose data are in table 5.9.

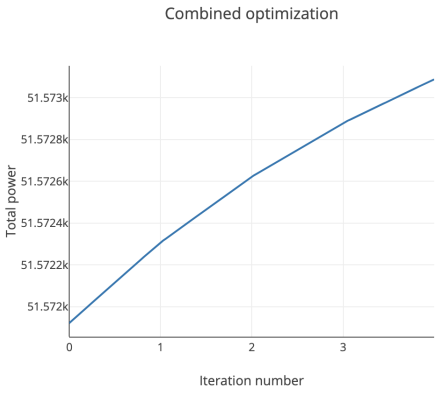

Figure 5.20: In this image we display the power extracted by the array at each iteration of the combined optimization of the positions and of the damping coefficients. The parameters used in this simulation are listed in table 5.10.

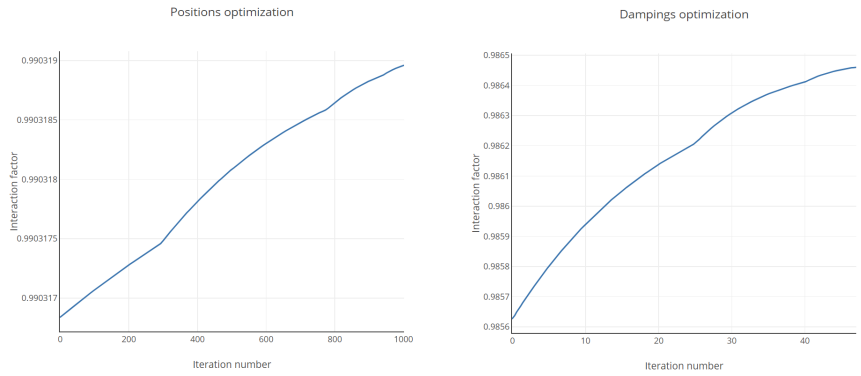

Figure 5.21: In this image we display the interaction factor associated to the array at each iteration of an optimization process. On the left, we have the results concerning the optimization of the positions, whose data are in table 5.1. On the right, we have the results concerning the optimization of the damping coefficients, whose data are in table 5.9.

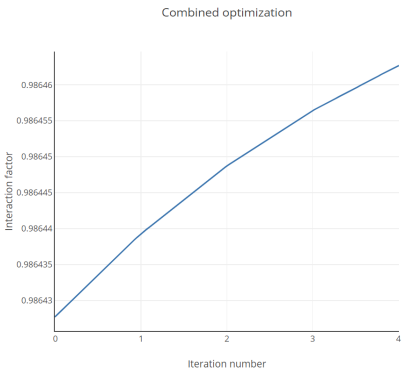

Figure 5.22: In this image we display the interaction factor associated to the array at each iteration of the combined optimization of the positions and of the damping coefficients. The parameters used in this simulation are listed in table 5.10.

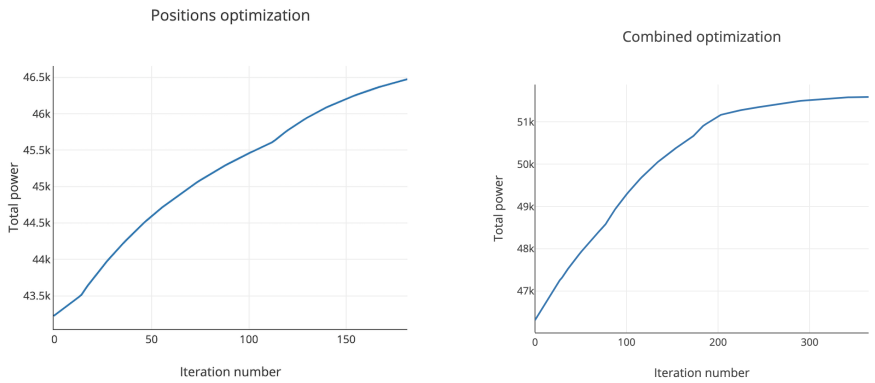

Figure 5.23: In this image, we display the power extracted by an array at each iteration of an optimization process. On the left, we have the results concerning the optimization of the positions, whose data are in table 5.2. On the right we have the results concerning the optimization of the damping coefficients, whose data are listed in table 5.11.

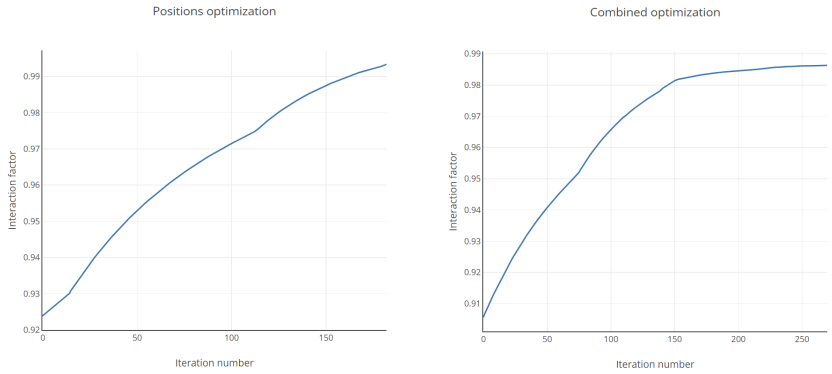

Figure 5.24: In this image, we display the interaction factor associated to the array at each iteration of an optimization process. On the left, we have the results concerning the optimization of the positions, whose data are in table 5.2. On the right we have the results concerning the optimization of the damping coefficients, whose data are listed in table 5.11.

because of the starting values of the damping coefficients. We also see that for this initial configuration the optimizations of the positions allow for a significant increase in total extracted power. That is because the initial configuration is far from an optimal solution, differently from the previous case. Nonetheless, the best-performing optimization algorithm is once again the one allowing for a combined optimization of positions and damping coefficients. Looking at the pictures showing the interaction factors at each iteration, the same considerations, derived from the case where the starting positions of the bodies allowed them to fill as much space as possible, are applicable here.

5.4.2 Design considerations

Here, we outline some useful guidelines for the process of designing a park of wave energy converters. The consideration that we are about to state are the result of the several tests and analyses performed throughout this thesis, and only concern the positions where the bodies should be located and the damping coefficients that should be associated with them.

Concerning the positions, we have that, in order to obtain an optimal configuration a trade-off between the amount of surface allowed and of power produced should be considered. Therefore, positioning our bodies in the selected area for installing the devices, to obtain maximum performance one should place them as far as possible from each other. This is done to limit the negative effect that is caused by the park effect on arrangements of bodies closely packed together.

Considering the values of the damping coefficients, we have that optimal performances are obtained by setting them to different values, according to the considered body. More in detail, we have that the bodies interacting earlier with the incident ambient wave should be associated with higher values of damping coefficients. Meanwhile, the further down the direction of the incident ambient wave we move, the lower the value of the damping coefficient we should select. The exact value to which these coefficients should be set to is difficult to estimate and therefore running an optimization algorithm is advised.

Following these simple instruction prevents ending up in situations where the park effect affects the performances of the arrays too negatively. To be able to provide a more complete list of guidelines for the design of parks of wave energy converters, more studies are necessary, where the optimization is performed with respect to more parameters.

Parameter	Value	Parameter	Value	Parameter	Value
a	$1m$	$d-h$	$0.5m$	λ	$50000\frac{Ns}{m}$
δ	$4000\frac{N}{m}$	N_{bodies}	9	$spacing$	$10m$
d	$10m$	ω	$1\frac{rad}{s}$	H	$1m$
β	$0rad$	N_n	3	N_q	8
ρ	$1000\frac{kg}{m^3}$	γ	10^{-3}	m	0.5
tol	0.00001	t_0	0.0001	$maxit$	4000

Table 5.1: Parameters used for the computation of the optimal positions for the bodies in a 3×3 square array configuration, where the bodies are constrained into a square.

Parameter	Value	Parameter	Value	Parameter	Value
a	$1m$	$d-h$	$0.5m$	λ	$50000\frac{Ns}{m}$
δ	$4000\frac{N}{m}$	N_{bodies}	9	$spacing$	$5m$
d	$10m$	ω	$1\frac{rad}{s}$	H	$1m$
β	$0rad$	N_n	3	N_q	8
ρ	$1000\frac{kg}{m^3}$	γ	10^{-2}	m	0.5
tol	0.00001	t_0	0.001	$maxit$	4000

Table 5.2: Parameters used for the computation of the optimal positions for the bodies in a 3×3 square array configuration, where the bodies are constrained into a square, which area is equal to $400m^2$.

Parameter	Value	Parameter	Value	Parameter	Value
a	$1m$	$d-h$	$0.5m$	λ	$50000\frac{Ns}{m}$
δ	$4000\frac{N}{m}$	N_{bodies}	9	R_0	$9m$
d	$10m$	ω	$1\frac{rad}{s}$	H	$1m$
β	$0rad$	N_n	3	N_q	8
ρ	$1000\frac{kg}{m^3}$	γ	10^{-2}	m	0.5
tol	0.00001	t_0	0.08	$maxit$	4000

Table 5.3: Parameters used for the computation of the optimal positions for the bodies in a circular array configuration, where the bodies are constrained into a square of side $20m$.

Parameter	Value	Parameter	Value	Parameter	Value
a	$1m$	$d-h$	$0.5m$	λ	$50000\frac{Ns}{m}$
δ	$4000\frac{N}{m}$	N_{bodies}	9	β	$[\frac{\pi}{12}, \frac{5}{12}\pi]$
d	$10m$	ω	$1\frac{rad}{s}$	H	$1m$
$spacing$	$10m$	N_n	3	N_q	8
ρ	$1000\frac{kg}{m^3}$	γ	10^{-2}	m	0.5
tol	10^{-3}	t_0	0.0004	$maxit$	4000

Table 5.4: Parameters used for the computation of the optimal positions for the bodies in a square configuration, ranging β.

Parameter	Value	Parameter	Value	Parameter	Value
a	$1m$	$d-h$	$0.5m$	λ	$50000\frac{Ns}{m}$
δ	$4000\frac{N}{m}$	N_{bodies}	9	AR	$[\frac{1}{9}, 1]$
d	$10m$	ω	$1\frac{rad}{s}$	H	$1m$
β	$0rad$	N_n	3	N_q	8
ρ	$1000\frac{kg}{m^3}$	γ	10^{-2}	m	0.5
tol	0.00001	t_0	0.01	$maxit$	4000

Table 5.5: Parameters used for the computation of the optimal positions for the bodies in a rectangular configuration, ranging AR, where the bodies are constrained into a rectangle of fixed area equal to $400m^2$.

Parameter	Value	Parameter	Value	Parameter	Value
a	$1m$	$d-h$	$0.5m$	λ	$50000\frac{Ns}{m}$
δ	$4000\frac{N}{m}$	N_{bodies}	9	AR	$[\frac{1}{9}, 1]$
d	$10m$	ω	$1\frac{rad}{s}$	H	$1m$
β	$0rad$	N_n	3	N_q	8
ρ	$1000\frac{kg}{m^3}$	γ	10^{-1}	m	0.5
tol	0.00001	t_0	0.0008	$maxit$	4000

Table 5.6: Parameters used for the computation of the optimal positions for the bodies starting in a 3×3 square configuration with initial spacing of $3.33m$, where the bodies are constrained into rectangles of variable AR, with fixed area of $400m^2$.

Parameter	Value	Parameter	Value	Parameter	Value
a	$1m$	$d-h$	$0.5m$	λ	$50000\frac{Ns}{m}$
δ	$4000\frac{N}{m}$	N_{bodies}	9	$apothem$	$\frac{21}{5}$
d	$10m$	ω	$1\frac{rad}{s}$	H	$1m$
β	$0rad$	N_n	3	N_q	8
ρ	$1000\frac{kg}{m^3}$	γ	10^{-1}	m	0.5
tol	0.00001	t_0	0.004	$maxit$	4000

Table 5.7: Parameters used for the computation of the optimal positions for the bodies starting in a 3×3 square configuration with initial spacing of $\frac{21}{5}m$, where the bodies are constrained into half of a regular decagon.

Parameter	Value	Parameter	Value	Parameter	Value
a	$1m$	$d-h$	$0.5m$	λ_0	$50000\frac{Ns}{m}$
δ	$4000\frac{N}{m}$	N_q	8	N_n	$3m$
d	$10m$	ω	$1\frac{rad}{s}$	H	$1m$
ρ	$1000\frac{kg}{m^3}$	γ	10^0	m	0.5
tol	0.00001	t_0	1024	$maxit$	4000

Table 5.8: Parameters used for the computation of the optimal damping coefficient for an isolated body.

Parameter	Value	Parameter	Value	Parameter	Value
a	$1m$	$d-h$	$0.5m$	λ_0	$31000\frac{Ns}{m}$
δ	$4000\frac{N}{m}$	N_q	8	N_n	$3m$
$Nbodies$	9	β	0	$spacing$	$10m$
d	$10m$	ω	$1\frac{rad}{s}$	H	$1m$
ρ	$1000\frac{kg}{m^3}$	γ	$10**(2)$	m	0.5
tol	0.00001	t_0	32000	$maxit$	4000

Table 5.9: Parameters used for the computation of the optimal damping coefficients of bodies displaced in a 3×3 square configuration.

Parameter	Value	Parameter	Value	Parameter	Value
a	$1m$	$d-h$	$0.5m$	λ_0	$31000\frac{Ns}{m}$
δ	$4000\frac{N}{m}$	N_q	8	N_n	$3m$
$Nbodies$	9	β	0	$spacing$	$10m$
d	$10m$	ω	$1\frac{rad}{s}$	H	$1m$
ρ	$1000\frac{kg}{m^3}$	maxit	4000	m	0.5
tol_1	0.00001	$t_1(0)$	32000	γ_1	10^2
tol_2	3	$t_2(0)$	3	γ_2	3

Table 5.10: Parameters used for the computation of the optimal damping coefficients and positions of bodies displaced in a 3×3 square configuration.

Parameter	Value	Parameter	Value	Parameter	Value
a	$1m$	$d-h$	$0.5m$	λ_0	$22500\frac{Ns}{m}$
δ	$4000\frac{N}{m}$	N_q	8	N_n	$3m$
$Nbodies$	9	β	0	$spacing$	$5m$
d	$10m$	ω	$1\frac{rad}{s}$	H	$1m$
ρ	$1000\frac{kg}{m^3}$	maxit	4000	m	0.5
tol_1	0.000001	$t_1(0)$	32000	γ_1	$10^{-0.8}$
tol_2	0.001	$t_2(0)$	0.08	γ_2	10^2

Table 5.11: Parameters used for the computation of the optimal damping coefficients and positions of bodies displaced in a 3×3 square configuration.

Parameter	Value	Parameter	Value	Parameter	Value
a	$1m$	$d-h$	$0.5m$	λ_0	$37500\frac{Ns}{m}$
δ	$4000\frac{N}{m}$	N_q	8	N_n	$3m$
$Nbodies$	9	β	0	$spacing$	$5m$
d	$10m$	ω	$1\frac{rad}{s}$	H	$1m$
ρ	$1000\frac{kg}{m^3}$	maxit	4000	m	0.5
tol_1	0.000001	$t_1(0)$	32000	γ_1	$10^{-0.8}$
tol_2	0.001	$t_2(0)$	0.08	γ_2	10^2

Table 5.12: Parameters used for the computation of the optimal damping coefficients and positions of bodies displaced in a 3×3 square configuration.

Chapter 6

Conclusions

This chapter concludes the study by summarising the research process, the key research findings in relation to the research aims and questions, and discussing the value and contribution thereof. It also reviews the limitations of the study and proposes opportunities for future research.

The main objective that we set for this thesis was to develop a model capable of determining optimal configurations of arrays of wave energy converters. To achieve this purpose, we started by analyzing the mathematical model describing the interaction between monochromatic waves and arrays of cylindrical floating bodies. This part of the analysis was crucial, since, in order to later develop the model for an array optimization algorithm, having a clear understanding of the way this interaction happens is a pivotal factor. Another reason asserting the importance of this step, is that this is the stage where the most relevant assumptions are made. Therefore, given that most of the limitations associated with our model derive from this step, this initial study is essential to be able to define in which scenarios our model will be applicable.

After having analyzed this model, and having derived the equation of motion, we realized that an optimization of the produced power was possible through a projected gradient method. Therefore we developed a mathematical model to optimize the positions of the bodies, and one to optimize the damping coefficients of the bodies. Lastly, a model for the combined optimization of the positions and of damping coefficients was obtained.

The developed models were therefore numerically implemented and verified, through a convergence analysis of the gradient. Subsequently, these models were run to obtain results concerning significant arrays layouts.

The creation of these numerical implementations is already a good result achieved by this research. Now, being the models openly available, they could be used and further improved by the scientific community. A key element that has to be improved, in case the research of this topic will progress in the direction we outlined here, is the time efficiency of the numerical implementations. We already reached some degree of efficiency by improving the numerical implementation, with respect to the first versions that we developed. Nonetheless,

better-performing computational strategies can be found.

Once the optimization algorithms were implemented, we run them with different initial configurations, and constraining our solution into differently sized domains.

We started considering the optimization of the positions of the bodies.

There, the first test we performed was one where the nine bodies, composting the array to be optimized, were constrained into a square of side equal to 20 m. We started testing them in a 3×3 square configuration that filled as much space as possible, that is because through previous tests we figured that this is a configuration with interaction factor q close to unity. What we found was that the starting configuration was already close to a local optimum, and therefore the positions of the bodies barely changed. Also, the improvement of the interaction factor was marginal.

Subsequently, to simulate a scenario in which the bodies would change their positions by a significant amount, we placed them in the same bounded domain as in the previous test, but with a different starting configuration. This time, they were still in a 3×3 square array, but packed closer together. Clearly, this initial configuration was associated to a much lower interaction factor, and the bodies tended to drift away from each other as expected. Here, a first interesting result was found, that is that the bodies did not simply get as far from each other as possible, trying to get closer to the configuration where the interaction is equal to one by definition. They instead drifted away from each other non-homogeneously, favoring displacements in the direction perpendicular to the incoming ambient wave. From here, we had an idea for the development of a subsequent test that is later described. Continuing with the same square constraint, we performed another two tests. The first one consisted in testing the circular geometry, this is done because the circular geometry has many benefits, such as being associated with low variance power output, and having no dependence on incident ambient wave direction. What we hoped to achieve here, was to discover a configuration that preserved the positive aspects of the circular configuration, while at the same time going beyond the limitation of the low total produced power. The results didn't match our expectations, given that the performances were indeed optimized, to a level similar to the one associated with the previously studied configurations, but the newly obtained arrangement was a complete distortion of the original circular geometry, and therefore did not carry all the benefits associated to the latter. The last test, performed under the square constraint, is one where the bodies were placed in the same way as in the first test, but the incident wave angle was ranged instead of being kept constant. The obtained results, highlighted the symmetric nature of this configuration and showed that the closer the angle was to $\frac{\pi}{4}$, the lowest the value at which the interaction factor converged. At the same time, the greatest overall displacement that the bodies were subject to, was found in correspondence of angles close to $\frac{\pi}{4}$. The most important result obtained from this test is, despite the bodies being displaced of different amounts based on the value of the incident wave, the fact that this displacement was always very small, hinting towards the fact that the square configuration, in which the bodies takes up as much

space as possible, is close to an optimal solution independently of the value of the incident wave angle.

Moving on from the square constraint, we adopted a rectangular constraint. Here, the total area of the rectangles was kept equal to the one of the squares in the previous tests. That is to avoid finding favorable solutions only due to the fact that more space was allowed in this scenario. We performed two tests. Both of them were run for different values of the aspect ratio of the rectangle. In the first one, the bodies were positioned in such a way as to cover as much space as possible. Starting from these initial conditions, the positions of the bodies got modified only slightly, and we got a confirmation that some rectangles having the side perpendicular to the ambient incident wave longer than the other, led to greater performances, compared to the square configuration. The second test, consisted in running the simulation but under different initial positions. We chose to pack the bodies in smaller rectangles positioned at the center of the allowed domain. This was done for the same reason related to the analogous test with the square configuration. We found that, in this case, the bodies in the middle column tended to move, in the vertical direction, more than the ones in the first and last column. The obtained performances were not substantially different from the previous test.

Lastly, we considered the body constrained into a semi-decagon. This was done to simulate the more engineering-wise interesting scenario, where the bodies are located in a natural bay. This configuration is of great interest, because it simulates a possibly real application of wave energy converters. The results showed lower performances than in the previous simulations, but this was to be expected given that the area we constrained the bodies inside was smaller. We found some bodies to be on the active constraint, and moreover, the middle column to stay closer to the first one rather than to the last one.

After having optimized the positions, we moved on with simulating the optimization of the damping coefficients. We started optimizing the damping coefficient of a single device, starting from an initial configuration associated with a damping coefficient of 50000 $\frac{Ns}{m}$, since this is the value we used in the previous tests. We obtained clear convergence of the damping coefficients to a value close to 31000 $\frac{Ns}{m}$, and a significant improvement in the extracted power. Subsequently, we repeated the same test with an underdamped system, and the damping coefficient converged again to the same value. Moving on, we optimized the damping coefficients of a 3×3 square array of wave energy converters. Once again, the area of the square was set to be 400 m^2. Here, the initial damping coefficient was set to be equal to 31000 $\frac{Ns}{m}$, being the value associated with optimal performances of an isolated body. We obtained that the produced power increased significantly, and that all the studied quantities reached convergence. Some of the damping coefficients increased in value with respect to the initial one, and some others got reduced. A trend was found, consisting in the bodies interacting first with the incident wave having the greatest increase in interaction factor. We also notices how the symmetry of the system played a significant role in the results, having the top and bottom body of each column the same value of damping coefficient at each iteration. The following test consisted in

breaking the symmetry of the system, changing the value of the incident ambient wave angle. There, we observed that all the bodies damping coefficients converged to different values.

As the last set of tests, we covered the combined optimization of the bodies' positions and damping coefficients. We always constrained our body into a square of area equal to (400 m^2). In the first test, we started from a 3×3 square array configuration, with the bodies taking as much space as possible (400 m^2), combined with values close to the optimal ones we previously computed for the damping coefficients. The results showed a little improvement in performance, and a very marginal change in positions and dampings. Therefore, in the following test, to check if the cross-influence that the positions and the damping coefficients exert on each other would lead us to different final configurations, we considered an overdamped system, with the bodies packed close together in a small square placed at the center of the domain. The results led to a configuration similar, both in terms of positions and damping coefficients, to the one of the previous tests. Also repeating the test with an underdamped system, we obtained the same results.

Therefore, we were able to show that our numerical implementation is indeed able to optimize positions and damping coefficients of an array composed of multiple bodies. And, given that no matter the initial condition we always obtained the same final configuration, we obtained what is most likely, in terms of positions and damping coefficients of the bodies, the optimal configuration of our problem.

Through our analysis, we obtained many interesting results, but what matters the most is that we set the foundation for future studies on this topic. Specifically, further progress could be done modeling the optimization algorithms of other quantities of the body, such as the stiffness coefficients and its geometrical properties. Only once the cost function will be optimized with respect to all the quantities it depends on, one will be able to state that he found the truly optimal solution to this problem. The formulation of this problem could be made even more complicated, considering the combined optimization of power produced and of the variance of the extracted power. To make an even more complete analysis, also nonlinear effects should be taken into account, as well as other factors such as the length of the cables connecting the bodies to the electrical grid.

Given the current state of things, our research allowed for a small step in the direction of making wave energy converters a competitive power source.

Bibliography

[1] Arfken, G. B., and Weber, H. J. *Mathematical Methods for Physicists (sixth edition)*. Academic Press, 2005.

[2] Babarit, A. On the park effect in arrays of oscillating wave energy converters. *Renewable Energy, Elsevier 58* (2019), 68–78.

[3] Bailey, H., Robertson, B., Ortiz, J., and Buckham, B. Stochastic methods to predict wec array power for grid integration. In *Proceedings of the 11th European Wave and Tidal Energy Conference (EWTEC)* (Nantes, 2015).

[4] Borgarino, B., Babarit, A., and Ferrant, P. Impact of wave interactions effects on energy absorption in large arrays of wave energy converters. *Ocean Engineering 41* (2012), 79–88.

[5] Budal, K. Theory for absorption of wave power by a system of interacting bodies. *Journal of Ship Research 21*, 04 (1977), 248–254.

[6] Child, B. F. M. *On the configuration of arrays of floating wave energy converters*. PhD thesis, The University of Edinburgh, 2011.

[7] Child, B. F. M., and Venugopal, V. Optimal configurations of wave energy device arrays. *Ocean Engineering 17* (2010), 1402–1417.

[8] Devolder, B., Stratigaki, V., Troch, P., and Rauwoens, P. Towards the numerical simulation of 5 floating point absorber wave energy converters installed in a line array using openfoam. In *Proceedings of the 12th European Wave and Tidal Energy Conference (EWTEC)* (Cork, 2017).

[9] Engström, J., Eriksson, M., Göteman, M., Isberg, J., and Leijon, M. Performance of large arrays of point absorbing direct-driven wave energy converters. *Journal of Applied Physics 114*, 20 (2013), 204–502.

[10] Evans, D. V. Some analytic results for two- and three-dimensional wave energy absorbers in power from sea waves. *Journal of Fluid Mechanics 112* (1980), 213–248.

[11] Faraggiana, E., Masters, I., and Chapman, J. Design of an optimization scheme for the wavesub array. In *Proceedings to RENEW conference* (Lisbon, 2018).

[12] Fitzgerald, C. J., and Thomas, G. A preliminary study on the optimal formation of an array of wave power devices. In *Proceedings of the 7th European Wave and Tidal Energy Conference (EWTEC)* (Porto, 2007).

[13] Gao, Z., and Moan, T. Mooring system analysis of multiple wave energy converters in a farm configuration. In *Proceedings of the 8th European Wave and Tidal Energy Conference (EWTEC)* (Uppsala, 2009).

[14] Giassi, M., Göteman, M., Thomas, S., Engström, J., Eriksson, M., and Isberg, J. Multi-parameter optimization of hybrid arrays of point absorber wave energy converters. In *Proceedings of the 12th European Wave and Tidal Energy Conference (EWTEC)* (Cork, 2017).

[15] Goda, Y. *Random Seas and Design of Maritime Structures (Third Edition)*, vol. 15 of *Advanced Series on Ocean Engineering*. World Scientific, 2010.

[16] Goteman, M., Engstrom, J., Eriksson, M., Isberg, J., and Leijon, M. Methods of reducing power fluctuations in wave energy parks. *Journal of Renewable and Sustainable Energy 06*, 04 (2014), 043–103.

[17] Kagemoto, H., and Yue, D. Interactions among multiple three-dimensional bodies in water waves: an exact algebraic method. *Journal of Fluid Mechanics 166* (1986), 189–209.

[18] Konispoliatis, D., and Mavrakos, S. Hydrodynamics and power absorption characteristics of free floating and moored arrays of owc's devices. In *Proceedings of the 33rd Offshore and Arctic Engineering Conference (OMAE2014)* (San Francisco, 2014).

[19] Letcher, T. M. *Future Energy (Second Edition) Improved, Sustainable and Clean Options for our Planet*. Elsevier Science, 2014.

[20] Mavrakos, S. Hydrodynamic coefficients for groups of interacting vertical axisymmetric bodies. *Ocean Engineering 18*, 5 (1991), 485–515.

[21] Mavrakos, S., and Koumoutsakos, P. Hydrodynamic interaction among vertical axisymmetric bodies restrained in waves. *Applied Ocean Research 9*, 3 (1987), 128–140.

[22] McGuinness, J., and Thomas, G. Optimal arrangements of elementary arrays of wave-power devices. In *Proceedings of the11th European Wave and Tidal Energy Conference* (Nantes, 2015).

[23] McGuinness, J. P. L., and Thomas, G. Optimisation of wave-power arrays without prescribed geometry over incident wave angle. *International Marine Energy Journal 4*, 1 (2019), 1–10.

[24] Ohkusu, M. Hydrodynamic forces on multiple cylinders in waves. In *Proceedings of the International Symposium on The Dynamics of Marine Vehicles and Structures in Waves* (London, 1974).

[25] Rumpf, R., Fiddy, M., and Testorf, M. Design of generalized invisible scatterers. *Optics Express 15*, 8 (2007), 4735–4744.

[26] Simon, J. Multiple scattering in arrays of axisymmetric wave-energy devices. part 1: a matrix method using a plane-wave approximation. *Journal of Fluid Mechanics 120* (1982), 1–25.

[27] Sinha, A., Karmakar, D., and Soares, C. Performance of optimally tuned arrays of heaving point absorbers. *Renewable Energy 92* (2016), 517–531.

[28] Snyder, L., and Moarefdoost, M. Optimizing wave farm layouts under uncertainty. In *Proceedings of the 3rd Marine Energy Technology Symposium (METS2015)* (Washington, 2015).

[29] Tissandier, J., Babarit, A., and Clément, A. H. Study of the smoothing effect on the power production in an array of searev wave energy converters. In *Proceefing of the 18th Conference of the International Society for Offshore and Polar Engineering* (Vancouver, 2008).

[30] Vicente, P., de O Falcão, A., Gato, L., and Justino, P. Dynamics of arrays of floating point-absorber wave energy converters with inter-body and bottom slack-mooring connections. *Applied Ocean Research 09*, 04 (2009), 267–281.

[31] Vicente, P., de O Falcão, A., and Justino, P. A time domain analysis of arrays of floating point-absorber wave energy converters including the effect of nonlinear mooring forces. In *Proceeding of the 3rd International Conference on Ocean Energy* (Bilbao, 2010).

[32] Wang, L., Göteman, M., Engström, J., Eriksson, M., and Isberg, J. Constrained optimal control of single and arrays of point-absorbing wave energy converters. In *Proceedings of the 3rd Marine Energy Technology Symposium (METS2015)* (Washington, 2015).

[33] Weber, H. J., Harris, F., and Arfken, G. B. *Essential Mathematical Methods for Physicists*. Elsevier, 2004.

[34] Wolgamot, H. A., Taylor, P. H., and Taylor, R. E. The interaction factor and directionality in wave energy arrays. *Ocean Engineering 47* (2012), 65–73.

[35] Yang, S. H., Ringberg, J., and Johnson, E. Analysis of interaction effects between wecs in four types of wave farm. In *Proceedings of The 3rd International Conference on Renewable Energies Offshore (RENEW 2018)* (Lisbon, 2019).